Detection and functional analysis of Ca^{2+} microdomains and BK channels in olfactory receptor neurons of larval *Xenopus laevis*

Dissertation

for the award of the degree

"Doctor of Philosophy (PhD)/Dr. rer. nat."

Division of Mathematics and Natural Sciences

of the Georg-August-University Göttingen

submitted by

Guobin Bao

From: Shanghai, P.R. China

Göttingen, Aug. 31th, 2010

Member of the Thesis Committee (Reviewer): Prof. Dr. Dr. Detlev Schild

Dept. of Neurophysiology and Cellular Biophysics, University of Göttingen

Member of the Thesis Committee (Reviewer): Prof. Dr. Michael Müller

Dept. of Neurophysiology and Sensory Physiology, University of Göttingen

Member of the Thesis Committee: Prof. Dr. Fred Wolf

Dept. of Non-linear Dynamics, Max Planck Institute for Dynamics and Self-Organization

Member of the Thesis Committee: Dr. André Zeug

Dept. of Cellular Neurophysiology, Center of Physiology, Hannover Medical School

Date of submission of the PhD Thesis: Aug. 31th, 2010

Day of Thesis Defense (Disputation):

Herewith I declare, that I prepared the thesis "Detection and functional analysis of Ca^{2+} microdomains and BK channels in olfactory receptor neurons of larval *Xenopus laevis*" on my own and with no other sources and aids than quoted.

Guobin Bao

Göttingen, Aug 30th, 2010

Contents

List of Figures

List of Tables

List of Abbreviations

$[Ca^{2+}]$	calcium concentration
$\Delta[Ca^{2+}]$	change of Ca^{2+} concentration
AP	action potential
ATP	adenosine 5′-triphosphate
BAPTA	1,2-bis(2-aminophenoxy)ethane-N,N, N',N'-tetraacetate
cAMP	cyclic adenosine monophosphate
ChTx	Charybdotoxin
cLSM	confocal laser-scanning microscopy
CRU	Ca^{2+} release unit
CV	coefficient of variation
DMSO	dimethyl sulfoxide
EGTA	ethylene glycol-bis-(2-aminoethyl)-N,N,N',N'-tetraacetic acid
ER/SR	endoplasmic/sarcoplasmic reticulum
GTP	guanosine 5′-triphosphate
IbTx	Iberiotoxin
IP_3R	Inositol trisphosphate
NCKX	Na^+/Ca^{2+}-K^+ exchangers
NCX	Na^+/Ca^{2+} exchangers
ORN	olfactory receptor neuron
RCK	regulator of conductance for K^+
RyR	Ryanodine receptor
SAC	stretch-activated channel
TEA	tetraethylammonium
TM	transmembrane
TTX	Tetrodotoxin
VGCC	voltage-gated Ca^{2+} channel

Abstract

Olfactory receptor neurons (ORNs) sense odors through the interaction of odorants with their receptors, accomplishing the first step of olfactory signaling via the generation of action potentials (APs). It is well known that BK channels and voltage-gated Ca^{2+} channels (VGCCs) are involved in the fine tuning of APs in many neurons, however, due to the low expression levels of both channels in ORNs, it is still unknown whether they remain functioning. In the current study, a co-localization of BK channels and voltage-dependent Ca^{2+} microdomains is observed on the surface of ORNs of *Xenopus laevis*, and the functional Ca^{2+} microdomains may comprise mainly the VGCC clusters rather than single Ca^{2+} channels. Moreover, the distance between BK channels and VGCCs is also estimated by using various Ca^{2+} buffers, and the estimate is around 50 to 200 nm but no less than 30 nm. Besides, blocking BK channels with Iberiotoxin (IbTx) or chelating Ca^{2+} ions by BAPTA results in a significant increase in the decay time of AP falling phases, and IbTx also decreases the firing rates of ORNs in response to odorant stimuli. Taken together, the current findings demonstrate that despite the low expression level, by forming functional Ca^{2+} microdomains, BK channels and VGCCs achieve a key function in olfactory signaling, shaping the APs and facilitating the firing rates.

1. Introduction

1.1 BK channels

A BK channel is a Ca^{2+}-activated K^+ channel. Based on its two properties, conducting potassium ions and depending on intracellular calcium ions, it is usually called "potassium large conductance calcium-activated channel" (an official full name also for its gene: KCNMA1) or "large-conductance calcium-activated potassium channel". A BK channel also has many other names like high-conductance maxi-K channel (or Maxi-K) (Latorre and Miller, 1983), Slowpoke (dSlo or Slo1), $K_{Ca}1.1$, KVCA or KCNMA, which come from the gene names of channel α-subunits, and Ca^{2+}-dependent big-conductance K^+ channel (Blatz and Magleby, 1987) which is the source of B (big-conductance) and K (potassium). Sometimes, it is even simply written as BK.

1.1.1 Three Ca^{2+}-activated K^+ channels

The BK channel belongs to a subclass of the Ca^{2+}-activated K^+ channel family. Based on the differences in single-channel conductance, pharmacological properties, and voltage dependence of channel opening, this family owns three subclasses. Two others are the "small conductance calcium-activated potassium channel" (SK channel, 10-20 pS) and the "intermediate conductance calcium-activated potassium channel" (IK channel, 25-100 pS). The SK channel is typically blocked by the bee venom Apamin, and its open probability is unaffected by membrane potential (Bond *et al.*, 1999). The IK channel is selectively blocked by 1-[(2-chlorophenyl) diphenylmethyl]-1H-pyrazole (TRAM-34) or NS1619 (a BK channel opener); and its gating is also not voltage-dependent (Wulff *et al.*, 2000; Vergara *et al.*,1998). These are the main differences of SK or IK channels from BK channels when originally researchers discovered them. The BK channel is found to be blocked by tetraethylammonium (TEA), paxilline, Iberiotoxin (IbTx), and Charybdotoxin (ChTx). Normally, its opening is both voltage- and Ca^{2+}-dependent, meaning that it will not open when intracellular Ca^{2+} concentration ($[Ca^{2+}]_i$) is low, yet when $[Ca^{2+}]_i$ reaches the threshold its gating is voltage-dependent (Xia *et al.*, 2002).

1.1.2 K$^+$ selectivity and Ca^{2+}-activated specificity

Although ion channels with a large conductance were not supposed to be so selective, the BK channel has an extremely big conductance (~250 pS) while it is very selective to conduct K$^+$. Reports show that it conducts K$^+$ 10-fold more effectively than Rb$^+$, and 150 to 200-fold more effectively than Cs$^+$ and Li$^+$, respectively (Eisenman *et al.*, 1986; Stefani *et al.*, 1997). However, it is essentially impermeant to Na$^+$, for which the permeability ratio to K$^+$ was less than 0.03 (Blatz and Magleby, 1984); and the permeabilities of other monovalent ions like NH$_4^+$ and TEA$^+$ are also similarly low (Kehl and Wong, 1996). Binding of TEA$^+$ even disrupts BK channels. So, TEA applied extracellularly in low concentrations (5–10 mM) was able to block BK channels effectively (Hicks and Marrion, 1998).

On the other hand, the activation of BK channels by intracellular Ca^{2+} is not so specific that it can be influenced by many other divalent ions. Sr^{2+} has been reported to have a binding site at the C-terminal tail of the channel, which is independent of main Ca^{2+} binding sites and can potentiate the channel activity independently (Zeng *et al.*, 2005). Mg^{2+} has also been reported to enhance the BK channel activation (Golowash *et al.*, 1986) and increase the Hill coefficient of the channel when it is activated by Ca^{2+}, which indicates that Mg^{2+} may share part of the Ca^{2+} binding sites at a BK channel and also introduce extra binding sites. Furthermore, many other divalent cations have been shown to modulate the BK channel coordinatively, enhancing the channel activation by Ca^{2+} and increasing the Hill coefficient as well (Oberhauser *et al.*, 1988). Such divalent cations are Mn^{2+}(25), Fe^{2+}(26), Co^{2+}(27), Ni^{2+}(28) and Cd^{2+}(48) (brackets are atomic number).

1.1.3 BK channel structures

BK channels have a high selectivity for conducting K$^+$ but have a low specificity for being activated by divalent ions, which is inseparably characterized by the complex channel-protein structures themselves (Figure 1A). BK channels structurally belong to the S4 superfamily of K$^+$ channels, which, discovered so far, possesses a core of

α-subunits comprising either one or two copies of a highly conserved pore loop domain (P-domain). The P-domain motifs share the sequence, T/SxxTxGxG, which has been termed as the K^+-selectivity signature sequence (Moulton *et al.*, 2003). In families that contain one P-domain, for example the BK channel family, a selective pathway for K^+ across the membrane is assembled by four α-subunits (Figure 1B). However, it remains unknown how two P-domain subunits assemble to form a selective pore; what is known is that usually two P-domain channels are highly regulated K^+ selective leak channels (Goldstein *et al.*, 2001). In this S4 superfamily, except for inward-rectifying K^+ channels which have two transmembrane (TM) domains, all the other channels including all voltage-gated K^+ channels (Kv), KCNQ channels (originally known as KvLQT channels), EAG-like K^+ channels, and three Ca^{2+}-activated K^+ channels (BK, IK and SK), are characterized by having six TM domains (named S1-S6) including one positively charged S4 domain, toward which all the experimental evidence points as the domain in charge of sensing the voltage (reviewed by Swartz, 2008).
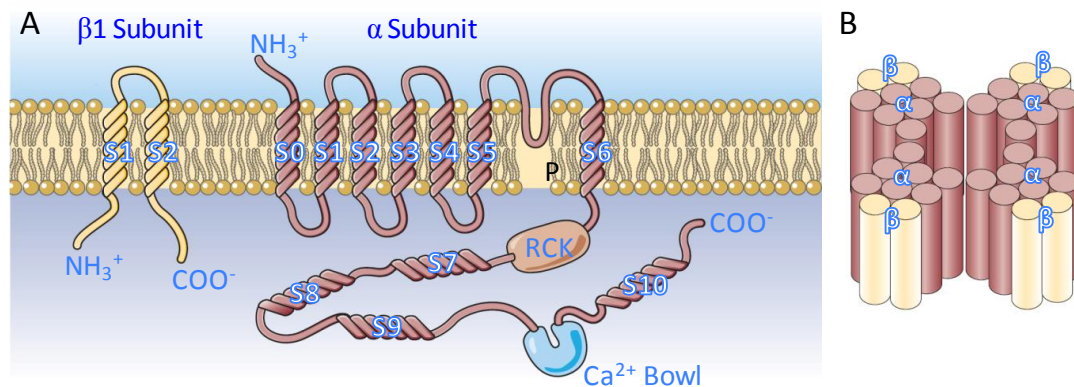
Figure 1. Schematic diagrams of BK channels
(A) Structures of α- and β1-subunit. There are 2 TM domains (S1, S2) in β1-subunit, and 11 hydrophobic domains (S0-S10) including 7 TM domains (S0-S6) in α-subunit with 1 pore region (P) located between S5 and S6. Besides, there are one Ca^{2+} bowl and at least one RCK domain located between the core and the tail region of the α-subunit. (B) Association of 4 α- and β1-subunits forms a native BK channel. (Modified from: Ledoux *et al.*, 2006)

As can be seen, with such structures, a BK channel naturally is a voltage-dependent K^+ selective channel. It is worth mentioning that the BK channel α-subunit has an extra TM domain, termed S0, leading to an external NH_2-terminus (Figure 1A), which not only means that the voltage sensor, though named S4, actually locates on the fifth TM

domain of each of four α-subunits, but also indicates that the extracellular interference factors may usually entwine the β-subunits. Because this NH_2-terminus along with the first TM domain is essential for the binding of β-subunits which will largely regulate the BK channel functions.

The Ca^{2+} dependency is a particular feature of BK channels which differs from the other channels in the superfamily. It is also determined by the special structures of the channel α-subunits, especially the large COOH-terminuses (~800 amino acids, 2/3 of the full length), each of which contains four predominantly hydrophobic domains. These hydrophobic domains are located intracellularly and contribute to both the RCK domains (the specialized intracellular motifs regulating the conductance of K^+ channels; Jiang *et al.*, 2001) and the Ca^{2+}-sensor domains, although the precise locations of Ca^{2+} binding sites remain unclear.

By using channel α chimeras and mutants, researchers so far have gradually identified two RCK domains and three distinct Ca^{2+}-dependent regulatory mechanisms with different divalent-cation selectivities in the COOH-terminus (reviewed by Latorre and Brauchi, 2006). A well studied high-affinity Ca^{2+}-binding site christened the "Ca^{2+} bowl" (Schreiber and Salkoff, 1997), which corresponds to five consecutive negatively charged aspartates (D894–D898; Schreiber *et al.*, 1999), has been newly identified as a key component composing one of the two RCK domains, termed RCK2 (Yusifov *et al.*, 2008). However, the other RCK domain (now called RCK1) which was discovered much earlier (Jiang *et al.*, 2001) encompasses also one high-affinity Ca^{2+}-sensing region which locates about 400 amino acids upstream the Ca^{2+} bowl and consists of two separate aspartates (D362, D367) and one methionine (M513; Xia *et al.*, 2002; Zeng *et al.*, 2005, Bao *et al.*, 2002). In a BK channel, each of the four α-subunits contributes two RCK domains including two high-affinity Ca^{2+}-binding regions forming a gating ring where two Ca^{2+} ions bind per subunit. Such complex structures convert the free energy of Ca^{2+} binding into mechanical work and open the channel when cytoplasmic Ca^{2+} reaches micromolar concentrations (Xia *et al.*, 2002; Magleby, 2003). A further

study reveals that the Ca^{2+} binding region on D362/D367 in RCK1 is also the target for Sr^{2+} and Cd^{2+} to activate BK channels (Zeng, 2005). Besides a third Ca^{2+}-binding region with low-affinity (in the millimolar range) is identified in RCK1, which consists of two salt bridges formed by two pairs of spatially adjacent amino acids (E374/H350 and E399/H344, Shi *et al.*, 2002), and which is additionally involved in the physiological regulation of BK channels by millimolar amounts of Mg^{2+} (Golowash *et al.*, 1986; Horrigan *et al.*, 1999). Furthermore, this low Ca^{2+} affinity site is also thought to be involved in Mn^{2+}, Fe^{2+}, Co^{2+}, and Ni^{2+} binding.

A functional BK channel is a complex (Figure 1B) composed of four α-subunits of homo-associations and four auxiliary β-subunits (Meera *et al.*, 1997; Knaus *et al.*, 1994; McManus, 1995; Salkoff *et al.*, 2006). Generally, there is only one gene in the genome of a species encoding BK α-subunit (Tian *et al.*, 2001; Chen *et al.*, 2005) and 1–4 genes encoding different β-subunits (Behrens *et al.*, 2000; Brenner *et al.*, 2000b; Poulsen *et al.*, 2009). However, most species have alternative splicing variants (Shipston, 2001; Fodor, 2009). And it is not necessary that all four α- or β-subunits are the same in a BK channel, in fact, it is still unclear in which conditions four subunits are of homo-associations and in which conditions they are of hetero-associations.

1.1.4 BK channel genes and alternative splice variants

The first BK channel gene was cloned in 1991 from the cDNA of a Drosophila gene, slowpoke1 (Atkinson *et al.*, 1991; Butler *et al.*, 1993), which encoded a BK channel α-subunit. Then in succession, many other clones of BK genes were reported in various other species covering from C. elegans to mammalian. Since BK channels are ubiquitous and share high sequence homology among all the BK genes, the name of the gene, Slo1 or Slowpoke, also gradually becomes the name of BK channels.

The official gene name of α-subunits is KCNMA1. In human genome, KCNMA1 locates on chromosome 10 from base pair 78,629,360 to 79,398,353 (Ensembl Gene ID: ENSG00000156113). So far 27 splice variants were identified and 5 of them were

too short to be real proteins. In mouse genome it is on chromosome 14 from base pair 24,117,983 to 24,622,525 (ENSMUSG00000063142) with 4 splice variants.

Human:

Gene Name	Alternative splicing	Ensembl Gene ID	UniProtKB/Swiss-Prot
KCNMA1	27	ENSG00000156113	Q12791
KCNMB1	1	ENSG00000145936	Q16558
KCNMB2	12	ENSG00000197584	Q9Y691
KCNMB3	7	ENSG00000171121	Q9NPA1
KCNMB4	1	ENSG00000135643	Q86W47

Mouse:

Gene Name	Alternative splicing	Ensembl Gene ID	UniProtKB/Swiss-Prot
KCNMA1	4	ENSMUSG00000063142	Q08460
KCNMB1	1	ENSMUSG00000020155	Q8CAE3
KCNMB2	4	ENSMUSG00000037610	Q9CZM9
KCNMB3	-	NF	-
KCNMB4	1	ENSMUSG00000054934	Q9JIN6

Xenopus tropicalis:

Gene Name	Alternative splicing	Ensembl Gene ID	UniProtKB/Swiss-Prot
KCNMA1	1	ENSXETG00000018041	Q90ZC7
KCNMB1	-	NF	-
KCNMB2	4	ENSXETG00000007250	NA
KCNMB3	-	NF	-
KCNMB4	1	ENSXETG00000011382	NA

Table 1. Summary of BK channel genes
There is 1 gene encoding BK α-subunit named KCNMA1, and 4 genes (KCNMB1-4) encoding β-subunit. NF = Not Found; NA = Not Available

In toad genomes, however, the situation is complicated, since different species usually have different chromosome numbers. *Xenopus laevis* is an allotetraploid species (Kobel and Du Pasquier, 1986) with 36 chromosomes (4n=36), meaning many genes are two pseudoalleles of four copies. Unfortunately, it is still unknown where the BK channel gene is in the genome of this species. It is worth pointing out that most available gene databases of toads came from a true diploid species, *Xenopus tropicalis* (Hirsch, 2002) which has 20 chromosomes (2n=20). For example, in "Ensembl" the assemble database for *Xenopus tropicalis* contains 19,501 scaffolds with an average coverage of 7.65

times of the whole genome; and KCNMA1 can be found on scaffold 265 from base pair 797,000 to 1,089,066 (ENSXETG00000018041). Despite only one transcript without splice variant being found in the database, it does not mean BK channels in Xenopus are simple, because the protein diversity of the β-subunits still exist (Table 1).

Alternative splicing in BK channel genes is an important discovery in both vertebrates and invertebrates. It mainly serves the function of fine tuning the action potential kinetics in neurons. For example, in cochlear hair cells in vertebrates, alternative splicing shows an exquisite art of sophisticated control in an organism. By strictly regulated post-transcriptional mechanisms, different exons encoding the same functional domains with different properties form functionally diverse splicing variants of BK channels which are precisely arranged in the individual hair cells along the tonotopic gradient of the Cochlea. These functional domains cover Ca^{2+} sensors, RCK- and P-domains, and S4 domains (the voltage sensor); and they are like the building blocks controlled by the alternative pre-mRNA splicing mechanisms, generating many BK channels with different kinetics, assembling and tuning the hair cells to resonate with frequencies of a large dynamic range. This tonotopic organization of BK channel α-subunits associated with different β-subunits (Ramanathan *et al.*, 1999) in non-mammalian vertebrates like amphibians, reptiles, and birds are the key step of generating the intrinsic frequency selectivity of the cochlear hair cell along the frequency-axis of the cochlea. In mammalians, it also appears in the inner hair cells and is responsible, with the help of a mechanical tuning structure, for transducing sound to the brain (Langer *et al.*, 2003; Pyott *et al.*, 2007).

An interesting discovery of BK channel alternative splicing is that during evolution the splicing is unlikely conserved in the gene structure across phyla, but occurs always at similar regions of a channel protein at experimentally established domain boundaries (Reviewed by Fodor, 2009), suggesting a prominent role for convergent evolution with splicing variants changed via changes in interdomain communication.

1.1.5 Functional properties of BK channels

BK channels have different electrophysiological properties in different tissues (Meredith *et al.*, 2004, Pattillo *et al.*, 2001, Shao *et al.*, 1999, Ricci *et al.*, 2000). Except for alternative splicing, modulation by tissue specific expressed β-subunits is another main reason. Until now, four different β-subunits (KCNMB1–4) have being discovered, and in Xenopus, only KCNMB2 and KCNMB4 are identified (Table 1).

Generally, products of KCNMB1 and KCNMB2 can enhance Ca^{2+} sensitivity of BK channels, which is critical for the proper regulation of smooth muscle tone (Brenner *et al.*, 2000b; Tseng-Crank *et al.*, 1996; Chang *et al.*, 1997; Jiang *et al.*, 1999; Wallner *et al.*, 1999; Xia *et al.*, 1999). KCNMB3 has several splicing variants and produces different β-subunits conferring different voltage dependencies on BK channels; besides, all of these β-subunits have an extracellular loop which is reported to cause a pronounced inward rectification of the currents (Zeng *et al.*, 2003; Brenner *et al.*, 2000a; Uebele *et al.*, 2000). KCNMB4, which expresses almost exclusively in the brain (Behrens *et al.*, 2000; Brenner *et al.*, 2006; Weiger *et al.*, 2000), produces β-subunits with different channel gating properties, which mainly slow down the kinetics of the channels and influences the APs (Ha *et al.*, 2004; Wang *et al.*, 2006; Pyott *et al.*, 2007).

BK channels are ubiquitously expressed in a wide variety of tissues in various species, mediating the genesis and regulation of the membrane voltage and modulating the action potential; and they are involved in a number of key physiological processes, like muscle contraction, auditory turning, neuronal excitability, neurosecretion, and transmitter release. It is noticeable that all of these processes need an increase in cytosolic Ca^{2+} to develop. That is true, because gating of BK channels is Ca^{2+} activated. Although, the voltage can open BK channels theoretically in the complete absence of Ca^{2+}, yet, practically in a physiological range of membrane potentials, the channel open probability is extremely low and just reaches a detectable threshold, which has almost no physiological meaning. However, binding of Ca^{2+} shifts many voltage-dependent

parameters of a BK channel to more negative voltages and allows it to function under physiological conditions (Cox *et al.*, 1997). In fact, there is a synergy between $[Ca^{2+}]_i$ and membrane potential, the higher the $[Ca^{2+}]_i$, the smaller the depolarization needed to activate the channel. Normally, the $[Ca^{2+}]_i$ above 10 µM is prerequisite, although Ca^{2+} can facilitate the gating of BK channels in a wide range up to millimolar. It is also worth mentioning that Ca^{2+} of high concentration can open a BK channel even when all its voltage sensors are in the resting configuration but presumably with a low open probability and no physiological meaning at all.

1.2 Ca^{2+} microdomains

It is conceivable that the BK channel functions are closely linked to Ca^{2+}. And, as compared to the intricacy of BK channels, cell Ca^{2+} signaling is also not simple.

1.2.1 Cytosolic Ca^{2+}

Ca^{2+} is one of the most abundant metals by mass in many organisms; and as a prototypically cytosolic second messenger, Ca^{2+} is ubiquitous in eukaryotes from yeast to human, playing important roles in cell signaling. It is now agreed that a long time evolution let cells adopt this positively charged single-atom cation, together with the other negatively charged anion, the phosphate ion, as two primary signaling elements. Because the most important substances of cells, the proteins, change their functions by the shape and charge, while either Ca^{2+} binding or phosphorylation will trigger changes in protein charges, thus in turn, altering the shapes or conformations and further the interactions (Westheimer, 1987; Clapham, 2007), so, gradually, using Ca^{2+} and phosphate ions to control local electrostatic fields and to modulate the protein conformations become the two universal tools of cells in signal transduction.

However, it is also the use of such two tools that makes cells avidly exclude the Ca^{2+} from the cytosol. It has been well known that cells invest a large amount of their energy to affect changes in $[Ca^{2+}]$, resulting in a 10,000-fold gradient maintained by the cells between their intracellular free $[Ca^{2+}]$ of about 100 nM and extracellular

$[Ca^{2+}]$ of about several mM. Such a high Ca^{2+} gradient across the cell membrane more or less underlies the efforts, the effectiveness, and the speed for Ca^{2+} exclusion by the cells. In contrast, the concentration of another divalent cation, Mg^{2+}, which is also an essential element in biological systems, barely differs across the cell membrane. For this strange phenomenon, one explanation is: because Ca^{2+} binds water much less tightly than Mg^{2+} does, and precipitates the phosphate. Thus, to avoid the precipitation of phosphate with Ca^{2+}, it is better to have low $[Ca^{2+}]$ in cytosol.

Besides, there are likely other reasons that also make cells eagerly remove the cytosolic Ca^{2+}. As a hydrophilic and ionic small messenger, Ca^{2+} ions are obviously diffusible, whereby rapidly and equivalently accessing all the cellular compartments is no doubt an excellent property for an intracellular messenger to relay signals. However, unlike cyclic adenosine monophosphate (cAMP), another important second messenger, which can be removed easily and effectively via hydrolysis catalyzed by phosphodiesterases, Ca^{2+} is only a small inorganic single-atom ion and can neither be catabolically degraded nor be anabolically synthesized. In addition, Ca^{2+} can trigger a wide variety of Ca^{2+}-dependent signaling events or reaction cascades, which, unfortunately, are sometimes of even opposing effects on cellular functions.

Hence, cells had to evolve ways to sequester such a dangerous divalent ion. Perhaps, an easy way is just to reduce its cytosolic levels and, when needed later for signaling, only to use its electrical currents when moving across a biological membrane (Cheng and Lederer, 2008) or binding energy (Clapham, 2007) after its influx or release into the cytosol.

1.2.2 Dynamic balance

Since Ca^{2+} cannot be generated by anabolic synthesis, nor can it be chemically altered by degradation, to exert control over Ca^{2+}, cells must transport, compartmentalize, extrude, or chelate it. And on the other hand, the free cytosolic Ca^{2+} is also a dynamic balance of the Ca^{2+} influx, Ca^{2+} release, Ca^{2+} sequestration and Ca^{2+} buffering.

In eukaryotic cells there are two major pathways to increase cytosolic Ca^{2+}, depending on the Ca^{2+} sources being outside or inside a cell. One is the Ca^{2+} influx through voltage-gated Ca^{2+} channels (VGCCs), nonselective cation channels, and some ionotropic receptors which can partially conduct Ca^{2+} ions. All these channels are generally found on the surface membrane of a cell. The other major pathway is the Ca^{2+} release from intracellular stores via inositol trisphosphate-gated channels (IP_3Rs) or ryanodine-gated channels (RyRs), both of which are usually located in the endoplasmic reticulum (ER) membrane inside a cell.

In comparison, to maintain the cytosolic $[Ca^{2+}]$ at a low level of around 100 nM, cells undertake more efforts and pay more energy. ATPase pumps are the main machines to push Ca^{2+} uphill for eternity either out of the cell or into the ER, the former via plasma membrane Ca^{2+} ATPases (PMCA pumps) and the latter via Sarco/Endoplasmic reticulum (SR/ER) Ca^{2+} ATPases (SERCA pumps). Besides, a second mechanism, the Na^+/Ca^{2+} exchangers (NCX) and Na^+/Ca^{2+}-K^+ exchangers (NCKX), exchange one Ca^{2+} ion for three Na^+ ions (NCX) or co-transport one K^+ ion with one Ca^{2+} ion in exchange for four Na^+ ions (NCKX), running in their "forward" modes, using inward Na^+ current to drive Ca^{2+} extrusion. A third way is the Ca^{2+} uptake by mitochondria, which, in fact, is not mediated by a pump or exchanger, but by a "Ca^{2+} uniporter" (Nicholls and Crompton, 1980), where the accumulation of Ca^{2+} into the mitochondrial matrix is driven by an electrochemical potential gradient across the inner mitochondrial membrane; and the potential gradient is usually estimated at ~200 mV negative to the cytosol, which is generated either by the respiratory chain or ATP (Adenosine-5'- triphosphate) hydrolysis.

In fact, all the above three methods will directly or indirectly use the energy from ATP. Now comes the fourth and most important way, the chelating of Ca^{2+} ions by Ca^{2+}-binding proteins, which does not use the ATP but the binding affinity coming from the specialized structural parts of the Ca^{2+}-binding proteins themselves. Most of these specialized structural parts are characterized by three Ca^{2+} regulatory motifs: 1)

the EF hand domain (a name after the E and F regions of parvalbumin; Nakayama and Kretsinger, 1994) which consists of a conserved Ca^{2+}-coordinating loop of 12 amino acids flanked on each side by short α-helical domains (Kretsinger, 1980); 2) the C2 domain which is a type of Ca^{2+} binding loops in a β-sandwich structure of ~120 amino acid segment composed of 8 β-strands (Cho and Stahelin, 2005); and 3) the annexin folds (a name from the annexin repeat, a 70 amino acid motif restricted to annexins) which typically consist of 4 tandem repeats folded into a compact domain of five α-helices (Gerke *et al.*, 2005). Emphasizing the importance of Ca^{2+}binding proteins is the finding that about only 1–5% of Ca^{2+} ions entering a cell shows up as free ions (Hodgkin and Keynes, 1957; Gorman and Thomas, 1980; McBurney and Neering, 1985; Ahmed and Connor, 1988; Zhou and Neher, 1993). This fourth way, also named a buffering way, is the fastest control mechanism for both the maintenance of a low cytosolic $[Ca^{2+}]$ and the Ca^{2+} signaling. Such a fast control mechanism will not only result in a diffusion-limited Ca^{2+} propagation from the Ca^{2+} sources, but also in many cases trigger the next cellular processes locally, which confers on the cells a key material basis for the compartmentalization of Ca^{2+} signaling.

1.2.3 Ca^{2+} microdomain separating Ca^{2+} signaling in time and space

There is now a growing awareness that in addition to just simply maintaining a low cytosolic $[Ca^{2+}]$ (though not really simple) as discussed above, a remarkable versatility of local Ca^{2+} signaling has also been developed by cells during their long evolution. This compartmentalized Ca^{2+} signaling is based on the local nature of functional Ca^{2+} microdomains, which elicit the local selectivities of Ca^{2+} responses to the large amount of promiscuous events, some of which may happen even not locally.

In the past few decades, plenty of elementary Ca^{2+} events have been observed in different parts of different cells. As a result, a great number of different names have also been increasingly generated in order to precisely describe those momentary and compartmentalized Ca^{2+} signals. Nevertheless, there are still common characteristics behind those Ca^{2+} events such as forming small functional elementary units or

domains, being momentary and compartmentalized. Such commonalities are now our general view of defining a Ca^{2+} microdomain as any Ca^{2+} signaling event that is localized to a specific small region of a cell (Rizzuto and Pozzan, 2006).

Name	Source	Location	Fuctions
Sparklet	VGCC	Surface membrane of cardiac cells[1]	Excitation–contraction (E–C) coupling
		Stereocila of hair cells[2]	Exocytosis particularly at synaptic endings
		Neocortical interneurons[3]	Transmitter release
Spark	RyRs	Cardiac cells[4]	E–C coupling
		Cerebellar basket cell[5]	Spontaneous Ca^{2+} transients
		Smooth muscle cell[6]	Activation of BK channels
Blink	RyRs	Lumen of the ER in muscle cells[7]	Depletion of Ca^{2+} within the lumen Inactivation of cardiac cell RyR_2s
Syntilla	RyRs	Presynaptic endings of hypothalamic neurons[8]	Release of hormones
Puff	IP_3Rs	Purkinje neurons[9]	Presynaptic Ca^{2+} release
		HeLa cell[10]	Intracellular Ca^{2+} waves

Table 2. Ca^{2+} elementary events that relate to functional Ca^{2+} microdomains
VGCC=Voltage-gated Ca^{2+} channel; RyRs= Ryanodine receptors; IP_3Rs= Inositol trisphosphate receptors. [1](Wang *et al.*, 2001); [2](Lumpkin and Hudspeth, 1998); [3](Goldberg *et al.*, 2003); [4](Cheng *et al.*, 1993); [5](Conti *et al.*, 2004); [6](Brenner *et al.*, 2000b); [7](Brochet *et al.*, 2004); [8](Crescenzo *et al.*, 2004); [9](Denk *et al.*, 1995); [10](Bootman *et al.*, 1997; Thomas *et al.*, 1998).

Table 2 summarizes the different names of those elementary Ca^{2+} events that relate to the functional Ca^{2+} microdomains (for review see Berridge, 2006). One thing should be mentioned that there are still more of them not listed in the table, as the elementary Ca^{2+} events are so universal that many different names may possibly refer to similar things (for review see Chen and Lederer, 2008). For example, a cluster of Ca^{2+} release channels, either RyRs or IP_3Rs or a mixture, in the SR/ER membrane is called a Ca^{2+} release unit (CRU), which has also other names like a "Couplon" or "Ca^{2+} synapse". And actually, it is more or less the microdomain of a Ca^{2+} spark. In addition, if only one RyR channel is involved, the Ca^{2+} spark is also called "Ca^{2+} ember" (González *et al.*, 2000), "Ca^{2+} quark" (Lipp and Niggli, 1998) or "Ca^{2+} glow" (Yao *et al.*, 2006). And if only one or a few IP_3Rs show a small Ca^{2+} puff, it is also named "Ca^{2+} blip" (Sun *et al.*,1998).

Besides, a backward spelling of "sparks" named "Ca^{2+} skraps" defines the Ca^{2+} microdomains of small local Ca^{2+} depleted areas inside Ca^{2+} stores where the authors expected mirror images of Ca^{2+} sparks while the results suggested a different kinetics of skraps rather than the mirror of sparks (Launikonis *et al.*, 2006). Other similar microdomains of Ca^{2+} depletion have also been found in ER of cardiac cells and named "Ca^{2+} scraps" (Shannon *et al.*,2003) describing a local fast Ca^{2+} diffusion equilibrium after the Ca^{2+} release.

Moreover, if a Ca^{2+} microdomain travels across many CRUs, a "Ca^{2+} wave" (Capogrossi *et al.*, 1988; Cheng *et al.*, 1996) or "Ca^{2+} wavelet" (Stuyvers *et al.*, 2005) occurs. And if some Ca^{2+} waves form an oscillation, a "Ca^{2+} clock" then appears. As to the "Ca^{2+} clock", there are two reports: one shows a repetitive appearance of Ca^{2+} microdomains being coupled to an "electrophysiological clock" formed mainly by BK channels in cardiac pacemaker cells (Lakatta *et al.*, 2006); and the other reveals a "Ca^{2+} clock" driven by a thermodynamically reversible Markovian process involving RyRs and Ca^{2+} induced Ca^{2+} release in normal cardiac myocytes (Wang *et al.*, 2002). These two reports undoubtedly illustrate the hidden complexities of the local Ca^{2+} signaling below the simple names.

It is already sufficient to show that elementary Ca^{2+} events are so widespread that almost every nook and corner of a cell will see their existence, forming the functional Ca^{2+} microdomains and completing the most important and complex Ca^{2+} compartmentalized signal transduction (Laude and Simpson, 2009).

1.2.4 Modeling of Ca^{2+} microdomains

Studies have shown that cytosolic Ca^{2+} binding proteins play an important part for the formation of Ca^{2+} microdomains. Based on the knowledge of Ca^{2+} reaction-diffusion equations, a model Ca^{2+} microdomain could be established to estimate the size of real Ca^{2+} microdomains. Usually, to calculate the Ca^{2+} concentration in a normal solution, a set of diffusion equations can be used (see Eq. 16–18, Appendix i), and the resulting

$[Ca^{2+}]$ is both a function of time and position. It could have been more complex inside a cell, since there were many different Ca^{2+} sources and Ca^{2+} binding proteins. However, there is a famous solution based on the analytical approximation to the steady-state Ca^{2+} profile near a Ca^{2+} channel (Neher, 1986), resulting in a time independent formula as: $[Ca^{2+}]_r = [Ca^{2+}]_\infty + \frac{i_{Total}}{4\pi F D_{Ca} r} e^{-\frac{r}{\lambda}}$ (Eq. 1, section 2.6), where $[Ca^{2+}]_\infty$ is the bulk Ca^{2+} concentration, i_{Total} is the average current of total Ca^{2+} influx, F is Faraday's constant, D_{Ca} is the diffusion constant of free Ca^{2+}, r is the calculated distance from the Ca^{2+} pole, and λ is the characteristic length of the buffer protein (for detail see Appendix i, Eq. 20).

A very simple model will be introduced based on this fomula. It is called a simple model because in the analytical approximation only one mobile Ca^{2+} buffer is assumed (see Eq.19, Appendix i). Nevertheless, in a place near the Ca^{2+} source where the Ca^{2+} transient is high, all binding proteins will bind with Ca^{2+} immediately. Thus, to treat all of them with an apparent diffusion constant and neglect their individual diffusion constants, will not lose the accuracy of the approximation in Eq.1. Moreover, the neglect of stationary or immobile buffers will also not influence the result of Eq. 1 a lot, since these buffers are fixed in space, Ca^{2+} binding to or release from them merely influences the bulk $[Ca^{2+}]$ which only prolongs the time needed to reach the steady-state (Wagner and Keizer, 1994; Smith, 1996).

With Eq. 1, the size of Ca^{2+} microdomains near single Ca^{2+} channels can be analytically calculated. Although there is one more difficulty that little is known about all the constants of cytosolic mobile Ca^{2+} buffers, the estimation still can be drawn by the knowledge that Ca^{2+} binding sites of most Ca^{2+} binding proteins are included within three Ca^{2+} regulatory motifs (EF hand domains, C2 domains and annexin folds) and most of those proteins show the apparent binding kinetics between the slow Ca^{2+} buffer, EGTA, and the fast Ca^{2+} buffer, BAPTA. For instance, the K_d and K_{on} values for calmodulin, the most ubiquitous cytosolic Ca^{2+} binding protein, are around 0.1-10

µM and 6×10^7 $M^{-1}s^{-1}$, respectively (Park *et al.*, 2008), and for calbindin, another abundant cytosolic Ca^{2+} binding protein, are around 1 µM and 3×10^7 $M^{-1}s^{-1}$, while those two values are 0.22 µM, 2.5×10^6 $M^{-1}s^{-1}$ for EGTA, and 0.50 µM, 4×10^8 $M^{-1}s^{-1}$ for BATPA (Wu *et al.*, 1996; Smith 1996). Thus, to calculate an upper limit value (the largest area), the slow dynamic constants from EGTA can just be used. Besides, it seems that the Ca^{2+} binding proteins are not uniformly distributed but likely condensed in the Ca^{2+} microdomains. Given a finding that half influence of buffering effects of endogenous proteins occurs by applying approximately 1 mM BAPTA, an assumption of a millimolar range, say 1 mM, of the endogenous buffers around a microdomain will be quite reasonable (Wu *et al.*, 1996 Smith 1996).

A $[Ca^{2+}]$ larger than 10 µM within the microdomain is further assumed, to design the model for the activation of a BK channel under physiological conditions (Cox *et al.*, 1997). Other constants and parameters are listed in section 2.6. The biggest estimate for the size of the Ca^{2+} microdomain can be seen as a spherical area with a radius of ~50 nm (For details, see section 2.6).

It is known that the size of a calmodulin molecule is around 40–50 Å, and the diameter of a Ca^{2+} channel or a BK channel is around 200–300 Å (estimated from a tetrameric Kv1.2; Long *et al.*, 2005). Given 1 nm=10 Å, a 500 Å in radius or 1000 Å in length can only accommodate, like side by side, 4 channels. Or in another case that one channel is in the center and one channel is at a distance of 500 Å, and in between there are 200–300 Å, which can accommodate 4–6 calmodulins. Such a size of the Ca^{2+} microdomain to the size of a channel and a calmodulin is just like the size of a 10-person elevator to the size of a person with maybe a suit case of a normal size.

1.3 BK channels and Ca^{2+} microdomains

1.3.1 Ca^{2+} microdomains coupling the VGCCs to BK channels

As introduced above Ca^{2+} microdomains make it possible for cells to have the most versatile Ca^{2+} signaling such that even opposing downstream functions can be present

in the same cells, and to have a high Ca^{2+} transient up to several mM within a small area while the bulk Ca^{2+} level is still ~100 nM. The variations in the patterning of Ca^{2+} microdomains greatly expand the second messenger repertoire that makes nearly nothing being impossible for this single-atom cation to do signaling inside the cells. From the above calculation, it may further be noticed that the normal functions of BK channels require Ca^{2+} channels located nearby. Otherwise, the intrinsic Ca^{2+}-dependency of BK channels would make little sense. To other words, those BK channels who do not reside close to a Ca^{2+} source or within a Ca^{2+} microdomain, may not have any direct effect but rather serve as a backup.

Practically, investigations using pharmacological and toxicological methods have proved many BK channel functions coupling to different types of VGCCs such as L-type (Prakriya and Lingle1999; Storm, 1987a), N-type (Marrion and Tavalin, 1998), and P/Q-type channels (Edgerton and Reinhart, 2003; Prakriya and Lingle, 1999; Womack *et al.*, 2004). Although all the above VGCCs can fuel BK channels in different cells, using simple toxin tests, one still cannot establish a close link of BK channel functions to Ca^{2+} microdomains. Nonetheless, the findings that the fast Ca^{2+} chelator, BAPTA, shows a greater ability as compared to EGTA in the interference of BK channel functions, which strongly suggests nanometer ranges of distances between BK channels and VGCCs (Lancaster and Nicoll, 1987; Müller *et al.*, 2007; Roberts, 1993; Storm, 1987b), ensure that Ca^{2+} microdomains indeed control the BK channels' life. Besides, there is also a new term, "nanodomain", to precisely define the size of such a functional Ca^{2+} microdomain (for review: Fakler and Adelman, 2008). In addition, there is even direct evidence showing the co-localization of ~90 BK and ~40 Ca^{2+} channels in one cluster by using a focal electrical recording in small membrane patches (Roberts *et al.*, 1990). Such clusters are spread as elementary functional units forming Ca^{2+} microdomains in the presynaptic active zones of hair cells playing a key function in electrical resonance of auditory signaling (Wu *et al.*, 1996; Bortolozzi *et al.*, 2008). Moreover, by using biochemical binding assays,

several other researchers have also identified selective co-assembly of BK and Ca^{2+} channels (or even subunits) forming macromolecular protein complexes. So far, $Ca_v1.2$ (L-type) (Grunnet and Kaufmann, 2004), $Ca_v2.1$ (P/Q-type) (Berkefeld *et al.*, 2006), $Ca_v2.2$ (N-type) (Loane *et al.*,2007), and $Ca_v\beta1$ (β-subunit of L-type channel) (Zou *et al.*, 2008) have been demonstrated in such complexes respectively, in not only heterologous expression systems but also rat brains, which further hints at an important function of a Ca^{2+} microdomain as a relatively independent local unit with all the necessary partners aggregated together.

1.3.2 Ca^{2+} sources in Ca^{2+} microdomains for BK channels

It is worth mentioning that besides the VGCCs, other Ca^{2+} sources have also been discovered to couple the BK channels. Metabotropic glutamate receptors (mGluRs) have been found to inhibit central neurons via BK channels (Chavis *et al.*, 1998; Fiorillo and Williams, 1998; Holmes *et al.*, 1996), and the Ca^{2+} source is mainly the intracellular Ca^{2+} stores and only partially L-type Ca^{2+} channels (Fagni *et al.*, 2000). Although the Ca^{2+} source is not the ionotropic channels formed by the mGluRs, ionotropic channels indeed can couple BK channels directly. A clear example that demonstrates the microdomains of such ionotropic channels with BK channels is in the rat olfactory bulb neurons, where N-methyl-D-aspartate receptors are the direct Ca^{2+} sources for BK channel activations (Isaacson and Murphy, 2001). Regarding the nonselective cation channels, the Ca^{2+} microdomain of stretch-activated channels (SACs) in smooth muscle cells of toad stomachs is another example where Ca^{2+} influx through SACs opens BK channels directly (Zou *et al.*, 2002).

1.3.3 Location of Ca^{2+} sources in Ca^{2+} microdomains

It is also worth mentioning that within a Ca^{2+} microdomain the aggregation of functional partners is not always necessary to form the complex. Sometimes they are not even in the same membrane. For example, in smooth muscle cells, the Ca^{2+} sparks formed by RyRs in the membrane of SRs modulate the cell-surface BK channels, controlling the muscle relaxations (Pérez *et al.*, 1999). A more detailed functioning

study shows that the modulation is related to the BK channel β-subunits controlled by a Ca^{2+}-induced Ca^{2+} release (Brenner 2000b). Here, a direct contact between BK channels and RyRs is unlikely, but their spatial adjacency still achieves the mission. It is thought that these two channels might be linked by a series of scaffold proteins that spanned a large distance (ZhuGe *et al.*, 2002). Given the fact that a normal muscle RyR-channel has a Ca^{2+} conductance of ~100 pS (Smith *et al.*, 1988), almost 20 more times higher than that of a usual VGCC which is several pS for Ca^{2+}, it is conceivable that the large distance between BK channels and RyRs should remain within the control of Ca^{2+} microdomains formed by RyRs.

Since all three types of RyRs show activities of Ca^{2+}-induced Ca^{2+} release triggered by VGCCs (Endo, 2009), the large distance between BK channels and RyRs plus the distance between RyRs and the original Ca^{2+} sources, the surface VGCCs, depicts a slow and delayed controlling model with long duration for BK channel activation: the Ca^{2+} influx via VGCCs does not activate BK channels directly but diffuses to RyRs and induces a second release of more Ca^{2+} ions, and then triggering the BK channel opening. As compared to the normal coupling model with only VGCCs and BK channels where the Ca^{2+} influx directly activates the BK channels, the coupling of RyRs and BK channels enables the Ca^{2+} influx not only to open the BK channels after a longer delay but also to keep them opening for a longer duration, which well fits into the control of tardive smooth muscle relaxations by BK channels.

1.3.4 Ca^{2+} microdomains and BK channels in olfactory systems

Although direct binding of a BK channel to a Ca^{2+} channel in the Ca^{2+} microdomain is an easy and reliable way for the opening of BK channels, such an immediate activation might not fit a circumstance that needs BK channels being activated with a long delay. However, indirect coupling can provide more options of different controls and, since Ca^{2+} is a diffusible second messenger, with indirect coupling, Ca^{2+} microdomains can be more flexibly organized.

It is well known that the durations of APs vary widely in different nervous systems. It is also known that the Ca^{2+} influx via VGCCs activated during each AP triggers the BK channels and feedback controls the APs including their durations (Storm, 1987b; Edgerton and Reinhart, 2003) and intervals in between (Lancaster and Nicoll, 1987; Storm, 1987a; Yazejian *et al.*, 2000), which is an important model for BK channel activation involved in signal transduction. Correspondingly, both the onset and duration of the BK channel activation may differ among different nervous systems. For instance, in hippocampal pyramidal neurons and granule neurons as well as in cerebellar Purkinje neurons (Shao *et al.*, 1999; Edgerton and Reinhart, 2003; Loane *et al.*, 2007; Müller *et al.*, 2007), BK channels are activated by short APs and keep opening for a few milliseconds, while in chromaffin cells (Lovell and McCobb, 2001), smooth muscle cells (Heppner *et al.*, 1997), suprachiasmatic nucleus neurons (Jackson *et al.*, 2004) and vomeronasal sensory neurons (Ukhanov *et al.*, 2007) the periods of BK channel openings extended to a few tens of milliseconds.

It is noticeable that in a short AP system, for example in hippocampal neurons (Loane *et al.*,2007) BK and Ca^{2+} channels are directly attached, whereas in findings of a slow BK channel activation, for example in smooth muscle cells (ZhuGe *et al.*, 2002) indirect coupling occurs. However, it is still unknown whether the precise control of a BK channel, especially the timing, is given by the diffusion time of the Ca^{2+} ions after their influx, though this is intuitively quite reasonable. And it is even more reasonable in slow systems with long duration APs, for the diffusional distance between the Ca^{2+} source and BK channels would be a perfect choice for cells to determine a long and reliable timing, which is one of our conclusions in the present study in olfactory receptor neurons, which exactly belong to a type of sensor systems with a slow response time (Laurent, 1999).

Olfaction is the sense of smell, the signal of which is proceeded in the olfactory nervous system, a "codec device" for odorant signaling, and the result of which is what we perceive as and what we call—the odor. Such a sensation starts from the binding of

odorants to their receptors located on the cilia of olfactory receptor neurons, generating a second set of messengers that causes excitations in these neurons. The odorant information which is likely encoded in the spikes of the excited neurons is then processed in the olfactory bulb and transmitted to higher centers in the brain.

Recently, the basic properties of an olfactory system have become clearer and clearer. For example, the number of natural odors is surely smaller than that of all possible odors including the endlessly growing new ones from the perfume labs; a person nonetheless can always perceive randomly synthesized mixtures of aroma compounds as distinct or meaningful odors. Moreover, the vision system may treat two images of random dots as two indistinguishable objects, whereas the olfactory system seems able to distinguish a large number of random-component mixtures by assigning in the brain a specific value or identity to each of them, and later, can recall those memories when smelling again. Essentially, this fact is what the perfume industry makes its living with (Laurent, 1999).

On the other hand, the vision system can distinguish very short events. That is why a movie needs to run at least 30 frames per second, otherwise the audiences may feel an apparent rotation or wobble. But imagining, if a person already learned to assign odors or concentrations to letters or words, how fast can he or she "see" by means of smelling?

The olfaction is poor at following many or rapidly changing signals (Laurent, 1999). Starting from the first step of the signaling (the diffusion of the odorants passing through the mucous layer and reaching the cilia then the receptors) already makes olfaction a low-bandwidth sense.

Many studies in the olfactory systems have been done in the past few decades (> 35,500 records in PubMed, till 2010), but very few are related to BK channels (15 records). Except for the expression and appearance of the currents, with regard to BK

channel functions in olfactory receptor neurons, to our knowledge there has been only one study where the author uses enzymatically dissociated newt neurons. The study showed that blocking BK channels increased the firing rate induced by current injections, and the author suggested the BK channels to function in the regulation of odor adaptation (Kawai, 2002).

On the other hand, BK channel functions are always closely related to Ca^{2+} channels, but there are almost no studies on BK channel and Ca^{2+} channel relations and functions in olfactory neurons. Given the widespread influence of BK channels on signal transduction in many preparations and the few BK and Ca^{2+} channels being expressed in olfactory receptor neurons (Schild, 1998), their functions seem more enigmatic. Regarding that previous finding, the dissociation may impair the cilia of the neurons and the enzyme may also change the BK channel properties (Armstrong and Roberts, 2001).

Thus, in the present study, intact olfactory receptor neurons in a slice preparation are used. What is interesting is that in olfactory receptor neurons BK channels are co-localized with voltage-dependent Ca^{2+} microdomains; and the distances between BK and Ca^{2+} channels is presumably around 50 to 200 nm but no less than 30 nm. To compensate these long diffusional distances, Ca^{2+} microdomains may likely comprise Ca^{2+}-channel clusters rather than single Ca^{2+} channels. With this advantage, several tens of BK and Ca^{2+} channels seems already enough to achieve key functions in olfactory signaling, shaping the APs and facilitating the spiking rates.

2. Materials and Methods

2.1 Animal model - *Xenopus laevis*

The African clawed frog, *Xenopus laevis* (also known as the platanna), is a species of South African aquatic frog of the genus *Xenopus*, which is the animal class Amphibia and order Anura. *Xenopus laevis* is one of the classic animal models for neurobiology and is even more successful in researches on olfactory system during its larval stages. It is easy to make a nose-olfactory bulb preparation, since a tadpole in larval stages has a quite transparent body and no bony structure separates the olfactory mucosa from the olfactory bulb. And all experiments can be carried out at room temperature, since *Xenopus* is a poikilothermal animal and no need to maintain a temperature above 30˚C like in most neurobiological experiments for mammalians.

Adult frogs bought from a commercial supplier (Kaehler, Hamburg, Germany) were raised in 150-l glass aquaria (10–20 animals per aquarium). The animal rooms were kept at 19–20˚C and around 80–90% humidity, with a 12-hr light/dark cycle. The water temperature was 20˚C. The frogs were fed with Pondstick food (Tetra Pond, Melle, Germany) and sometimes with small pieces of bovine heart.

All animal care and experimental procedures were conducted according to the guidelines of the Goettingen University Committee for Ethics in Animal Experimentation. Great efforts were made to minimize the number of animals used.

2.2 Slice preparation

Xenopus laevis tadpoles (stages 51–54) were anesthetized by immersion in a mixture of water and ice for 3 min, and killed by decapitated. A tissue block (Figure 2A, red quadrangle) including the olfactory mucosa, the olfactory nerves and the anterior 2/3 of the brain which contained the olfactory bulb was cut out and kept in cold bath solution (see below). According to the body size and the shape of the mucosa, a horizontal piece of 150–180 μm was sliced off with a vibratome (VT 1200S; Leica, Bensheim,

Germany), and the left part which included the olfactory epithelium was dissected horizontally into a 200-μm thick slice for future use. The slices were left in bath solution at room temperature for at least 20 minutes before used in the experiments.
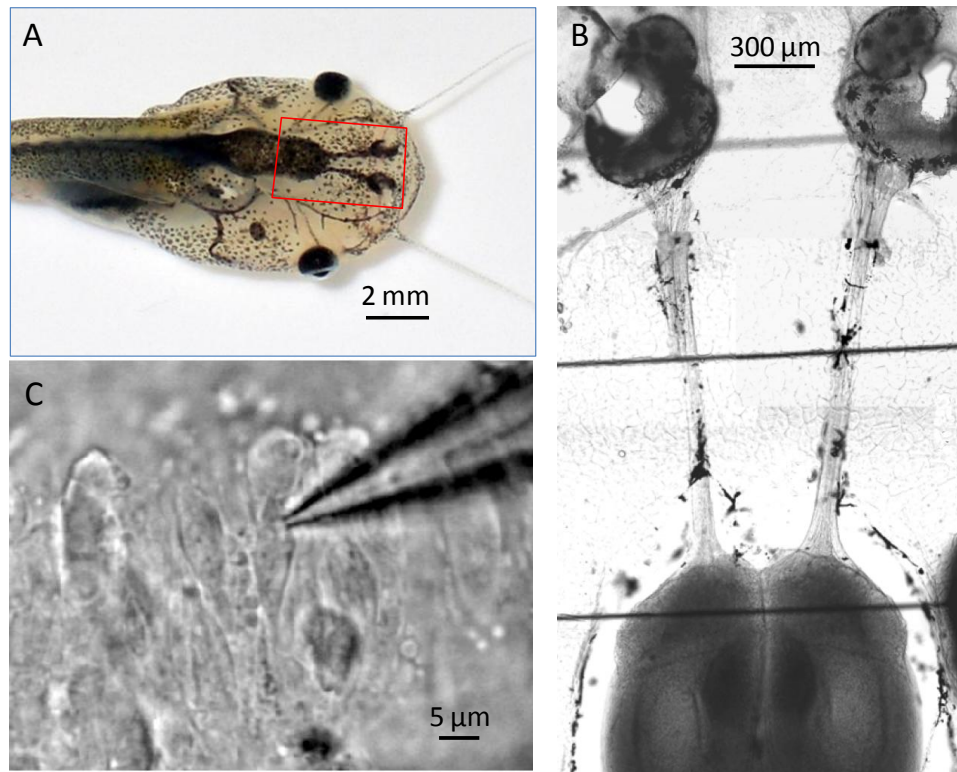
Figure 2. *Xenopus laevis* tadpole and the slice preparation
(A) *Xenopus laevis* tadpole (stage 53). (B) A typical mucosa slice with left and right olfactory mucosae cut as indicated by the red rectangle in A. (C) Slice with a patch pipette on the membrane of one olfactory receptor neuron.

2.3 Electrophysiology

All electrophysiological experiments were carried out at room temperature. Slices were placed in a recording chamber superfused with bath solution applied by gravity into the chamber. Odorants or other drugs were pipetted directly into a funnel drug applicator whose outflow was through a syringe needle placed close to the basal region of the olfactory epithelium. Neurons were visualized with an upright microscope (BX-51WI, Olympus) and monitored on the computer via a CCD camera.

Whole-cell and cell-attached patch-clamp recordings in tissue slices were done as described in Chen *et al.* (2009, PNAS). Briefly, microelectrodes (6–8 MΩ) were pulled from borosilicate glass capillaries (OD 1.2 mm) using a horizontal puller (PC-97, Sutter Instruments, Novato, CA, USA). For experiments in the cell-attached (on-cell) configuration, microelectrodes were filled with bath solution, and for whole-cell recordings the intracellular solutions are listed in Table 3. For combined patch-clamp/imaging experiments, Fluo-5f (100–200 μM) was added to a Cs^+-based intracellular solution.

An EPC-9 patch-claim amplifier (HEKA Electronics, Germany) equipped with *Patchmaster* software (HEKA Electronics, Germany) was used for data acquisition. In cell-attached mode, cells were voltage clamped at 0 mV. After a giga-seal was achieved another 5 min was usually waited in order to get a stable seal resistance (typically >5 GΩ). The currents were sampled at 10 kHz with two digital filters of the amplifier set at 10 kHz (Bessel) and 2.9 kHz (Bessel). In whole-cell recording mode, after the whole-cell configuration was established, cells were voltage clamped at -70 mV. Experiments were initiated only after the access resistance had stabilized (typically 12–20 MΩ). Liquid-junction potential, leak current (P/n protocol), fast and slow capacitances, and series resistance were corrected on-line (Sigworth *et al.*, 1995). The currents were sampled at 20 kHz and filtered at 10 kHz and 5.9 kHz. Data were exported to Matlab (The Math Works, USA) for subsequent analyses.

2.4 Confocal calcium imaging

In order to have a high temporal resolution, confocal calcium imaging was performed using a spinning-disk scanning unit (CSU-21, Perkin Elmer) mounted on an upright microscope (BX-51WI, Olympus) equipped with two water immersion objectives (40×, NA 1.2; 60×, NA 0.9; All Olympus) and a 50-mW, 488-nm, solid-state laser (Cyan, Newport-Spectraphysics). Images were taken by a cooled CCD camera (Orca-ER, Hammamatsu), controlled by the *UltraVIEW* software (Perkin Elmer).

2.4.1 Calcium imaging using the whole-cell configuration

Calcium imaging is designed to show the Ca^{2+} status of a tissue or medium. It takes advantage of Ca^{2+} indicators that can respond to the binding of Ca^{2+} ions by changing their spectral properties. There are numbers of different Ca^{2+} indicators with various Ca^{2+} binding affinities and different excitation or emission spectrums. High-affinity indicators are usually used to quantify low $[Ca^{2+}]$ in cytosol, however, they sometimes do not necessarily reveal true spatial gradients of Ca^{2+} concentration, as their low K_d values likely lead to a quick saturation in the vicinity of Ca^{2+} entry sites, and their slow Ca^{2+}-binding off-rates make them unable to reliably track the decay time course of Ca^{2+} transients. In the present study, a low-affinity indicator, Fluo-5f (K_d ~2.3 μM), was applied directly to the intracellular solution for calcium imaging, which was also combined with the whole-cell configuration in order to get voltage-dependent Ca^{2+} signals. To synchronize the imaging and the patch-clamp recording, the patch-clamp amplifier was controlled by the imaging software via external triggers.

2.4.2 Spinning-disk technology

The spinning-disk technology is established on a Nipkow disk platform, which was invented in 1884 and adapted for optical microscopy in 1968 (Petran *et al.*, 1968). In general, a spinning-disk confocal scanner uses a pair of rotating disks with thousands of pinholes in a spiral Archimedes. In the present research, the scanner is even improved by a Yokogawa patent with its second disk fitted with microlenses (Figure 3). Such innovation has markedly reduced the problem of irradiation efficiency and enables the scanning speed up to as fast as 1000 frames/sec (Ichihara *et al.*, 1996; Tanaami *et al.*, 2002; reviewed by Nakano, 2002).

In essence, the spinning-disk apparatus is based on the same principle as a confocal laser scanning microscopy (cLSM) to obtain confocal images. As light is projected on to the disk of microlens array, the microlenses trace the concentric arcs of excitation light passing through small pinholes in the disk of pinhole array and going through objective lens across the sample. Then, fluorescence emission from the sample returns

along the same light-path through the objective lens and the same pinholes which eliminate the out-of-focus light. The passed emission is in turn reflected by a dichroic mirror through a relay lens to the detector (Figure 3). Since the light axis never moves during scanning, fluorescent signals will produce in the detector position a real image which can be directly viewed by eye or captured by a CCD camera. Besides, the spinning-disk apparatus collects multiple points simultaneously rather than scanning a single point at a time, which means the technique is not only fast but also let the sample get a low dose of laser light. As the whole field of view is scanned during a single camera exposure, a high quality confocal image will be formed very quickly, making this technique highly suitable for live cell imaging and for weakly expressing samples which are prone to photobleaching.
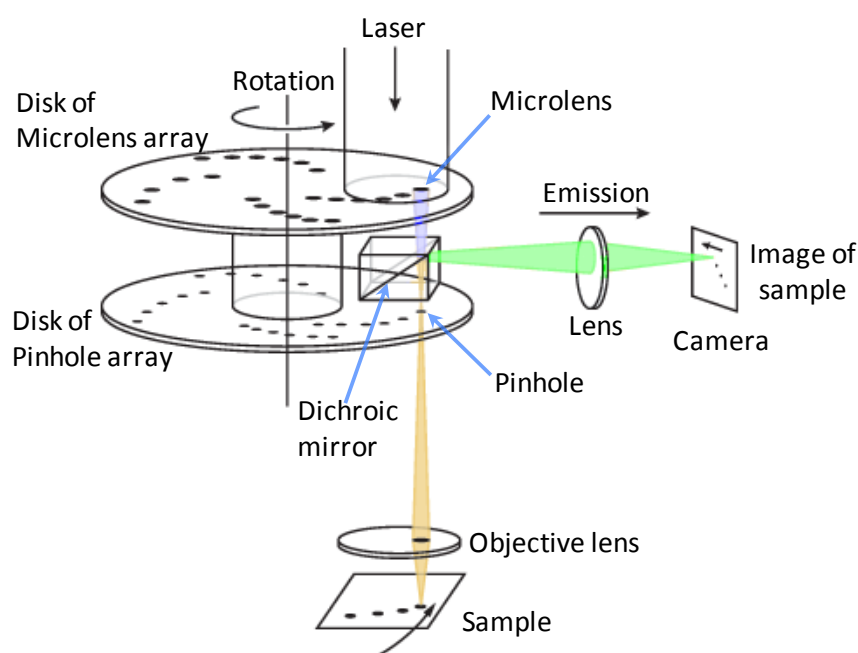
Figure 3. Schematic diagram of a spinning-disk cLSM with microlens
A Nipkow disk with microlenses (Yokogawa patents) is shown (the upper disk). The excitation light pathway is labeled as blue, the emission pathway is labeled as green, and their overlapping is marked as yellow. (Modified from: Nakano, 2002)

2.5 Imaging BK channels

A BK channel blocker, IbTx, was labeled with Alexa Fluor dyes to identify the surface

BK channels in either fixed or living slices.

2.5.1 Labeling Iberiotoxin

IbTx was labeled with either Alexa 546 or Alexa 488 according to the protocol of the labeling kit (Molecular Probes, Leiden, The Netherlands). Alexa labeled IbTx was purified and concentrated by FPLC and subsequent centrifugal filtering (molecular weight cutoff at 3 kDa; Vivaspin 500, Sartorius Stedim Biotech GmbH, Goettingen, Germany). The number of fluorophores per IbTx was estimated by photobleaching of Alexa 546 labeled IbTx using a confocal laser scanning microscope (Gennerich and Schild, 2005), a method similar to a previous report (Matthew, 2004) with the following modifications. First, Alexa 546 and the labeled IbTx were spin-coated on to clean glass cover slips at a concentration of ~0.5 nM, the concentrations being assessed by fluorescence correlation spectroscopy (Gennerich and Schild, 2002). Second, during the photobleaching, 5–7 focal planes covering a thickness of 2–3 μm in 0.4-μm intervals were collected for each time point in order to reduce the error from out-of-focus regions (Weigel *et al.*, 2009). Last, the 4D image stacks were analyzed with a global shift correction.

2.5.2 Staining BK channels

BK channels in fixed slices were stained with Alexa 546 labeled IbTx; and control slices were stained with Alexa 546 alone. Slices were fixed with paraformaldehyde (3%, 5 min, 4˚C) and then stained with either labeled IbTx or Alexa alone (500 nM–10 μM, 5–15 min, 4 ˚C) followed by 3 times washing in phosphate buffered saline (PBS, 5 min, each). After the last washing, the slices were mounted onto glass slides with 0.17 mm cover slips.

For staining in living slices, Alexa 488 labeled IbTx was used. All staining steps were similar as described in fixed samples, except that there was no fixation process and the PBS was replaced with the standard bath solution. After staining, the slices were washed in the bath solution for about 5–10 min before imaging; and after imaging, the

bath solution was still applied for at least another 10–15 min before the whole-cell recording and Ca^{2+} imaging.

2.6 Ca^{2+} microdomain modeling

The size of Ca^{2+} microdomains is estimated by a model based on a steady-state assumption near an open Ca^{2+} channel. The assumption includes: 1) there is only one mobile buffer with unsaturable state, and its concentration is constant in space and time; 2) the Ca^{2+} influx and diffusion reach a stead-stare; 3) the average current of Ca^{2+} influx is constant; and 4) the bulk Ca^{2+} concentration of cytosolic free Ca^{2+} is very low as compared to that of the buffer molecules and keep constant. With such a steady-state assumption, the model can be described by the following equations (Neher, 1986; Wagner and Keizer, 1994; Smith, 1996):

$$[Ca^{2+}]_r = [Ca^{2+}]_\infty + \frac{i_{Total}}{4\pi F D_{Ca} r} e^{-\frac{r}{\lambda}} \tag{1}$$

$$\text{and} \quad \lambda = \sqrt{\frac{D_{Ca}}{K_{on}[B]}}, \quad [B] = \frac{B_{Total} K_d}{[Ca^{2+}]_\infty + K_d}, \quad K_d = \frac{K_{off}}{K_{on}}$$

where $[Ca^{2+}]_\infty$ is the bulk Ca^{2+} concentration, i_{Total} is the average current of total Ca^{2+} influx, F is Faraday's constant, D_{Ca} is the diffusion constant of free Ca^{2+}, and r is the calculated distance from the Ca^{2+} pole. In these equations K_{on} and K_{off} are association and dissociation constants for the mobile Ca^{2+} buffer and λ is its characteristic length, [B] and B_{Total} are its free and total concentration, and K_d is its equilibrium binding constant. An easy mathematical deduction on how to obtain the equations is given at Appendix i.

A model Ca^{2+} microdomain is studied using Eq.1. The model assumes that: 1) there is only one Ca^{2+} channel in the center of the Ca^{2+} microdomain and the average total Ca^{2+} current is $i_{Total} = 0.3$ pA, which is calculated from a 3-pS channel under an average driving force of 100 mV with an open probability of 1; 2) the Ca^{2+} concentration for the Ca^{2+} microdomain is larger than 10 μM, the condition designed to have BK channels activated under physiological membrane potential (Cox *et al.*,

1997); and 3) the diffusion constant for free Ca^{2+} is $D_{Ca} = 400 \ \mu m^2 s^{-1}$, and the bulk Ca^{2+} concentration is $[Ca^{2+}]_\infty = 100$ nM (Wager, 1994; Smith, 1996). Thus, Eq.1 can be rewritten as:

$$[Ca^{2+}]_r = [Ca^{2+}]_\infty + \frac{i_{Total}}{4\pi F D_{Ca} r} e^{-\frac{r}{\lambda}} > 10 \ \mu M \implies \frac{1}{r} e^{-\frac{r}{\lambda}} > \frac{4\pi F D_{Ca} \left(10 \ \mu M - [Ca^{2+}]_\infty \right)}{i_{Total}}$$

Given $B_{Total}=1$ mM, $K_d=0.22 \ \mu M$ and $K_{on}=2.5 \times 10^6 \ M^{-1} s^{-1}$ (See section 1.2.4), the best guess will be r < 47 nm.

2.7 Variance analysis

2.7.1 Ca^{2+} tail currents

A Ca^{2+} channel normally cannot be simply described by two states like open and close. However, in some circumstance, it indeed can be treated as simple as two states, either open or close. One line of evidence is the Ca^{2+} tail current. It is often characterized by a single exponential decay which indicates, at that moment, the Ca^{2+} channel has simply two states and the state-shifting is a simple reaction or an elementary reaction. To prove, one can assume an elementary reaction with two states as open (O) and close (C):

$$O \underset{K_2}{\overset{K_1}{\rightleftharpoons}} C$$
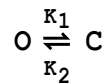
where K_1 and K_2 are the reaction rate coefficients. A reaction equation can be immediately defined:

$$\frac{d[O]}{dt} = K_2[C] - K_1[O] \tag{2}$$

In Eq. 2, [C] and [O] are the channel numbers in the open and close state, and should obey a mass balance equation: $[O] + [C] = [O]_0$, where $[O]_0$ is the total channel number. Given a starting point such as all channels are open at t=0, Eq. 2 can be calculated:

$$\frac{d[O]}{dt} = K_2([O]_0 - [O]) - K_1[O] \iff \frac{d[O]}{[O] - \frac{K_2}{K_1+K_2}[O]_0} = -(K_1 + K_2)dt$$

$$\xrightarrow{[O]_{t=0}=[O]_0} [O](t) = \frac{[O]_0}{(K_1 + K_2)} \left[K_2 + K_1 e^{-(K_1+K_2)t} \right] \tag{3}$$

Since the deduction is bidirectional, if a reaction shows a single exponential decay, it can also be described as an eliminatory reaction with only a single reaction step.

If each channel has same single channel current, i, the total current will be:

$$I(t) = i[O] = \frac{i[O]_0}{(K_1 + K_2)}\left[K_2 + K_1 e^{-(K_1+K_2)t}\right] \tag{4}$$

Eq. 4 shows that the tail current is a function of time with a single exponential decay. Based on this equation, the open probability at a certain membrane potential can be estimated.

2.7.2 Variance analysis of Ca^{2+} currents

Suppose that a Ca^{2+} channel has simply two states and all channels are independent, therewith, the channel open and close events will follow a binomial distribution such that the current and its variance will match the following equations (Neher and Stevens, 1977):

$$I(t) = N\, i\, P_o(t) \tag{5}$$

$$\sigma^2(t) = N\, i^2 P_o(t)[1 - P_o(t)] \tag{6}$$

where I(t), the current, $P_o(t)$, the open probability, and $\sigma^2(t)$, the variance of current, are all functions of time; N is the channel number and i is the single channel current. Eq. 5 and 6 can be rewritten to:

$$\sigma^2(t) = -I(t)^2/N + I(t)i \quad \text{or} \quad \sigma^2(t) = I(t)i[1 - P_o(t)].$$

As there are usually additional, independent noise sources, their variance has to be added, giving:

$$\sigma^2(t) = -I(t)^2/N + I(t)i + \sigma_0^2 \tag{7a}$$

$$\text{or} \quad \sigma^2(t) = I(t)i[1 - P_o(t)] + \sigma_0^2 \tag{7b}.$$

These equations were used in two ways. 1) In nonstationary fluctuation analysis of Ca^{2+} tail currents, the current mean and its variance on each isochrone, calculated as $\langle I \rangle$ and Vat(I), were fitted using Eq.7a as

$$Vat(I) = -\frac{\langle I \rangle^2}{N} + i\langle I \rangle + \sigma_0^2 \tag{8}$$

thereby the channel number, N, and the single channel current, i, could be obtained as

fit parameters. 2) For a steady-state Ca^{2+} current, the time average of the current and its variance were fitted using Eq. 7b as

$$Var(I) = \langle I \rangle k + \sigma_0^2 \tag{9}$$

$$\text{and} \quad k = i(1 - P_o) \tag{10}$$

Under steady-state voltage-clamp conditions both i and P_o are constant, and the average variance is proportional to the average current and thus number of channels, N.

Usually, the Ca^{2+} current may decrease unexpectedly during data collection; this problem is called channel rundown. A correction to calculate the variance relies on measurements of the differences in the current of successive trials as:

$$y_j = \frac{1}{2}[x_j(t) - x_{j+1}(t)] , \quad j \in [1, M-1]$$

$$Var(I) = \frac{2}{M-1} \sum_{j=1}^{M-1}(y_j - \langle y \rangle)^2 , \quad \langle y \rangle = \frac{1}{M-1} \sum_{j=1}^{M-1} y_j \tag{11}$$

or:

$$Var(I) = \frac{1}{2(M-1)} \sum_{j=1}^{M-1}[x_j(t) - x_{j+1}(t)]^2 - \frac{1}{2}\left[\frac{x_1(t) - x_M(t)}{M-1}\right]^2 \tag{12}$$

where $x_j(t)$ is the *j*th point along the isochrone at time t, M is the total number of the trials (Alvarez *et al.*, 2002). Eq. 11 is actually equivalent to Eq. 12, as:

$$\frac{2}{M-1} \sum_{j=1}^{M-1}(y_j - \langle y \rangle)^2 = \frac{2}{M-1}\left(\sum_{j=1}^{M-1} y_j{}^2 - \sum_{j=1}^{M-1}\langle y \rangle^2\right)$$

$$= \frac{1}{2(M-1)} \sum_{j=1}^{M-1}[x_j(t) - x_{j+1}(t)]^2 - \frac{1}{2}\left[\frac{x_1(t) - x_M(t)}{M-1}\right]^2 \quad \to (12)$$

If rundown is small, it is enough to use only the first part to calculate the Var(I) as:

$$Var(I) = \frac{1}{2(M-1)} \sum_{j=1}^{M-1}[x_j(t) - x_{j+1}(t)]^2.$$

2.7.3 Variance analysis of Fluorescence

To analyze the number of Ca^{2+} channels per Ca^{2+} microdomain, ORNs were

repetitively depolarized in the whole-cell configuration from -70 mV to -10 mV for 200 ms, and the average of the resulting fluorescence signal $\langle F \rangle$ and its variance σ_F^2 were measured. The measured variance comprises three components (from three independent stochastic processes): $\sigma_F^2 = \sigma_d^2 + \sigma_{sn}^2 + \sigma_{F,\Delta[Ca]}^2$, namely (i) a constant dark noise variance, (ii) a shot noise variance increasing linearly with the average fluorescence, and (iii) a variance depending on the change of Ca^{2+} concentration ($\Delta[Ca^{2+}]$), $\sigma_{F,\Delta[Ca]}^2$, indicated by the Ca^{2+} dye (Sabatini and Svoboda, 2000). The dark noise was measured with the shutter closed and the shot noise was estimated by fitting a line to the plot of fluorescence variance versus mean measured from various Ca^{2+} solutions where both $\Delta[Ca^{2+}]$ and $\sigma_{F,\Delta[Ca]}^2 = 0$. The fit result is $\sigma_{sn}^2 = q\langle F \rangle$, where q (the slope) stands for the device detector gain for a single photon.

If the Ca^{2+} dye is not saturated, the change of fluorescence ΔF and $\Delta[Ca^{2+}]$ are linearly related. Thus, the coefficient of variation of $\Delta[Ca^{2+}]$ can be calculated:

$$CV_{\Delta[Ca]} = CV_{F,\Delta[Ca]} = \frac{\sigma_{F,\Delta[Ca]}}{\langle F \rangle - F_0} = \frac{\sqrt{\sigma_F^2 - \sigma_d^2 - \sigma_{sn}^2}}{\langle F \rangle - F_0} = \frac{\sqrt{\sigma_F^2 - \sigma_d^2 - q\langle F \rangle}}{\langle \Delta F \rangle}.$$

As stationary process of channel openings and closings follow binomial statistics, if N independent Ca^{2+} channels have a same open probability p, the average number of open channels $\langle N_{open} \rangle$ and its variance σ_{open}^2 are given by

$$\langle N_{open} \rangle = Np \quad \text{and} \quad \sigma_{open}^2 = Np(1 - p),$$

from which the coefficient of variance is calculated:

$$CV_{open} = \frac{\sigma_{open}}{\langle N_{open} \rangle} = \frac{\sqrt{Np(1 - p)}}{Np} = \sqrt{\frac{(1 - p)}{Np}} \tag{13}$$

Here, a piecewise stationary binomial process such as the channel open and close events within the repetitive image acquisition (of 20-ms length) in the same experiment is not distinguished from the stationary binomial process and is neglected. The resulting error, which can be assumed to be approximately 5% (Sabatini and Svoboda, 2000), is thus irrelevant for the results.

It is also assumed that imaging is done far away from dye saturation, so that increases in $[Ca^{2+}]$ give proportional increases in fluorescence. As the coefficients of variation of linearly scaled stochastic processes are equal, the following equation can be got:

$$CV_{open}{}^2 = CV^2_{\Delta[Ca]} = CV^2_{F,\Delta[Ca]} \quad \text{or} \quad \frac{(1-p)}{Np} = CV^2_{F,\Delta[Ca]} \tag{14}$$

As p is known from the above voltage-clamp experiments at -10 mV, and the coefficient of variance results from the fluorescence measurement, the number of channels per microdomain can be obtained :

$$N = \frac{1 - p_{open}}{p_{open} \times CV^2_{F,\Delta[Ca]}} = \frac{1}{CV^2_{F,\Delta[Ca]}} \left(\frac{1}{p_{open}} - 1 \right) \tag{15}$$

Here, $p_{open}=p$ suggests the open probability of the channels.

2.8 Data analysis

All data analysis was performed in Matlab (The Math Works, USA) using custom algorithms written as either C++ functions or M-functions (Matlab-code functions).

2.8.1 Selection of regions of interest

Fluorescent images were first corrected with the shift along the time dimension whenever necessary using a custom-written routine. Then, the data were transformed into either $\Delta F = F(t) - F_0$ or $\frac{\Delta F}{F_0} = \frac{F(t) - F_0}{F_0}$ forms after subtraction of the background. F_0 was determined pixelwise as the mean intensity from the first 3 s of the data.

Ca^{2+} influx upon depolarizing pulses was assessed and spotted by pixelwise crosscorrelating the fluorescence intensity $I_{x,y}(t)(t = 1, ..., T)$ with the average depolarization pulse $S(t)(t = 1, ..., T)$, as

$$C(x, y, t) = \frac{\mathcal{F}^{-1}\{\mathcal{F}[I_{x,y}(t)] \cdot \mathcal{F}^*[S(t)]\}}{\langle I_{x,y}(t) \rangle \langle S(t) \rangle}$$

where $\mathcal{F}$ represents the Fourier transform, $\mathcal{F}^{-1}$ is the inverse Fourier transform, and $\mathcal{F}^*$ is its complex conjugate. The image at time-lag zero, $C(x, y, 0)$, is used as a

guide for placing the regions of interest (ROIs).

2.9 Solutions

The standard bath solution contained (in mM): 98 NaCl, 2 KCl, 1 $CaCl_2$, 2 $MgCl_2$, 5 glucose, 5 sodium pyruvate and 10 HEPES (pH 7.8, 230 mOsm). The PBS solution contained (in mM): 137 NaCl, 2.7 KCl, 8 NaH_2PO_4 and 1.4 KH_2PO_4 (pH 7.4). All intercellular solutions are listed in Table 3.

The mixture of amino acids was prepared in bath solution and contained all the following L-amino acids besides glycine: alanine, arginine, cysteine, histidine, isoleucine, leucine, lysine, methionine, phenylalanine, proline, serine, threonine, tryptophan and valine (200 µM of each).

Iberiotoxin (IbTX) and Charybdotoxin (ChTX) were dissolved in dimethyl sulfoxide (DMSO, 0.1 mM stock), stored at -20 ℃ and diluted to their final concentrations in standard bath solution before use (final [DMSO] < 0.2%). Tetrodotoxin (TTX) were dissolved as 1 mM stock solution in distilled water and stored at -20 ℃. Nimodipine (20 µM) was prepared fresh daily from a 20 mM stock solution (in DMSO), and the related experiments were carried out in the dark.

IbTx, ChTx and TTX were purchased from Alomone Labs (Alomone Labs Ltd. Jerusalem, Israel). All the other chemical compounds were bought from Sigma Chemicals (Sigma-Aldrich, Deisenhofen, Germany).

Name	BAPTA 10 mM	EGTA 10 mM	EGTA 1.2 mM	Fluo-5F 2 mM	Fluo-5F EGTA	Cs	Cs Fluo-5f
KCl	8	8	8	8	8	-	-
K-Gluconat	57	57	75	65	65	-	-
TEA-Cl	-	-	-	-	-	5	5
CsMeSO$_3$	-	-	-	-	-	62	62
MgCl$_2$	2	2	2	2	2	2	2
CaCl$_2$	0.1	0.1	0.1	0.1	0.1	0.1	0.1
HEPES	10	10	10	10	10	10	10
EGTA	-	10	1.2	-	1	10	10
BAPTA	10	-	-	-	-	-	-
Fluo-5F	-	-	-	2	1	-	0.15
ATP-Mg	2	2	2	2	2	2	2
GTP-Na$_2$	0.3	0.3	0.3	0.3	0.3	0.3	0.3
Na$_2$-Pcr	7	7	7	7	7	7	7
pH (7.7-7.8)	KOH	KOH	KOH	KOH	KOH	TEAOH	TEAOH
Osmolarity	190 - 195 mOsm						
Free Na$^+$	15	15	15	15	15	15	15
Free K$^+$	105-110	105-110	95	105	100	0	~1
Free Cl$^-$	12.2	12.2	12.2	12.2	12.2	9	9
Free Ca^{2+}	0.2-5 nM	0.1-3 nM	1-30 nM	2-70 nM	1-30 nM	0.1-3 nM	0.1-3 nM

Table 3. Intracellular solutions

All concentrations are given in mM except the free Ca^{2+}. The intracellular solutions were prepared with distilled water and stored at -20 °C. The pH of each solution was adjusted to 7.8 with 0.5 M of either potassium hydroxide (KOH) or tetraethylammonium hydroxide (TEAOH) prior to adding ATP, GTP and creatine phosphate (Pcr or Phosphocreatine). Osmolarity was measured after the adjustment of pH. The calculation of free K$^+$ was also included the K$^+$ ions of KOH (added during the adjustment of the pH). Free Ca^{2+} was calculated based on a total Ca^{2+} range of 0.1-0.5 mM, a pH range of 7.6-7.9, a temperature range of 20-24, an ionic strength range of 0.13-0.17 mol/L, and other parameters as: [ATP]+[GTP]=2.3 mM, [Mg^{2+}]=4 mM. The K$_d$ values of EGTA, BAPTA and Fluo-5F were 0.22 μM, 0.5 μM and 2.3 μM, respectively (Wu, 1996; Smith 1996).

3. Results

PART A: Ca^{2+} microdomains in olfactory receptor neurons of *Xenopus laevis*

3.1 Ca^{2+} channels in *Xenopus laevis*

To study Ca^{2+} microdomains in ORNs of *Xenopus laevis*, a Ca^{2+} indicator, Fluo-5f, was employed. The first steps were to identify the Ca^{2+} current and to verify that the Ca^{2+} indicator had no influence on the Ca^{2+}-channel function, because Fluo-5f had a fast response for Ca^{2+} binding but showed a low binding affinity as compared to EGTA which was the main Ca^{2+} buffer in the intracellular solutions.

3.1.1 Whole-cell Ca^{2+} currents

Ca^{2+} currents in ORNs of *Xenopus laevis* were recorded in the whole-cell configuration with a Cs^{+}-based internal solution, additionally, with TTX (1 μM) in the bath solution (Schild, 1989). In the voltage-clamp mode, the Ca^{2+} current activated at -40 mV and showed maximal amplitudes at -10 mV (Fig. 4A and B). These properties together with the long inactivation (>200 ms) of the currents (Fig. 4A and 9A) suggest that the predominant if not the only Ca^{2+} current in *Xenopus* ORNs is a high-voltage-activated L-type current. As a further test, a dihydropyridine blocker, nimodipine (20 μM), was applied and a marked decrease in the Ca^{2+} currents after a 5-min blocker incubation was recorded with a partial recovery after washout (Fig. 4C and D). Regarding the current rundown during the blocker incubation, a parallel control with only vehicle application (DMSO, 0.2%) was tested. Fig. 4E illustrates the statistical summary of the normalized Ca^{2+} currents at -10 mV before and after blocker or vehicle incubation. The significant inhibition of the current, which is around 60±10% (n = 5), indicates an L-type Ca^{2+} channel. Although the raw current traces in Fig. 4 were obtained without Fluo-5f, similar currents were obtained when the internal solution contained ~150 μM Fluo-5f (Fig. 9A). As a comparison, Fig. 4B shows the Ca^{2+} current/voltage (IV) curves recorded with and without Fluo-5f. No significant difference was found between these two IV curves, implying that Fluo-5f (up to

200 µM) has almost no effect on the Ca^{2+} channel function.

3.1.2 Number of Ca^{2+} channels in single neurons

After establishing the whole-cell configuration to measure the Ca^{2+} currents, the number of Ca^{2+} channels was determined using a fluctuation analysis of Ca^{2+} tail currents (for detail see section 2.7.2). The Ca^{2+} tail currents, as shown in Fig. 5A, were elicited by repolarization to -70 mV after repetitive depolarizing pulses from a holding potential of -70 mV to +50 mV. The variance-mean current plots were fitted with Eq. 8 (section 2.7.2) yielding the channel number and the single channel current for individual neurons (Fig. 5B). The average channel number was 33 ± 18 and the single channel current at -70 mV was 0.64 ± 0.21 pA (n = 39; Fig. 5C and D).

3.2 Imaging Ca^{2+} microdomains

As the above results indicate that the number of Ca^{2+} channels in single ORNs is smaller than that number in single "hotspots" of cochlear hair cells, whose number has been reported around 100 (Roberts 1990; Wu 1996; Bortolozzi *et al.*, 2008), an interesting question arises: how are the Ca^{2+} channels distributed in ORNs, uniformly or clustered? The following chapters will address this question.

3.2.1 Number of Ca^{2+} microdomains in individual focal planes

The approach here combined the patch-clamp technique and confocal microscopy with Ca^{2+} imaging. In the whole-cell configuration, Fluo-5f (150 µM) was added to the internal solution as a Ca^{2+} indicator. Single neurons were depolarized to -10 mV (Fig. 6A), where the maximal Ca^{2+} currents were induced (Fig. 4B); and fluorescence images were continuously acquired before, during and after the depolarization (Fig. 6A and B, 1 to 3). Fig. 6B illustrates the results from single optical planes of two individual neurons. The frames acquired during the depolarization (Fig. 6B, 2) clearly show some hotspots, indicating that the observed $[Ca^{2+}]$ increases were highly inhomogeneous and confined to a few high $[Ca^{2+}]$ microdomains. However, there is no clearly visible hotspot in the frames acquired before (Fig. 6B, 1) and after (Fig. 6B, 3)

the depolarization, suggesting that the observed $[Ca^{2+}]$ increases are voltage-dependent and probably the voltage-gated Ca^{2+} channels are located there.

The number of the microdomains was quantified in images averaged during the depolarization and then subtracting the control images averaged just prior to the depolarization (Fig. 6B, "2-1"). In order to activate as many Ca^{2+} channels and take as many frames as possible, a long depolarizing pulse (200 ms) was applied with 5 to 10-times repetition in 3-s intervals. However, due to the rundown of Ca^{2+} signals, usually, only one focal plane could be reliably acquired. Fig. 6C shows the distribution of these numbers over 40 focal planes originating from 40 neurons. On average, there are 1.5 microdomains per optical plane with a standard deviation of 1.9 (Fig. 6C).

Given that the thickness or diameter of a neuron in the z-direction (the axial direction) is about 5 to 10 μm and one focal plane covers a thickness of ~1.5 μm, a single neuron may present 4–7 focal planes without overlapping. Thus, a crude estimate would be around 5–12 Ca^{2+} microdomains per neuron.

3.2.2 Number of Ca^{2+} microdomains in individual neurons

Another attempt is to acquire multiple focal planes covering as much as possible the entire neuron to provide more accurate estimates. Since the Ca^{2+} rundown is use-dependent, the smaller the Ca^{2+} influx is, the less the rundown will be. Thus, in the following experiment, a 10-ms depolarizing pulse was used and repeated 20–30 times in 3-s intervals. It was found that with this protocol the image quality reduced slightly, but usually up to 9 focal planes could be obtained. As shown in Fig. 2B, most neurons have a thickness of 5–10 μm in the short axis (in the z-direction). Assuming a thickness of ~1.5 μm in one focal plane, 6 to 7 planes with 1 to 1.5-μm intervals can already cover the entire neuron in the z-direction. Fig. 7A and 7B illustrate the results from two neurons. For each neuron, six contiguous focal planes (labeled as 1–6) in 1-μm intervals are shown. From all images taken during (labeled as a) and after depolarization (labeled as b), the control background images taken just prior to the

depolarization have been subtracted. The hotspots again show voltage-dependent and they can be clearly observed only in the images taken during the depolarization (Fig. 7A and B, 1a–6a) but not after (1b–6b). Additionally, as indicated in Fig. 6, there are indeed some focal planes without hotspots like in Fig. 7B, 1a. The summary statistics over 28 neurons are shown in Fig. 7C. On average, the number of Ca^{2+} microdomains per neuron is 6.3 ± 2.3.

3.3 Number of Ca^{2+}-channels in Ca^{2+} microdomains

Since the number of Ca^{2+} microdomains in signal ORNs (Fig. 6 and 7) is much less than that of Ca^{2+} channels (Fig. 5), no matter how the distribution is, some Ca^{2+} microdomains must have multiple channels like channel clusters. If all channels are equally spread, one could estimate an average value of 5-6 channels per microdomain. The further step is to clarify by a direct determination of the Ca^{2+}-channel number in Ca^{2+} microdomains.

The approach is based on a variance analysis (for detail see section 2.7.2 and 2.7.3), a method similar to a previous report (Sabatini and Svoboda, 2000), which requires two estimates: 1) the coefficient of variation of fluorescence signal in the Ca^{2+} microdomains; and 2) the open probability of Ca^{2+} channels at the specific membrane potential when the depolarizing voltage are being applied to activate the channels during Ca^{2+} imaging.

3.3.1 Coefficient of variation of fluorescence signal

The Ca^{2+} images were evaluated by using the same control background image subtraction as in Fig. 6, and the correlation maps were calculated to facilitate the selection for ROIs (section 2.8.1). As shown in Fig. 8A and B, the Ca^{2+} microdomains are clearly visible in both, the control background subtracted image (A), and the image at time-lag zero of the correlation function (B). An image mask for the Ca^{2+} microdomains (Fig. 8C) was taken from the correlation maps. Fig. 8D shows the fluorescence signal of two ROIs (1 and 2) and the background during three trials.

Following the depolarizing test-pulses, the fluorescence of two Ca^{2+} microdomains (Fig. 8D 1, blue, and 2, green) rose and declined very quickly, showing almost exactly the shape of the test-pulses (Fig. 8D top).

Trial-to-trial fluctuations were analyzed for further extracting the Ca^{2+} channel number in individual Ca^{2+} microdomains. Dark noise (before shutter opening) and background fluorescence (pixels in the same frames outside of the target neuron) were measured during each experiment (Fig. 8E, black filled rhomboid and red circle). Baseline fluorescence (before depolarization) and response fluorescence (during depolarization) were obtained in each trial (Fig. 8D). Fig. 8E also illustrates the variance plotted against mean for the fluorescence before (circle) and during (triangle) depolarization from two ROIs (1, blue; 2, green), and from the background (red). The fluctuations of the baseline fluorescence within the individual trials and their variances were used to estimate the threshold for data selection. Neurons, whose baseline fluctuations were no greater than the expected noise (photon shot noise plus dark noise), were selected for further analysis. However, neurons, whose analyzed variation increases (the response fluorescence fluctuations) were smaller than the variance of baseline fluctuations, would again be neglected. The coefficient of variation of fluorescence ($CV_{F,\Delta[Ca]}$) is shown in Fig. 10A, and is required for further calculations.

3.3.2 Open probability of Ca^{2+} channels

Both the single channel current and the open probability are functions of a membrane potential. Besides, the open probability is also a function of time. However, as shown in Fig. 9A and 9B, except the first 20 ms after the depolarization, the Ca^{2+} current reveals constant means with similar standard errors (Fig. 9B) over the whole trace, indicating that after the depolarization for 20 ms the Ca^{2+} channels are likely running in a mode with single channel current and open probability being constant and not being a function of time. Moreover, the average current, $\langle I \rangle$, taken over 180 ms at -10 mV and its variance, $Var(I)$, could be fitted by a linear relationship, $Var(I) = \langle I \rangle k + \sigma_0$, where k, the slope, equals the product of the single channel current (at -10mV) and the

probability for the channel to be closed, $k = i(1 - P_o)$ (see section 2.7.2, Eq. 9 and 10). Fig. 9C shows the current variance-mean plot from 32 neurons. The linear regression gave a slope of $k = -0.046 \pm 0.003$. The linear dependence implies that k is constant, which also suggests that the open probability P_o and the single channel current i are constant too.

Since P_o and i are constant for a certain membrane potential, if assuming $P_{o,+50} = 1$ at +50 mV, the open probability at -10 mV could then be obtained by the ratio of the tail currents when stepping back either from -10 mV ($I_{tail,-10}$) or from +50 mV ($I_{tail,+50}$) to -70 mV:

$$\frac{I_{tail,-10}}{I_{tail,+50}} = \frac{P_{o,-10}\,Ni}{P_{o,+50}\,Ni} = P_{o,-10}$$

where N is the total channel number. The amplitudes were determined by fitting exponential decay curves to the tail currents recorded from the same cells as shown in Fig. 9D. In 8 cells recorded in this way, $P_{o,-10}$ resulted as 0.77 ± 0.05. The assumption, $P_{o,+50} = 1$ at +50 mV, appears justified here as stepping back from +30, +50, or +60 mV led to virtually the same tail current amplitudes (Fig. 9E).

3.3.3 Number of Ca^{2+}-channels per Ca^{2+} microdomain

If a Ca^{2+} microdomain has N channels that open independently with probability p during depolarization, the number of open channels will be governed by the binomial distribution. The coefficient of variation is given by: $CV_{open} = \frac{\sigma_{open}}{\langle N_{open} \rangle} = \frac{\sqrt{Np(1-p)}}{Np} = \sqrt{\frac{(1-p)}{Np}}$ (Eq.13, section 2.7.3). Assuming linearity between the fluctuations of Ca^{2+} influx through the channels, $\Delta[Ca^{2+}]$, and the resulting fluorescence, $\Delta\langle F \rangle$, the corresponding coefficients of variations, $CV_{\Delta[Ca]}$ and CV_F , respectively, are equal and given by: $CV^2_{\Delta[Ca]} = CV^2_{F,\Delta[Ca]} = \frac{(1-p)}{Np}$ (Eq. 14, section 2.7.3). With the given P_o = 0.77 ± 0.05, at -10 mV, the number of Ca^{2+} channels per microdomain will be: $N = \frac{1}{CV^2_{F,\Delta[Ca]}}\left(\frac{1}{P_o} - 1\right) = \frac{0.23}{CV^2_{F,\Delta[Ca]}}$. Fig. 10B shows the distribution of the number over 17 Ca^{2+} microdomains. The mean value is 12 ± 5 Ca^{2+}-channels per microdomain.

PART B: Co-localization of Ca²⁺ microdomains and BK channels in olfactory receptor neurons of *Xenopus laevis*

3.4 Location of BK channels

By using Ca^{2+} indicators, the location of Ca^{2+} microdomains can be clearly identified in individual ORNs of *Xenopus laevis*. Unfortunately, no such a specific indicator with high selectivity for K^+ was available. Using antibody to recognize BK channels is a classical way which works well for most of the species, but unluckily, all commercial available antibodies for either BK α- or β-subunits do not share 100% identity of their recognition epitopes with the sequence of BK channels in *Xenopus laevis*. So an alternative approach must be found.

3.4.1 Labeling Iberiotoxin and quantifying number of fluorophores

Instead of using specific antibodies, the idea is to use fluorophore-labeled specific agonists or antagonists of the targets. Here, a BK channel specific antagonist, IbTx, was used and labeled with Alexa Fluor dyes by ourselves (for detail see section 2.5.1). A diagram in Fig. 11 illustrates the amino acid sequence of IbTx and five candidate residues for labeling. The numerical quantity of fluorophores per IbTx, measured by imaging with photobleaching (for detail see section 2.5.1), is shown in Fig. 12.

Fig. 12A illustrates the fluorescent spots formed by Alexa Fluor dyes which were spin coated onto cover slips as a control for single molecule investigations. The fluorescent signal with multistep bleaching behavior arising from chance proximity was picked, and the last several bleaching steps were analyzed (Fig. 12B). A unitary intensity indicating the minimal single step could be obtained during photobleaching. Accordingly, the fluorescent signal of individual dye spots, if normalized with such unitary intensity, would result in the number of steps per spot, which would also imply the number of molecules per spot since a single-molecule spot could only give a single step. Fig. 12E shows the distribution of such steps among 270 dye spots. The presence

of a peak around 1 indicates that with the applied conditions for preparation, most dye spots are single molecules.

With the same preparation, the number of Alexa fluorophores per labeled IbTx was examined. Fig. 12C and D illustrates an image of labeled IbTx spin coated onto a cover slip (Fig. 12C) and the corresponding fluorescence trace during photobleaching (Fig. 12D). The number of steps per spot is shown in Fig. 12F. Among 360 spots, most were found having 3 to 4 steps. Suppose that with the same preparation most spots should have single molecules, therefore, the result could be that most IbTx were labeled with 3 to 4 fluorophores. On the other hand, the maximal steps are around 7 on the distribution chart (Fig. 12F); if little amount of spots are composed of two IbTx, the value 7 also well fits the result that each of them is labeled with either 3 or 4 Alexa fluorophores.

3.4.2 Staining BK channels with labeled Iberiotoxin

Alexa-labeled IbTx was first checked in fixed slices, and Alexa alone was used as a control. The best staining was obtained in the preparations with 1 μM labeled IbTx for 10 min, so the same conditions were also used for controls. As shown in Fig. 13A and B, the slices treated with labeled IbTx presented the specific staining as puncta around the cell bodies, indicating the surface locations of the targets. On the contrary, non-specific staining showed a uniform dispersion of the dyes on most cells in the slices treated with Alexa alone (Fig. 13C and D). These results suggest that the BK channels in *Xenopus laevis* can be stained by the labeled IbTx.

Fig. 13E also shows a time trace acquired from a single spot of the stained BK channels during photobleaching. As compared to a single spot of labeled IbTx itself, the spot of BK channels exhibits a 20–50 times stronger fluorescence. Because a background fluorescence with about 100–200 counts could always be detected in the slice samples (Fig. 13E), it was difficult to find out a minimal unitary step through photobleaching. So, it was failed to estimate the number of IbTx molecules or BK channels per spot correctly, even given the fact that the binding of IbTx to BK channel is in a one-to-one

ratio (Yu *et al.*, 2005).

Labeled IbTx in living slices were also checked with the same setup and conditions for Ca^{2+} imaging, which was a preparatory step for co-localization studies. As shown in Fig. 14, similar puncta, which surround the cell bodies indicating the surface staining of BK channels, can be seen only in the slices treated with labeled IbTx (Fig. 14A to F) but not in controls (Fig. 14G to I) stained with Alexa dye alone.

3.5 Co-localization of BK channels and Ca^{2+} microdomains

With labeled IbTx, locations of BK channels could be identified in living slices. Since BK channels had a close link to Ca^{2+}, the next step was to study if BK channels also locate close to Ca^{2+} channels. This experiment combined the Ca^{2+} imaging and BK channel staining (for detail see section 2.4.1 and 2.5.2).

Short-time incubation of olfactory mucosa slices with labeled IbTx again exhibited a pattern of puncta which typically localized on cell bodies (Fig. 15A) and disappeared after 15–30 min washout (Fig. 15B). Whenever a cell that showed IbTx puncta was patch-clamped, with Fluo-5F diffusing from the pipette into the soma, and depolarized to -10 mV to image its Ca^{2+} microdomains (Fig. 15C), there was an unambiguous superposition of Ca^{2+} channel microdomains and Alexa-IbTx-stained puncta as shown in Fig. 15D, clearly indicating a co-localization of Ca^{2+} and BK channels (n = 5 slices).

PART C: Physiological functions of BK channels in olfactory receptor neurons of *Xenopus laevis*

3.6 Functions of BK channels in olfactory receptor neurons

BK channels are well known for having a large single-channel K^+ conductance (~250 pS; Vergara *et al.*, 1998). Usually, if K^+ conductances were blocked, the cell excitability would increase; and as a direct result in neurons, the firing rate would also increase. Blocking BK channels in spontaneously firing Purkinje neurons revealed such a behavior (Edgerton and Reinhart, 2003; Womack and Khodakhah, 2004). However, so far the BK channel in ORNs of *Xenopus laevis* is not totally understood.

3.6.1 BK channel currents

Whole-cell BK channel currents in ORNs were determined by the antagonist, IbTx. As shown in Fig. 16A, incubation of 500 nM IbTx eliminated the outward currents clearly and the effect was partially reversible after washout. The BK channel currents were obtained by subtracting the currents after IbTx incubation from the total currents, and the average IV curve is shown in Fig. 16B. Assuming the conductance of a BK channel is 200–300 pS, the single channel current at +20 mV can be assumed to be on the order of 20–25 pA, which would, given the total current of 720±90 pA at +20 mV (Fig 16B), yield a rough estimate of about 30–40 BK channels per ORN.

3.6.2 Blocking BK channels reduces the response of ORNs to odorants

Generally, only a single allele of an odorant receptor gene is expressed in each ORN (Chess 1994), which means single ORN may only respond to very few odorants. To increase the experiment chances, a mixture of amino acids was applied to the slices as a group of odorants whenever stimulations were needed.

In on-cell recording, spontaneous discharges, a basal activity of an ORN, could be recorded (Fig. 17A, Control). Although such basal activity may have a range from 0.1 to 20 Hz, more than 80% ORNs still concentrate in a rate of 1 to 8 Hz as indicated by a

previous work in our lab (Manzini *et al.*, 2002). Thus, these neurons were chosen for further experiments. The basal firing rate in the experiment was 3.3 ± 0.6 Hz (Fig. 17B, Control) and was not significantly affected by applying the BK channel antagonist, IbTx (Fig. 17A and 17B, IbTx). By contrast, the firing rate of a stimulus response, whose increase can reach up to 400% (Fig. 17C, AA), was drastically reduced after IbTx incubation and its increase was only ~260% (Fig. 17C, IbTx+AA). Besides, the original stimulus response (Fig. 17A, AA) could be recovered during washout, though not completely, presumably due to incomplete washout of IbTx.

3.6.3 Changes in whole-cell recording

To further examine the influence on the APs after blocking BK channels, and to study the possible mechanisms, whole-cell current-clamp recordings were performed. An additional BK channel antagonist, ChTx, was also tested to ensure that the previous effects of IbTx were caused by blocking BK channels, and were not due to some unknown effect of IbTx peptide itself.

As shown in Fig. 18A, applying the amino acid mixture to an ORN immediately produced a high-frequency spike train, indicating the stimulus response to odorants. However, after ChTx incubation, such response became weaker and showed a spike train with a significantly lower frequency (Fig. 18B) as compared to that spike train before incubation (Fig. 18A), which confirms that blocking BK channels reduces the neuronal response to odorants. Besides, phase plot analysis suggests that after blocking BK channels the initiation site of APs becomes more negative and the falling phase becomes slower (Fig. 18C, middle panel).

A more complicated phenomenon with BK channels blocked as shown in Fig. 19 was that not all neurons revealed changes in action potential initiation site, for example, the neuron in Fig. 19B. However, neurons that have presented changes in their initiation site (Fig. 19A, middle panel), likely showed only a parallel shift with no slope change in the phase plot, suggesting a hyperpolarization of membrane potential generated in

these neurons with BK channels blocked. Nevertheless, all neurons, after BK channels was blocked, showed a significant change in the falling phase of APs (Fig. 19A and B, right panels). This indicates a broadening AP with a slower falling edge, which suggests that the function of BK channels may relate to the repolarization of APs.

3.6.4 Blocking BK channels slows the falling phase of action potentials

The repolarization phase of individual APs was further analyzed quantitatively. Fig. 20A illustrates the responses of two ORNs recorded under whole-cell current-clamp conditions. It has been noticeable that before antagonist treatment, their spontaneous firing rates or basal activities were already different (Fig. 20A, pre-incubation). In fact, in Fig. 20A, Cell #1 shows the lowest and Cell #2 shows the highest basal activities in all records. Nevertheless, the shapes of their APs are similar and all the falling phases of the APs can be perfectly fitted with single-exponential decay curves yielding time constants of around 2.5 ms (Fig. 20B), implying that no matter how high or low the basal activities of the ORNs are, the APs in such basal states are nearly identical (Fig. 20B) and have no correlation to the firing rates. In contrast, blocking BK channels by IbTx or ChTx slowed down the falling phase of APs significantly, which resulted in a longer decay of about 5 ms for IbTx and 6 ms for ChTx (Fig. 20A and C). These results further confirm that BK channels in ORNs relate to the repolarization of APs.

3.6.5 Effect of BK channels on interspike intervals during stimulations

One advantage to do whole-cell current-clamp in ORNs is to inject current to induce APs mimicking the stimuli. Fig. 21 illustrates the APs induced by 2-ms pulses of depolarizing current injections. After blocking BK channels, the falling phase of APs showed a longer decay time as compared to that before incubation, which was similar to the results of spontaneous APs (Fig. 20). Moreover, when a longer current pulse was injected, a spike train could be elicited as shown in Fig. 22. However, after blocking BK channels (Fig. 22, red) a current step with the same intensity was unable to achieve the same firing frequency. Summary plots in Fig. 22B and C show that after IbTx incubation, the 1st ISI increased about 6% as compared to control, and significant

increases can be observed in the 2nd and the subsequent ISIs. Such enlargement in ISIs suggests that a neuron in response to the same stimulus intensity cannot fire as fast as before without functional BK channels.

3.6.6 Buffering Ca^{2+} mimics the effect of BK channel antagonist

As functions of BK channels were closely related to intracellular $[Ca^{2+}]$, the further study used the intracellular solutions with different Ca^{2+} chelators; in combination, the BK channel antagonist was applied. Fig. 23 illustrates the effects of different Ca^{2+} chelators on the induced APs. Fig. 24 shows the summary statistics for the comparisons of recordings under different intracellular solutions before and after blocking BK channels. When the intracellular solution contained 10 mM EGTA, as compared to 1.2 mM EGTA, the decay time was prolonged from ~2.5 ms to ~4 ms. A further prolongation after ChTx incubation could be observed, which was ~5.3 ms and similar to the value when 1.2 mM EGTA was used. However, when the intracellular solution contained Ca^{2+} chelators with fast binding kinetics, like BAPTA or Fluo-5f, the decay time already showed a long value of ~7 ms even before ChTx incubation and no further extension could be detected after ChTx incubation. A more accurate condition was tested with half of the Fluo-5f replaced by EGTA; the decay time was prolonged from ~2.5 to ~5.5 ms after BK channel antagonist incubation, which was similar to the change when 1.2 mM EGTA was used. These results show that buffering Ca^{2+} with fast chelators were fully able to mimic the effect of the BK channel antagonist and influence the falling phase of APs as well.

3.7 Distance between Ca^{2+} channels and BK channels

With different Ca^{2+} chelators, the distance between Ca^{2+} channels and BK channels can also be roughly estimated. Assume that in the whole-cell configuration a well chemical "clamp" has been established, whereby the concentration of endogenous mobile Ca^{2+} buffers will be very low and the main Ca^{2+} buffers will be the Ca^{2+} chelators in the intracellular solutions. Hence, the $[Ca^{2+}]$ can be calculated with a steady-state equation

(Neher, 1986; Smith, 1996): $[Ca^{2+}]_r = [Ca^{2+}]_\infty + \frac{i_{Total}}{4\pi F D_{Ca} r} e^{-\frac{r}{\lambda}}$ (for detail, see section

2.6). Based on Fig. 5D and Fig. 9, a high boundary with the single-channel current, i=0.7 pA, and the open probability, P_o=0.9, and a low boundary with i=0.17 pA, and P_o=0.7, are further assumed to estimate the maximal and minimal distances. Fig. 25 illustrates the Ca^{2+} profiles with one channel or a 10-channel cluster in the center, when intracellular solutions contain 10 mM BAPTA or 1.2 mM EGTA. The distance between a BK and Ca^{2+} channel can be determined, given $[Ca^{2+}]$ larger than 10 µM for a normal BK channel activation (Brenner *et al.*, 2000). Table 4 lists the distances under different conditions when $[Ca^{2+}]$ drops to 10 µM. Since 10 mM BAPTA could mimic the effect of BK channel antagonist but 1.2 mM EGTA could not, and 10 mM EGTA was likely in a middle state showing partial influence; thus, the estimated distance was around 50 nm for only one Ca^{2+} channel in the center, or about 200 nm for 10–15 Ca^{2+} channels arranged closely as a cluster in the center. In case these Ca^{2+} channels were not closely located or the number was much less than 10, the shortest distance from the BK channel to these Ca^{2+} channels would have to be smaller than 200 nm, otherwise the whole contribution of all Ca^{2+} channels would be too small to activate the BK channel.

Ca^{2+} chelator	Distance (nm; $[Ca^{2+}]$ = 10 µM)		
	1 Channel	10 Channels	15 Channels
BAPTA 10 mM	15	30	35
EGTA 10 mM	50	180	220
EGTA 1.2 mM	65	300	390

Table 4. Distance from channel center to a position when $[Ca^{2+}]$ drops to 10 µM
The distances were the middle values estimated from the assumed low and high bondaries under each listed conditons using Eq.1. All parameters were taken from Fig. 25.

On the other hand, the distances between two channels are unlikely less than 30 nm, the shortest distance that 10 mM BAPTA can exert its function, since average Ca^{2+} channel number per Ca^{2+} microdomain is about 12 (Fig. 10B). So, a reliable estimate for the distances between these two channels is around 50 to 200 nm.
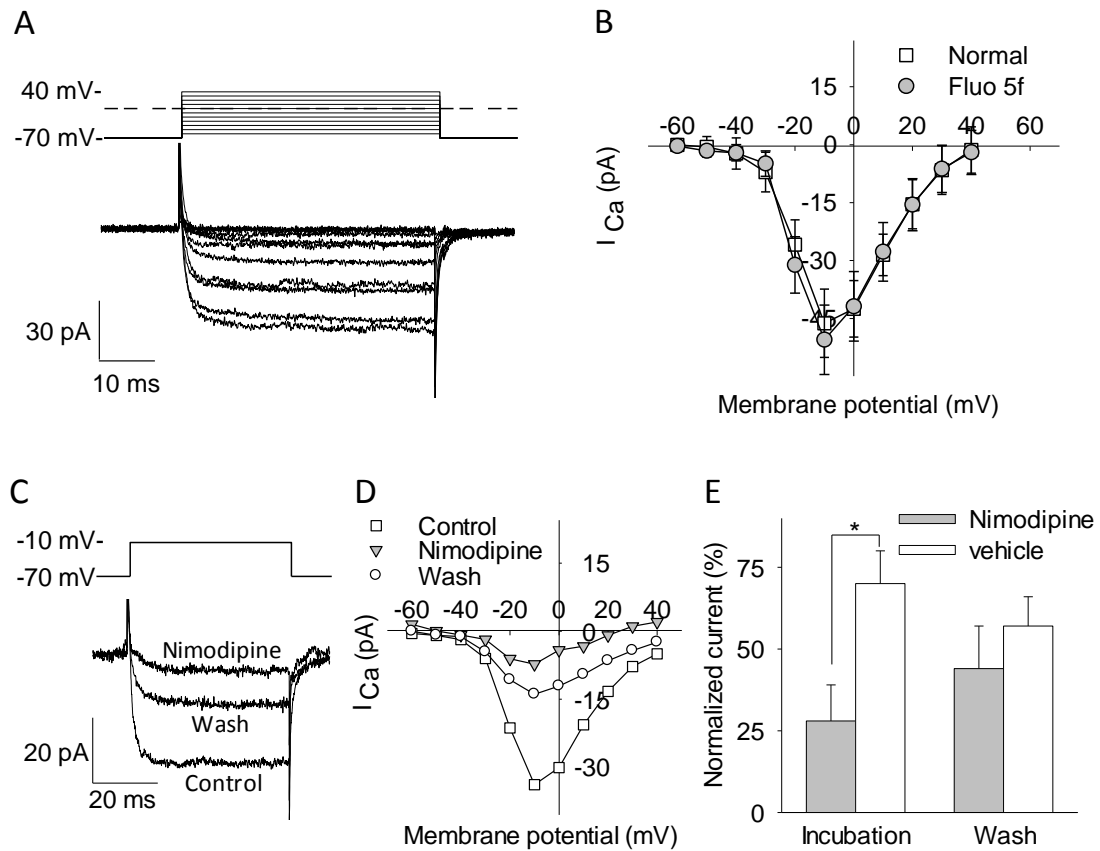
Figure 4. Whole-cell Ca^{2+} currents and IV curves in ORNs of *Xenopus laevis*.
(A) Macroscopic Ca^{2+} current (bottom) induced by successively depolarized pulses in 10-mV steps from -60 to 40 mV for 50 ms (top). (B) Ca^{2+} current/voltage (IV) curves recorded with normal (square, n=6) and Fluo-5f (circle, n=5) internal solutions. (C) Ca^{2+} current before (Control), 5 min after nimodipine (20 µM) application (Nimodipine) and 5 min after washout (Wash). Nimodipine was dissolved in DMSO and then diluted in bath solution (Final DMSO is ~0.1%, v/v). (D) Ca^{2+} IV curves in the same neuron and conditions as in C. (E) Summary statistics for the effect of nimodipine on the Ca^{2+} current at a depolarizing voltage of -10 mV. Data from individual neurons were 5 min after incubation (Incubation) of either 20 µM nimodipine (Nimodipine) or 0.2% of DMSO (vehicle), followed by 5 min washout (Wash). All the responses were normalized to the current recorded ~3 min after establishing the whole-cell configuration. * p<0.05, Student's *t* test, n=5.

A

B

$$\text{Fit}:\text{Var}(I) = -\frac{\langle I\rangle^2}{N} + i\langle I\rangle + \sigma_0$$

$N = 68 \pm 3$

$i = 0.66 \pm 0.02$ pA

C

$\langle N\rangle = 33 \pm 18$

D

$\langle i\rangle = 0.64 \pm 0.21$ pA
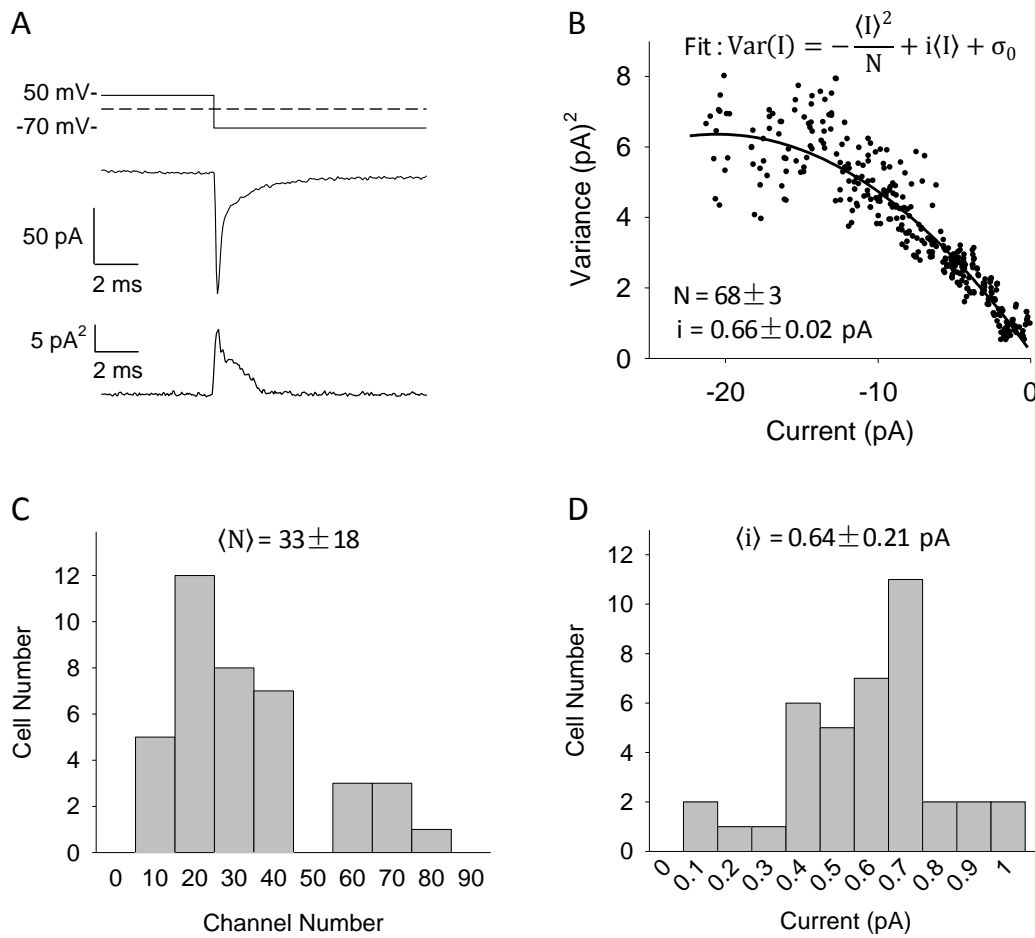
Figure 5. Estimation of Ca^{2+}-channel number and single channel current

(A) Waveforms from top to bottom: voltage test-pulse (top), Ca^{2+} tail current (middle) and the current variance (bottom). (B) An example plot of variance versus current mean (dot) and the curve fitting (solid line). Superimposed: the fitting function and the results with fitting errors; N, number of channels; i, single channel current. (C, D) Distribution of N (C) and i (D) over 39 cells. Superimposed: $\langle N\rangle$ and $\langle i\rangle$, the average of all N and i values, and the standard deviation.

A

B

C
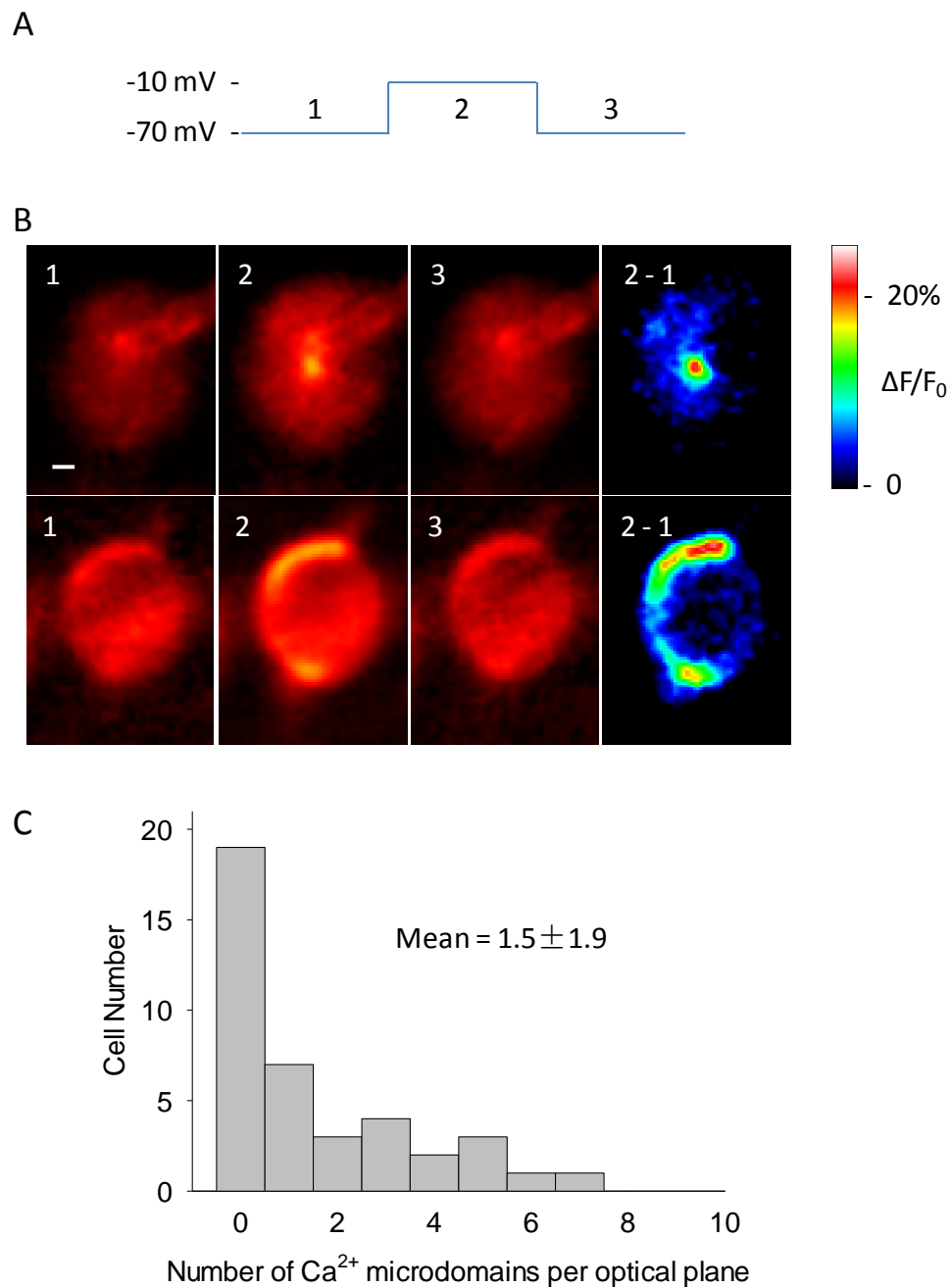
Figure 6. Ca^{2+} microdomains in single confocal optical planes

Neurons were depolarized to -10 mV, and meanwhile fluorescent signals were collected. (A) Voltage test-pulse waveform, the time of depolarization is 200 ms. (B) Average images taken before (1) during (2) and after (3) depolarization, and the subtraction of images 1 from 2 (2-1). Scale, 1 μm. (C) Distribution over 40 cells. The average and the standard deviation are shown.

A

B

C
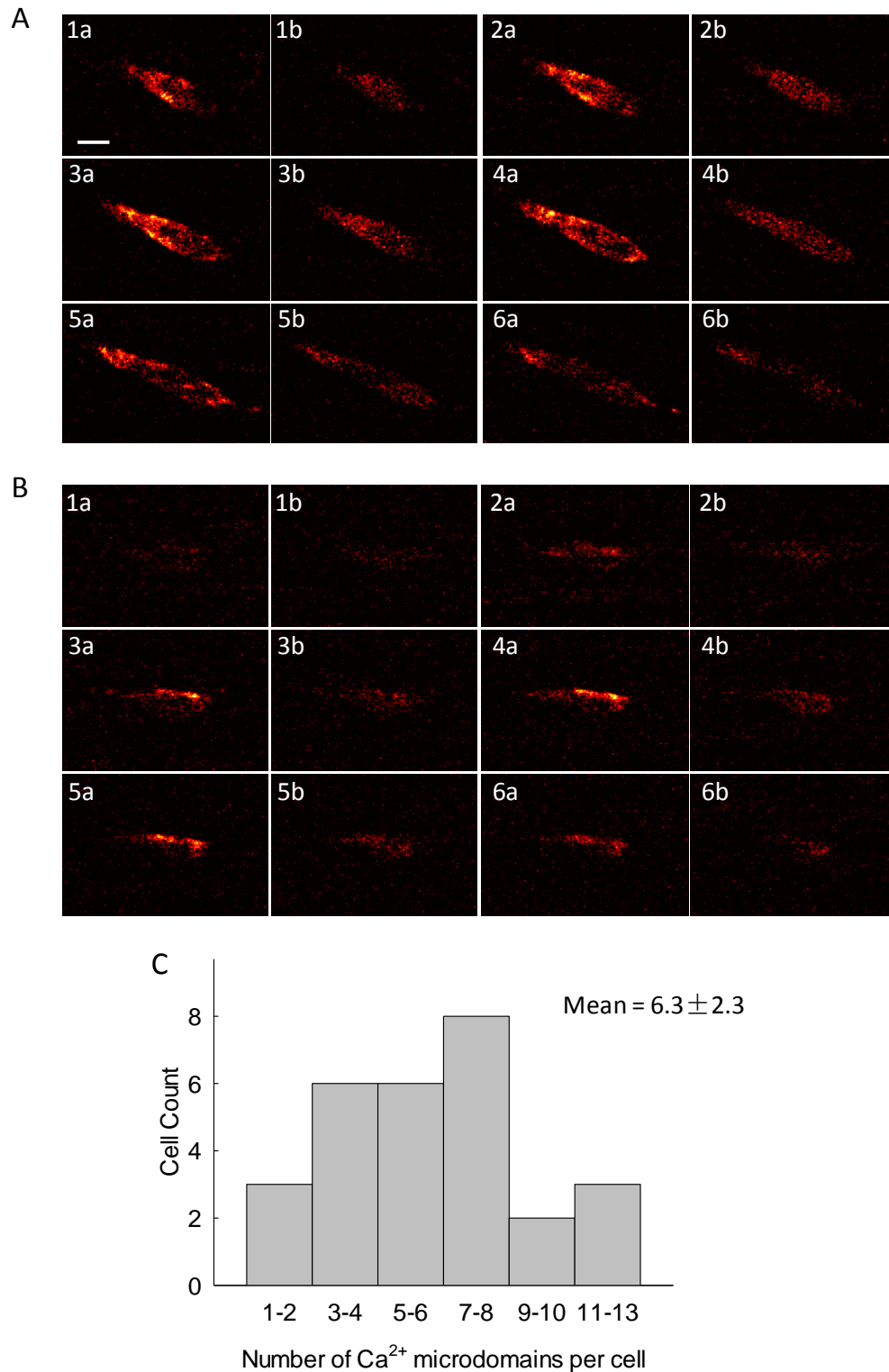
Figure 7. Ca^{2+} microdomains in single neurons

Neurons were depolarized for 10 ms to -10 mV. (A) Six focal planes in an interval of 1 μm were labeled as 1 to 6. From images during (a) and after (b) depolarization, the control background images just prior to the depolarization have been subtracted. Scale, 5 μm. (B) Example with less number of Ca^{2+} microdomains. (C) Distribution over 28 cells. The average and the standard deviation are shown.
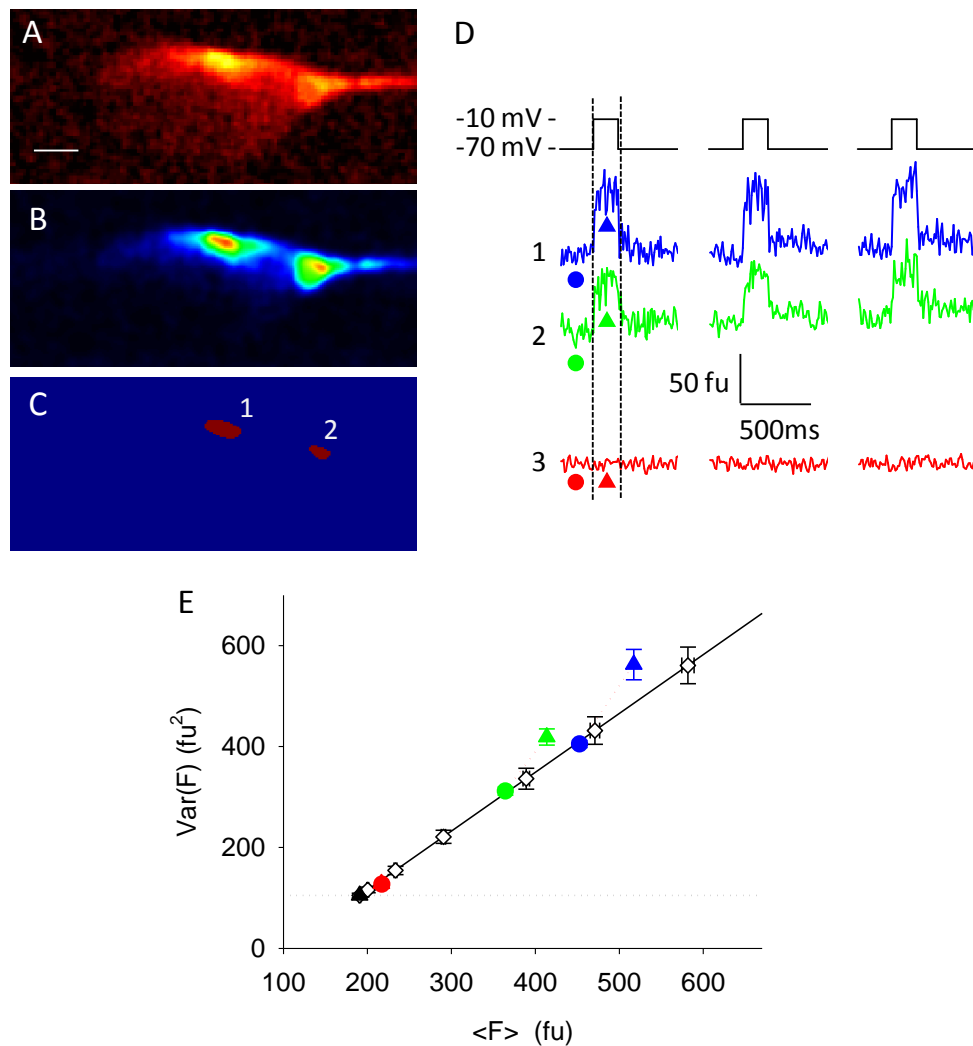
Figure 8. Coefficient of variation of fluorescence in Ca²⁺ microdomains

(A) Average fluorescence image taken during depolarization subtracted by the images taken just prior to the depolarization. Scale, 2 μm. (B) Correlation map in time-lag of 0. (C) Image mask obtained from B. Two ROIs were marked as 1 and 2. (D) Raw fluorescent signals of ROI 1 (blue) and 2 (green), and of background (3, red) taken from the pixels outside of the neuron. Symbols indicate the data taken before (circle) or during (triangle) the depolarizing voltage test-pulses (top, black trace). (E) Variance plotted against mean for the data before (circle) and during (triangle) depolarization (same symbols as indicated in D) from ROI 1 (blue), 2 (green) and the background (red). Rhomboids, variance/mean relationship obtained by imaging the patch pipette while varying the illumination intensity. Horizontal dotted line, variance due to dark noise; solid line, variance expected from photon shot noise. fu, fluorescence unit.
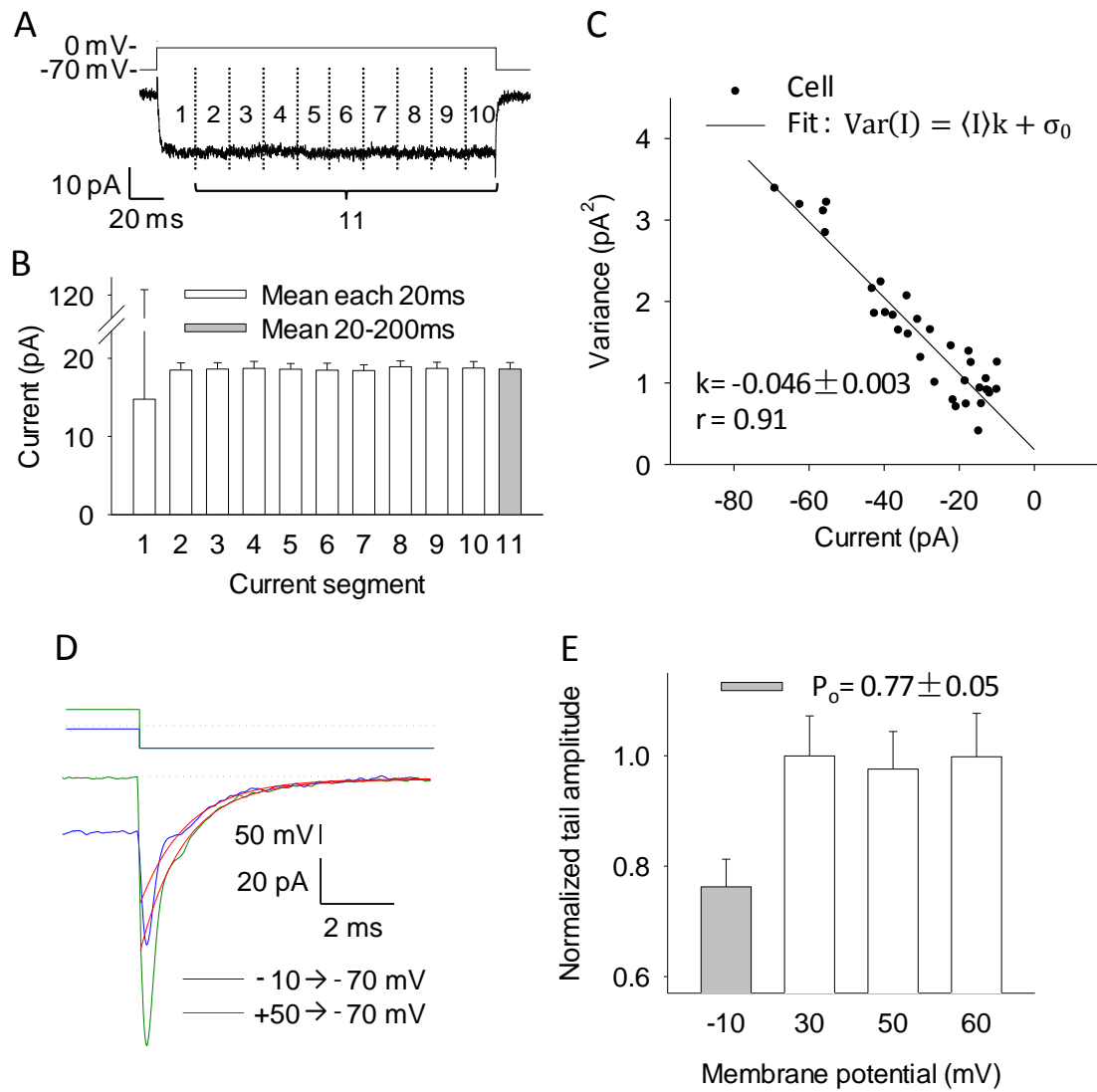
Figure 9. Ca²⁺ channel open probability

Whole-cell Ca^{2+} currents were obtained with the Fluo-5f internal solutions. (A) Macroscopic Ca^{2+} current (bottom) induced by depolarization to -10 mV for 200 ms (top). Ten current segments in 20-ms intervals are marked as 1-10; the segment 11 is the current during 20-200 ms of the depolarization. (B) Current mean of each segment with standard error. (C) Variance plotted against the current mean during 20-200 ms of the depolarization (segment 11) over 32 cells. Superimposed: k, the slope of linear regression, and r, the correlation coefficient. (D) Ca^{2+} tail currents (bottom) induced by repolarization to -70 mV (top) after the depolarization to +50 mV (green) and -10 mV (blue), and fitted with single exponential decay curves (red). (E) Summary statistics for the normalized tail amplitudes over 8 cells. Superimposed: P_o, the open probability at -10 mV calculated by (section 3.3.2): $P_o = \frac{I_{tail,-10}}{I_{tail,+50}}$.
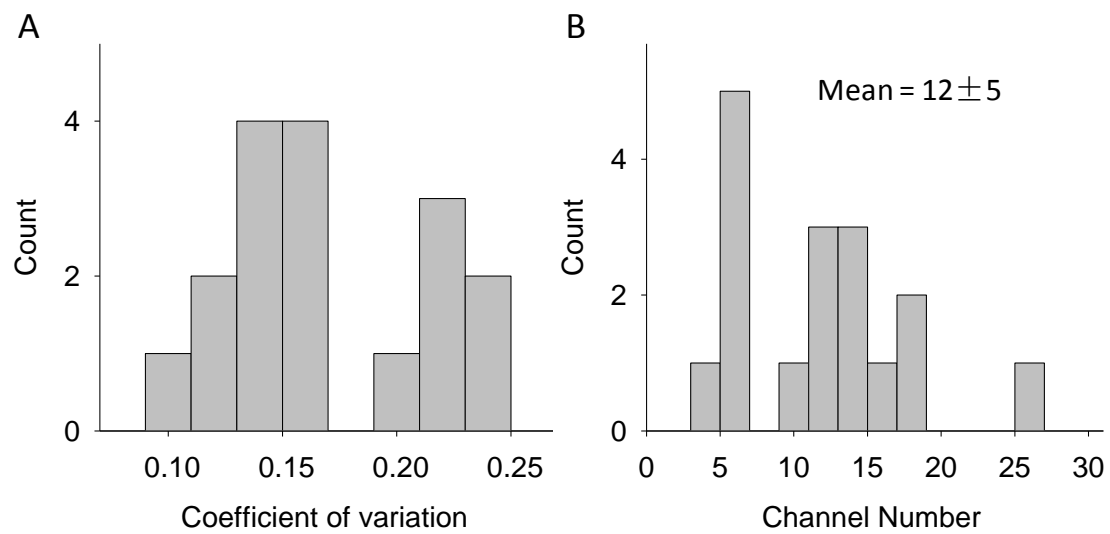
Figure 10. Distribution of Ca²⁺ channel number per microdomain

(A) Distribution of coefficient of variation. (B) Distribution of Ca^{2+} channel number per microdomain. The average and the standard deviation over 17 Ca^{2+} microdomains are shown.
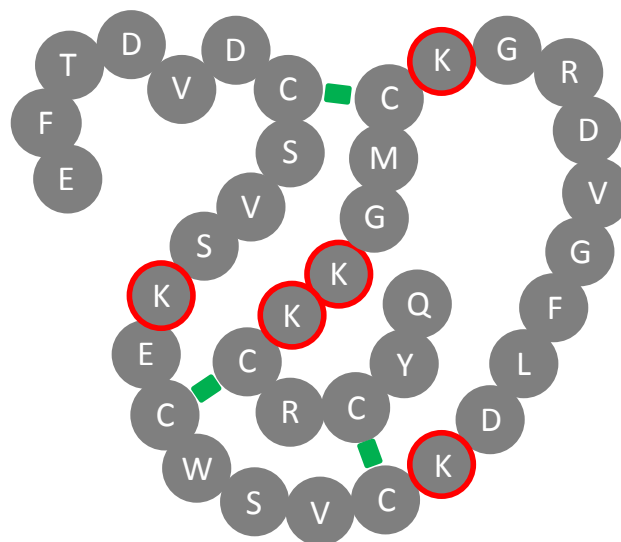
Figure 11. Five possible positions for labeling of Alexa dye in Iberiotoxin

(A) Amino acid sequence diagram of Iberiotoxin and 5 possible residues (red circles) for labeling.
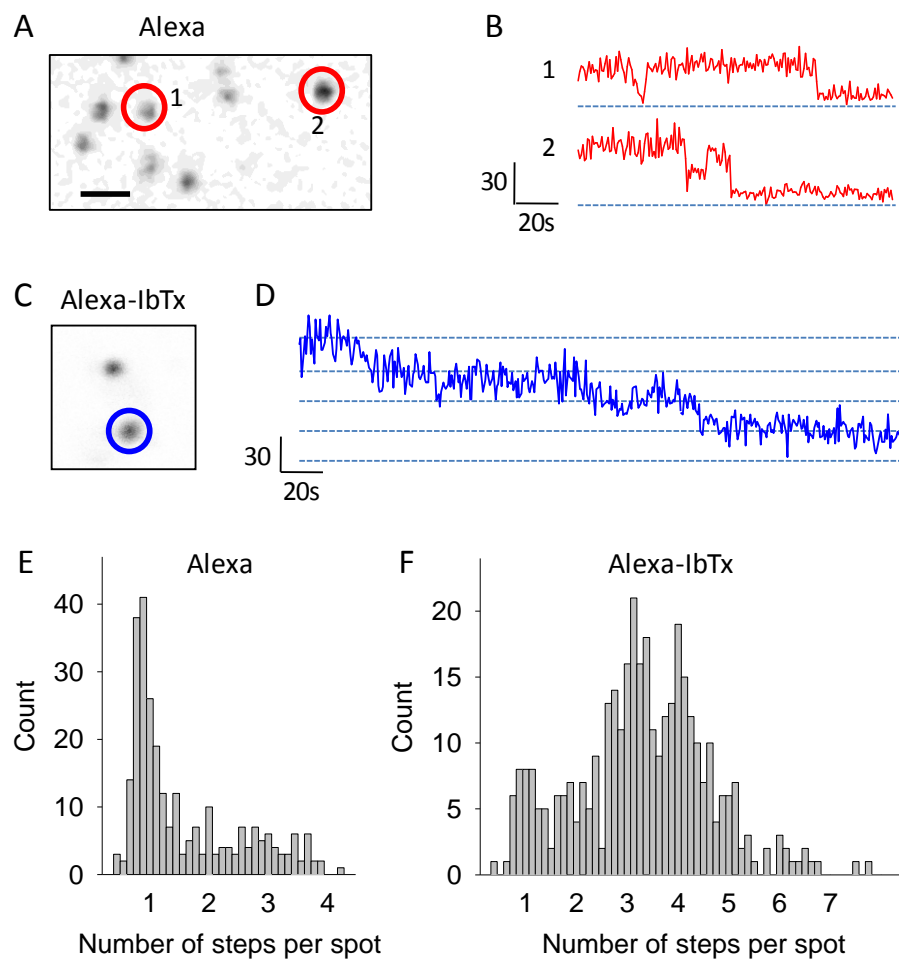
Figure 12. Quantifying number of fluorophores per Iberiotoxin

(A) Image of Alexa dyes spin coated on to a cover slip. Two ROIs (red circle) are labeled as 1 and 2. Scale, 0.5 μm. (B) Fluorescent signals of ROI 1 and 2 in A. Vertical scale is photon count, dashed line is 0. (C) Spots of Alexa labeled IbTx (Alexa-IbTx). One ROI was marked by a blue circle. (D) Fluorescent signal of ROI in C. Dashed lines start from 0 in an interval of the unitary fluorescent signal detected in B. (E) Estimated steps of individual spots of Alexa dye. (F) Estimated steps of individual spots of Alexa labeled IbTx.
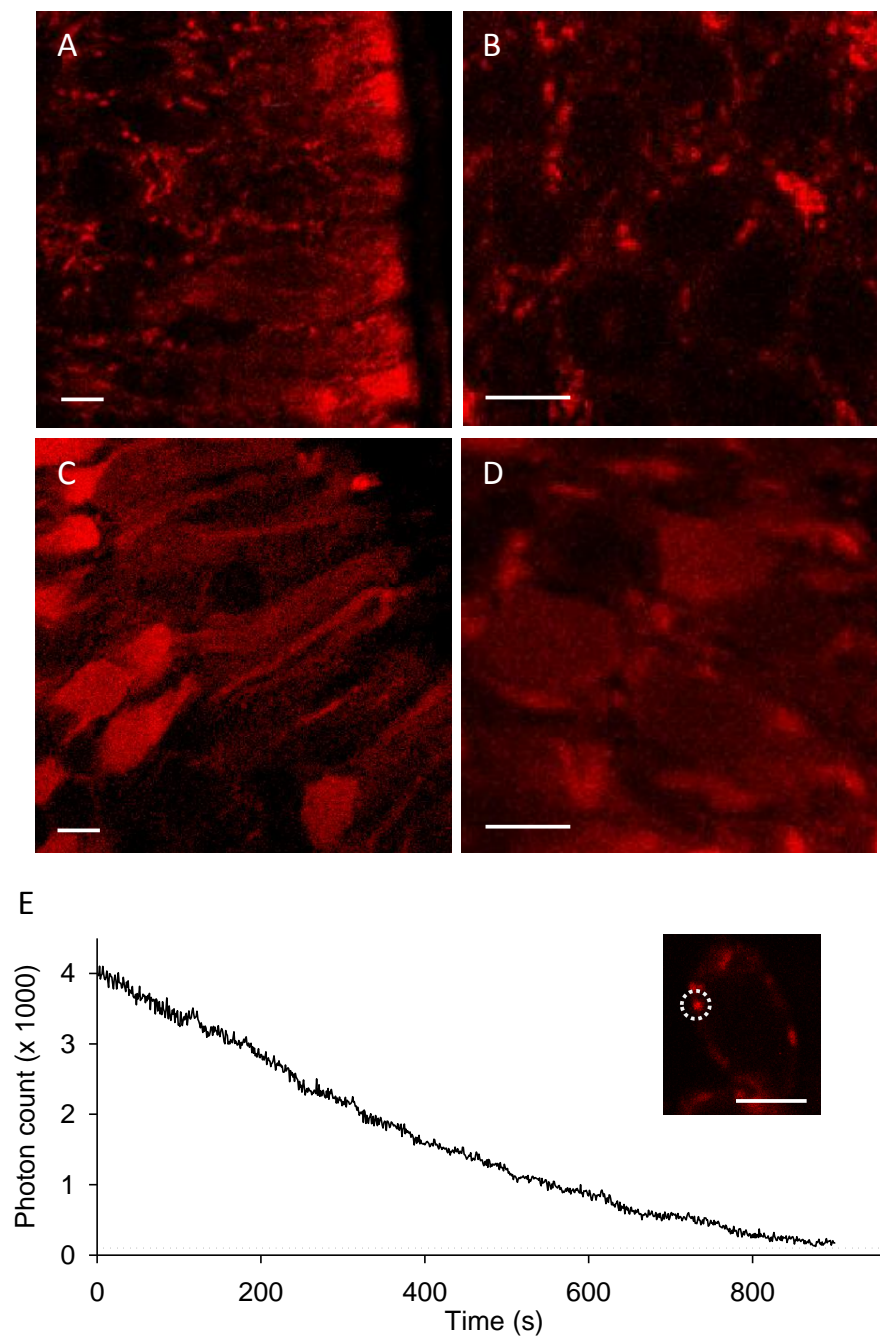
Figure 13. Staining BK channels with Alexa labeled Iberiotoxin in fixed slices

(A) and (B) Slices stained with Alexa 546 labeled IbTx. Images were taken in a two photon excitation cLSM with $40\times$ (A) and $63\times$ (B) objectives. (C, D) Slices stained with Alexa 546 alone and taken with $40\times$ (C) and $63\times$ (D) objectives. All scales are 5 μm. (E) Fluorescence signal of one ROI (white circle) in the superimposed image stained by labeled IbTx. A dashed line indicates a background photon count of ~100 photons/s in these fixed samples.
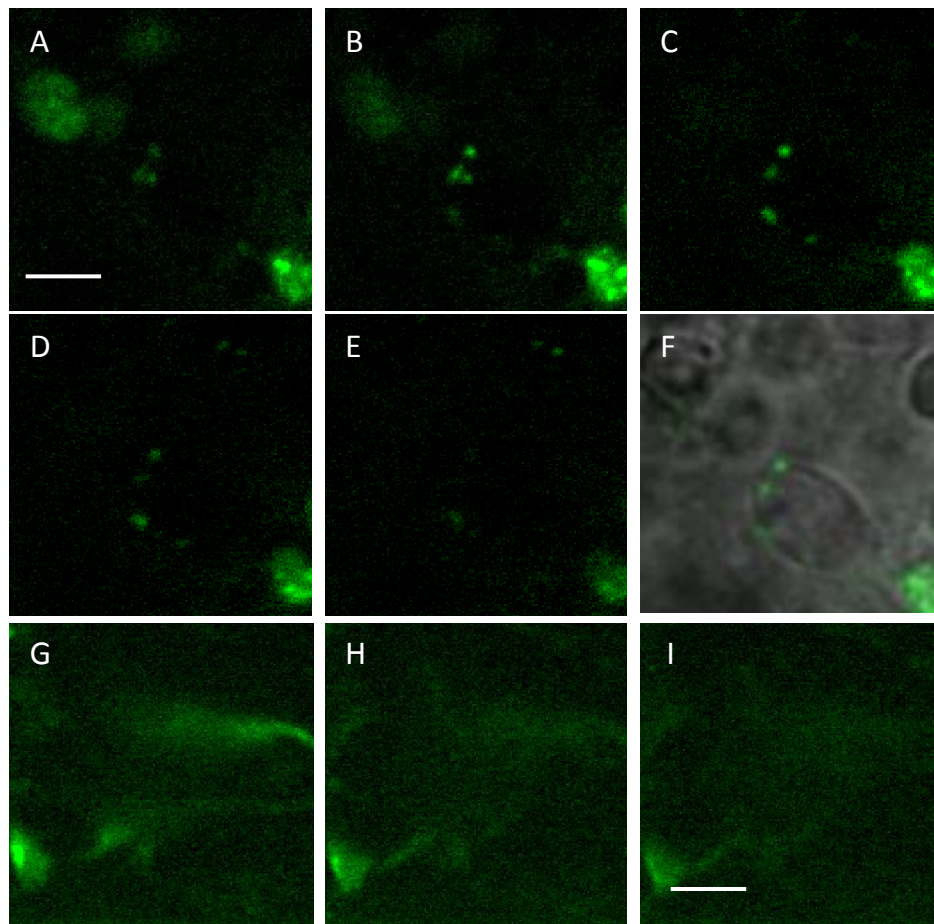
Figure 14. Staining BK channels with Alexa labeled Iberiotoxin in living slices

(A) - (E) Fluorescence images of a z-stack from slices stained with Alexa 488 labeled IbTx. Images were taken in the same setup as the Ca^{2+} imaging experiments. (F) Bright field image merged with A to E. (G)-(I) Z-stack images from slices stained with Alexa dye alone. All scales are 5 μm.
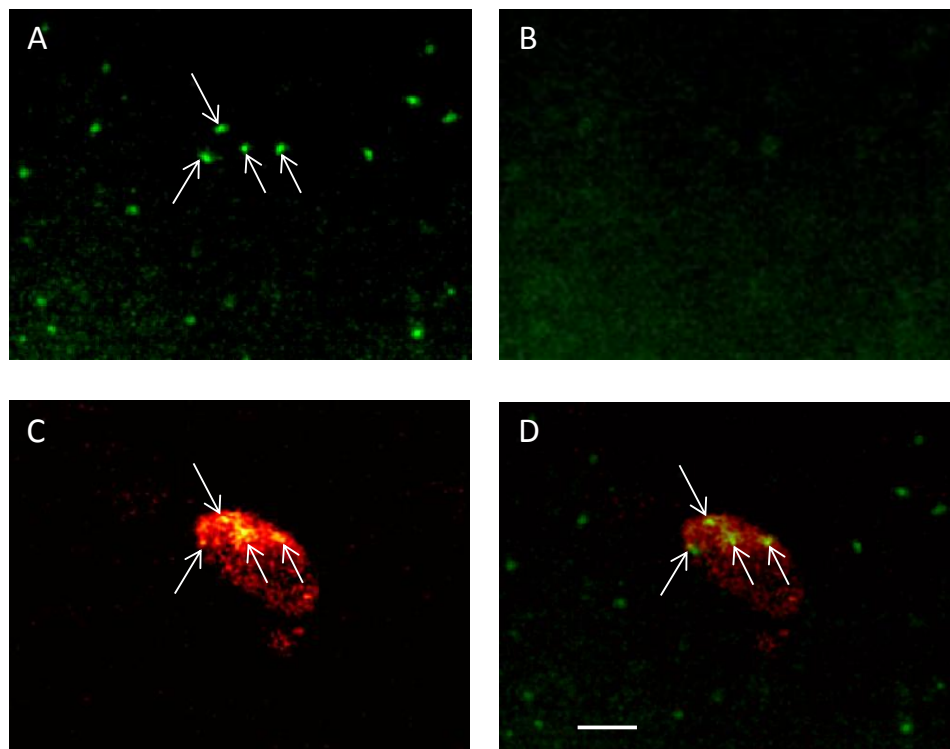
Figure 15. Co-localization of BK channels and Ca^{2+} microdomains

(A) Image of BK channels stained with Alexa 488 labeled IbTx. (B) Image after washing for 30 min after staining. (C) Image of Ca^{2+} microdomains during depolarization, the control prior to the depolarization has been subtracted. Images of (A), (B) and (C) are maximum projections of z-stacks. (D) Merge of (A) and (C). Arrows indicate co-localization of BK channels and Ca^{2+} microdomains. Scale, 5 μm.
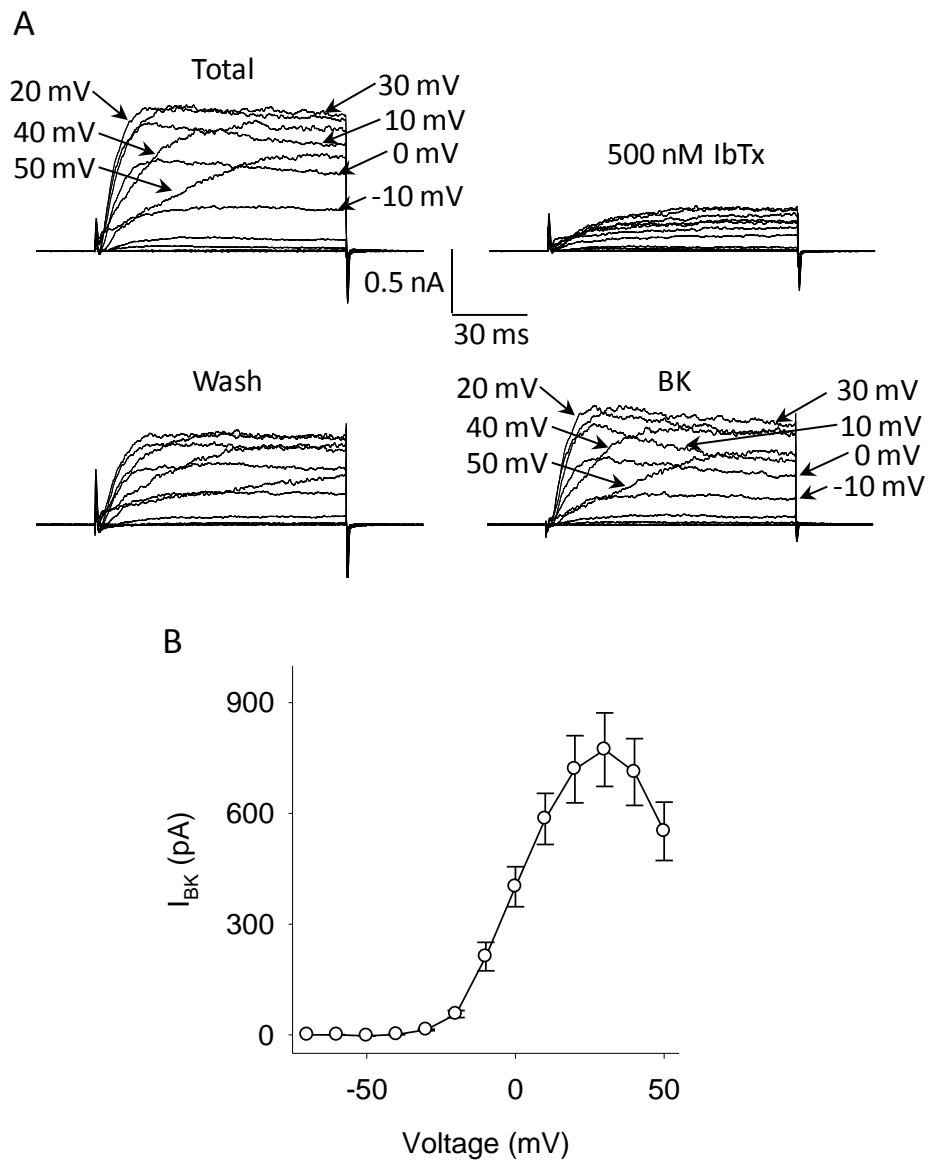
Figure 16. Whole-cell BK channel currents and IV curves in ORNs of *Xenopus laevis*
Whole-cell currents were induced by successively depolarizing pulses in 10-mV steps from
-60 to 50 mV for 100 ms. (A) Current recorded in normal bath solution (Total), after
incubation of IbTx (500 nM, 3 min), and after washout (Wash). The BK channel current (BK)
was obtained by subtracting the current after IbTx incubation from the total current. (B)
Average BK channel current/voltage (IV) curves (n=4).
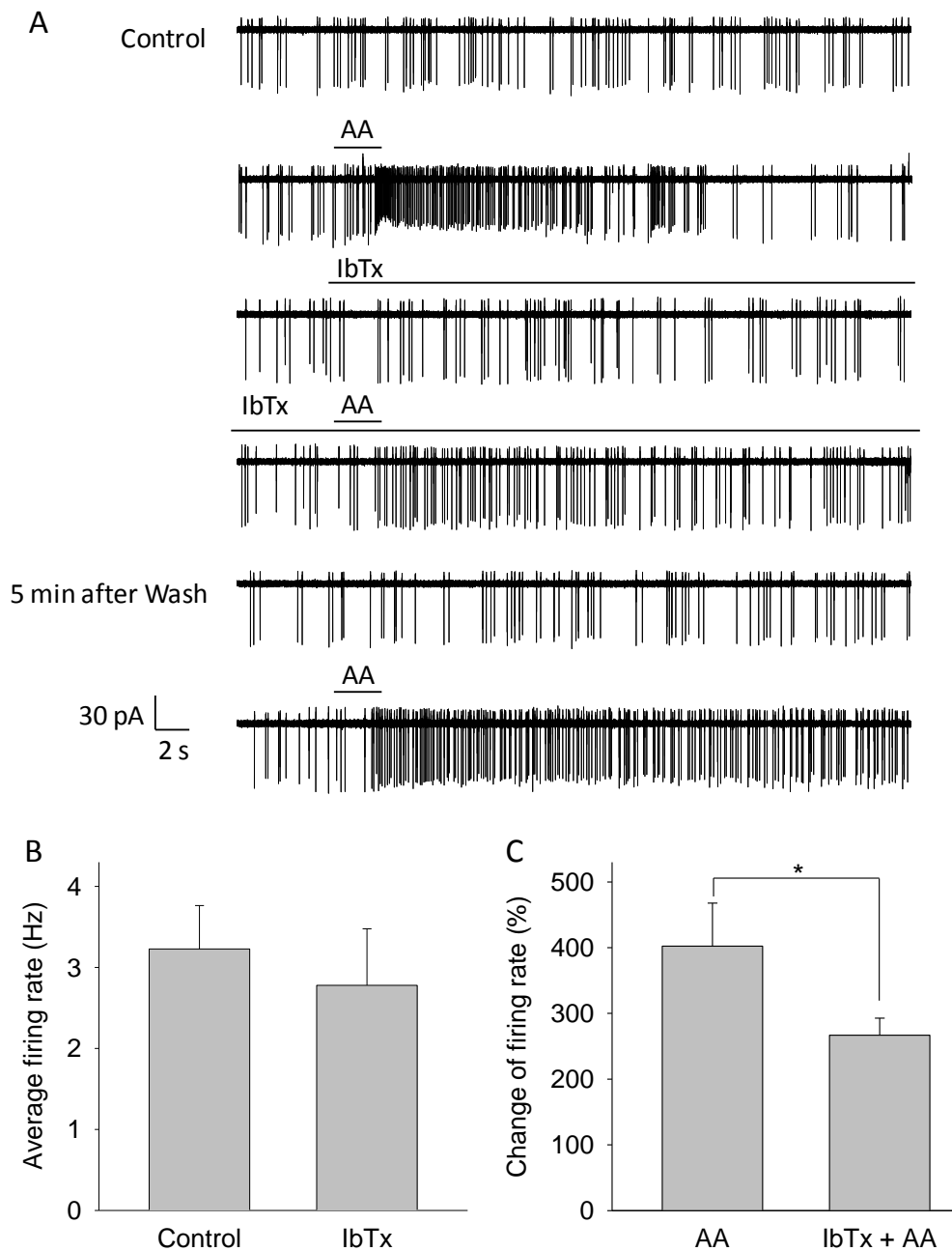
Figure 17. Blocking BK channels reduces the firing rate on odorant responses

ORNs of mucosa slices from tadpoles of stage 53 were recorded in on-cell mode. (A) From top to bottom, current trace of: spontaneous firing (Control), response to amino acid mixture (AA), response after incubation of IbTx, response to amino acid mixture together with IbTx (IbTx + AA), response after 5 min washing with bath solution, and response to amino acid mixture again. (B) Summary statistics for average firing rate of spontaneous activity (Control) and of response after incubation of IbTx. (C) Change of firing rate on application of odorants alone (AA) or together with IbTx after IbTx incubation (IbTx + AA) as compared before AA and IbTx+AA applying. * p<0.05, Student's *t* test, n=12.
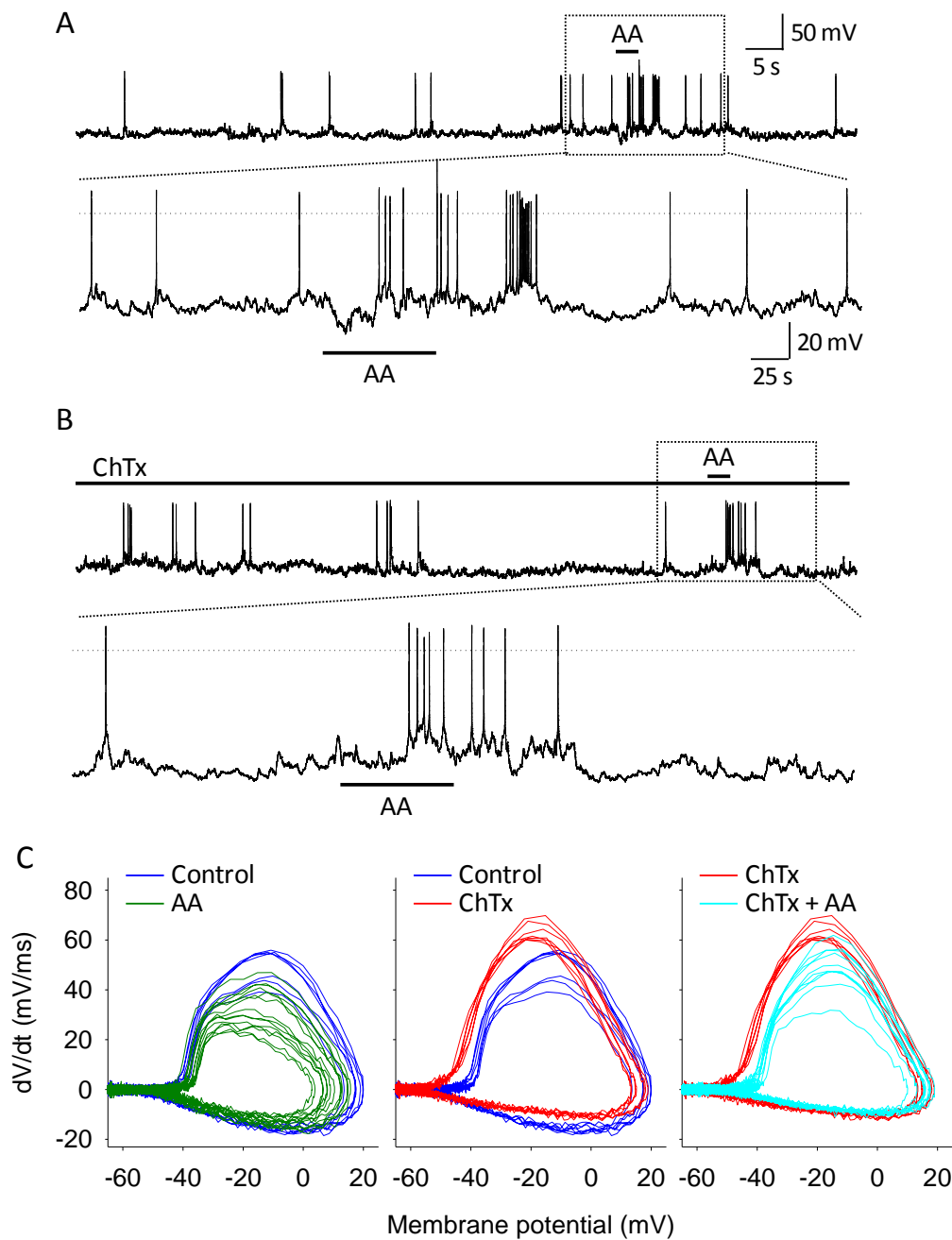
Figure 18. Changes in whole-cell recording with BK channels blocked
(A) and (B) Examples of voltage trace (top) and its enlarged view (bottom) from an ORN in whole-cell recording mode in response to the mixture of amino acids (AA) before (A) and 3 min after (B) ChTx incubation. (C) Phase plot (dV/dt versus V) of the APs from that voltage traces. Left to right: comparison of APs before (Control) and after (AA) application of amino acid mixture (left), before (Control) and 3 min after ChTx incubation (middle); before (ChTx) and after (ChTx + AA) applying amino acid mixture during ChTx incubation.
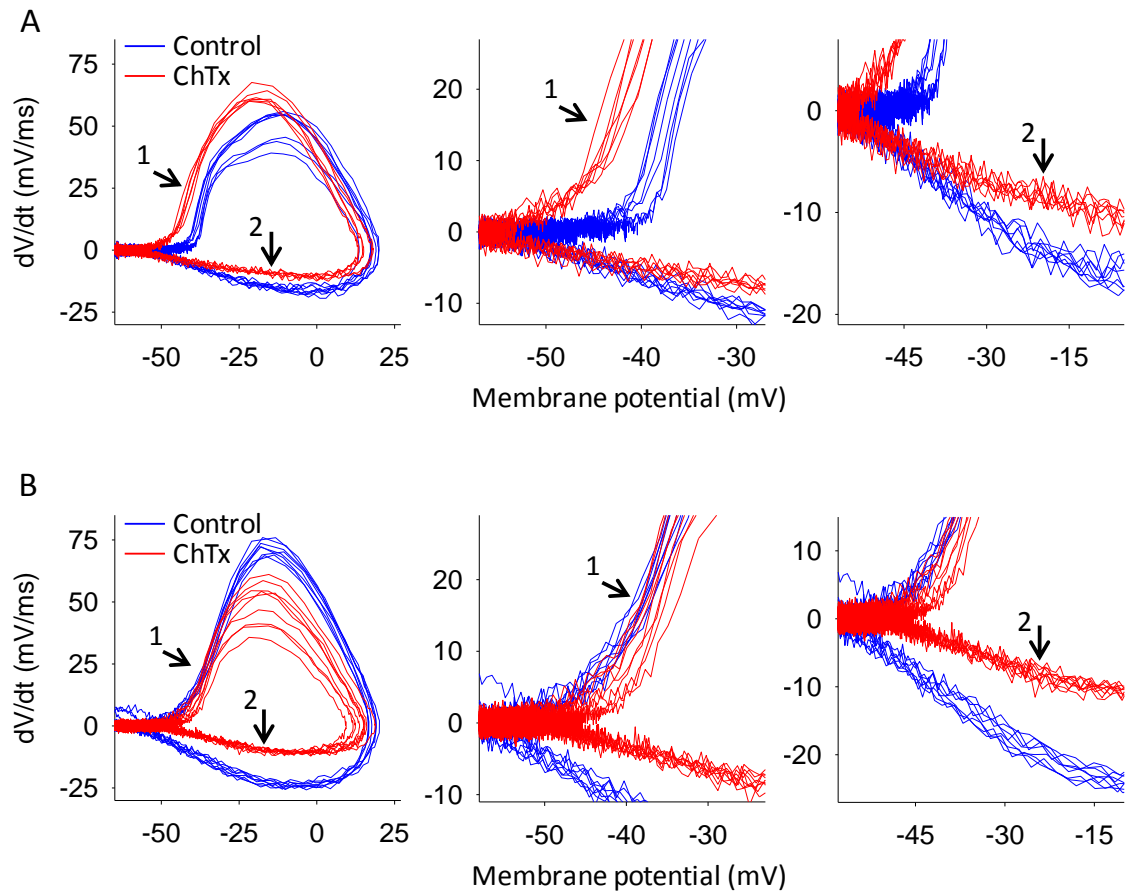
Figure 19. Differences in phase plots due to block of BK channels

(A) and (B) Phase plots and the enlarged views as indicated by the arrows in the initiation sites of action potentials (1, middle) and the falling phase of action potentials (2, right), before (Control, blue lines) and 3 min after (ChTx, red lines) incubation of a BK channel blocker, ChTx.
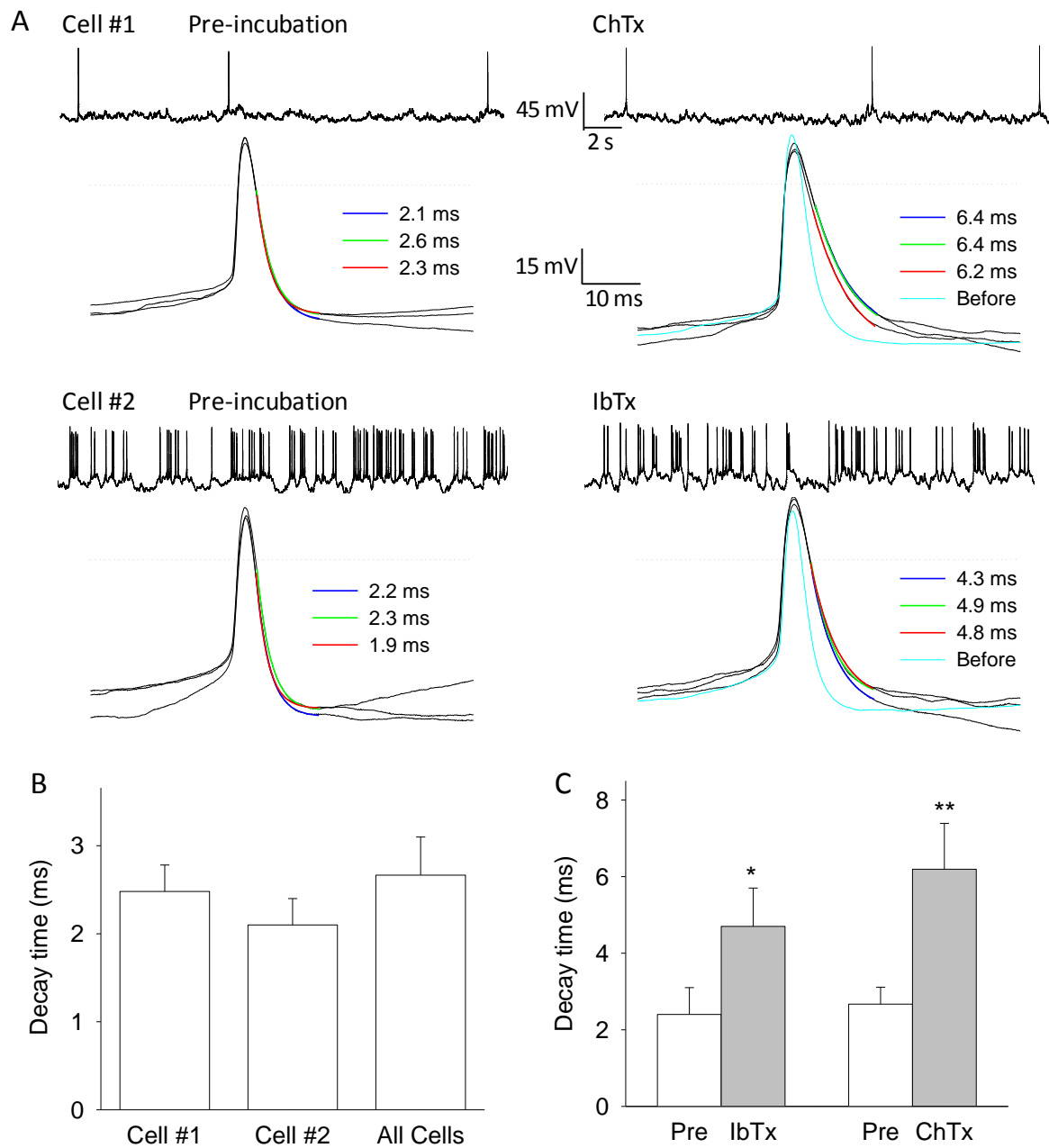
Figure 20. Blocking BK channels slows the falling phase of spontaneous action potentials
ORNs were recorded in whole-cell current-clamp mode. (A) Examples of voltage traces and individual APs from two neurons with low (Cell #1) and high (Cell #2) basal activities, before (Pre-incubation) and 3 min after ChTx or IbTx incubation. Superimposed: decay times of falling phase under single-exponential fittings. (B) Comparison of decay times in basal activity. (C) Comparison of decay times before (Pre) and 3 min after IbTx (n=5) or ChTx (n=6) incubation. * $p<0.05$, ** $p<0.01$, Student's t test.
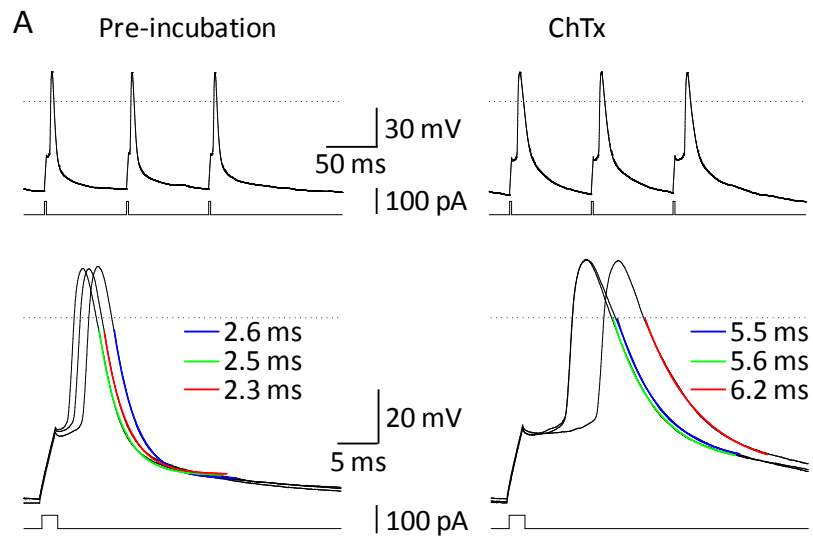
Figure 21. Blocking BK channels slows the falling phase of induced action potentials
ORNs were recorded in whole-cell current-clamp mode. (A) Top: voltage traces of three APs
elicited by 2 ms depolarizing current injection pulses before (Pre-incubation) and 3 min after
ChTx incubation; bottom: enlarged view showing the results of single-exponential fitting.
Superimposed: decay times of falling phase by single-exponential fittings.
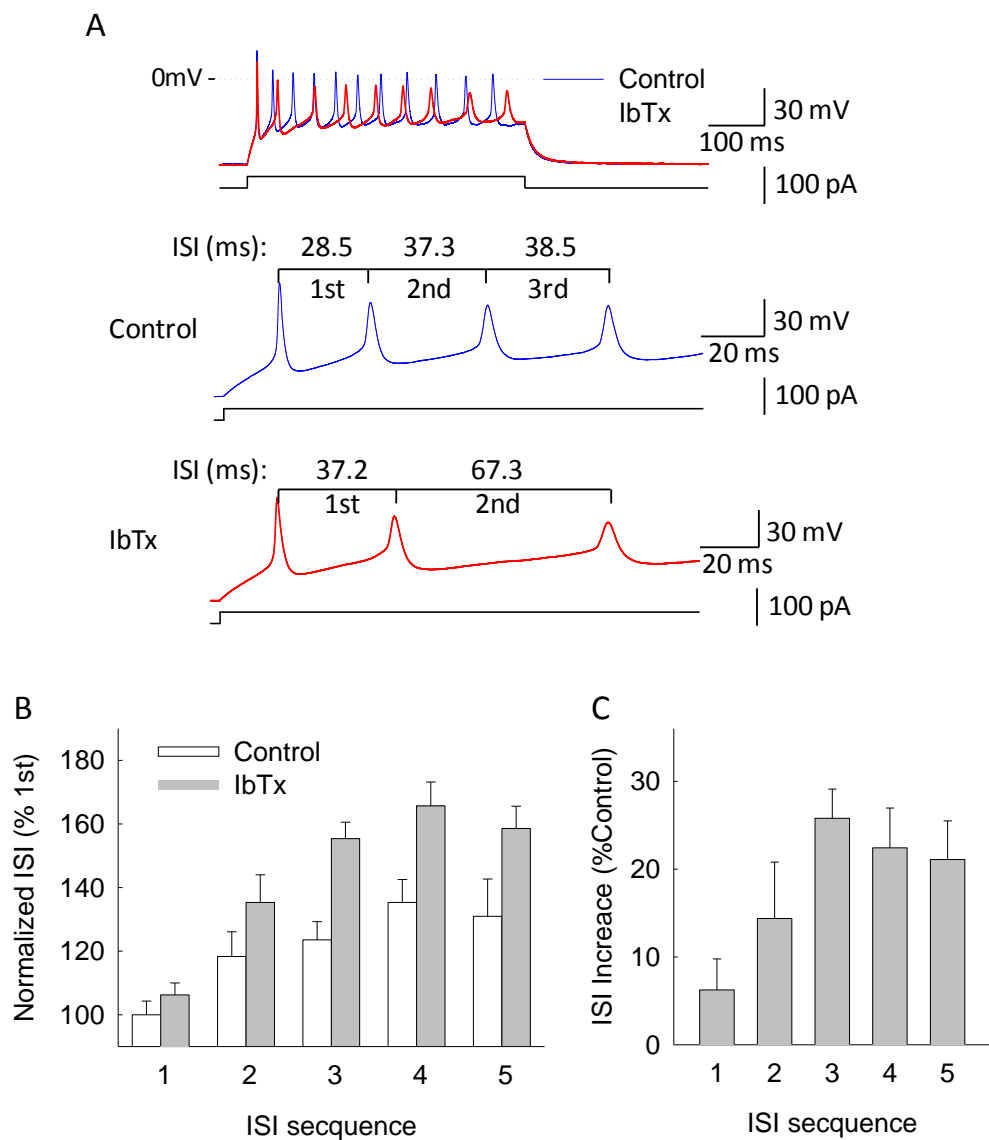
Figure 22. Blocking BK channels enlarges interspike intervals

ORNs were recorded in whole-cell current-clamp mode. (A) Voltage traces of spike trains in response to a brief current injection (30 pA, 500 ms, black line) before (control, blue line) and 3 min after (red line) IbTx incubation. Top: overview of the voltage traces; middle and bottom: enlarged view showing early part of the spike trains before (middle) and after (IbTx) incubation. Superimposed: times of ISIs. (B) Summary plot of the changes in the first 5 ISIs of spike trains before and after IbTX incubation. (C) Summary plot showing the increases of the first 5 ISIs after IbTx treatment as compared to the corresponding controls along the sequence.
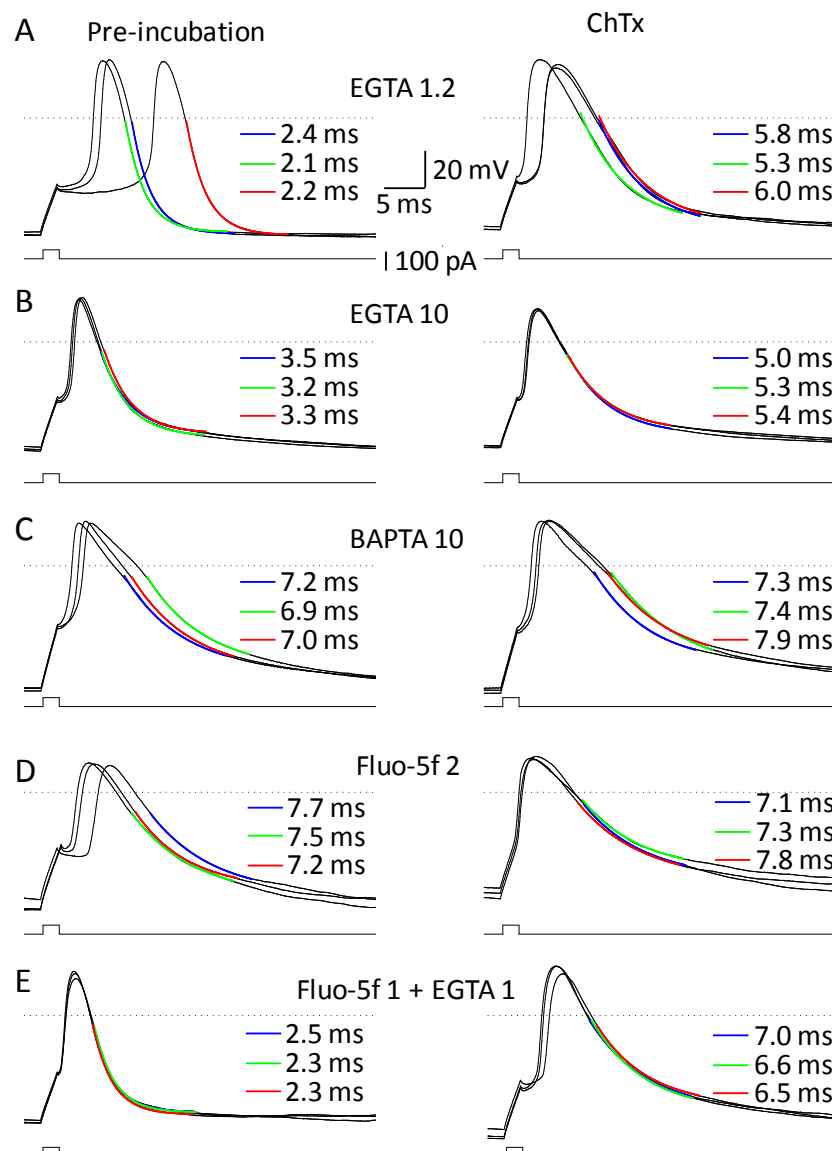
Figure 23. Effect of different Ca^{2+} chelators on the induced action potentials

ORNs were recorded in whole-cell current-clamp mode. APs were elicited by injection of 3-ms, 50-pA current pulses. (A) to (E) Influence of APs with intracellular solutions of different Ca^{2+} chelators before (Pre-incubation) and 3 min after ChTx incubation. Each intracellular solution contains from (A) to (E), 1.2 mM EGTA (A), 10 mM EGTA (B), 10 mM BAPTA (C), 2 mM Fluo-5f (D), or Fluo-5f plus 1mM EGTA. Superimposed: decay times of falling phase by single-exponential fittings.
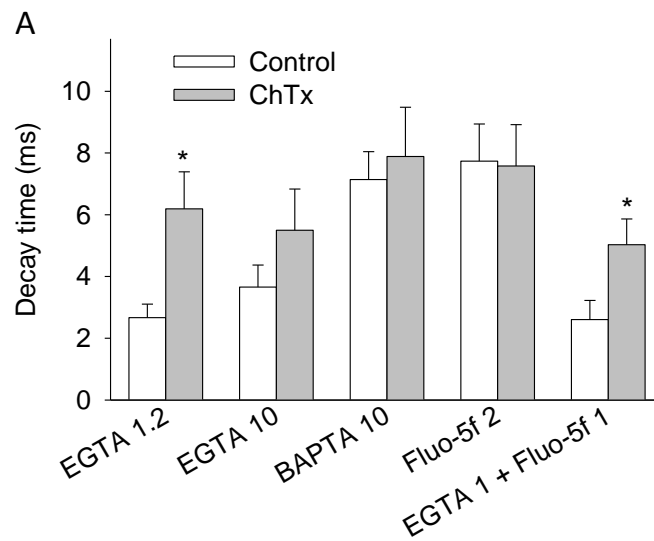
Figure 24. Comparison under different intracellular solutions

Summary statistics for Figure 23, average decay time of induced APs compared before (control) and 3 min after ChTx incubation. Different intracellular solutions from left to right were 1.2 mM EGTA, 10 mM EGTA, 10 mM BAPTA, 2 mM Fluo-5f, and 1mM Fluo-5f plus EGTA. * $p<0.05$, Student's *t* test, n=6 in each group.
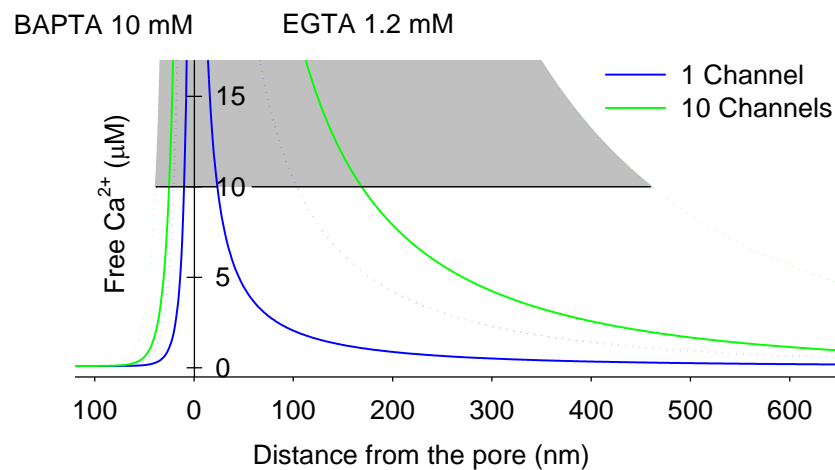
Figure 25. Simulation of [Ca^{2+}] profile near channel center of Ca^{2+} microdomains

Free [Ca^{2+}] is calculated in a condition with BAPTA 10 mM (Left) and EGTA 1.2 mM (right), with one (blue) and 10 (green) Ca^{2+} channels. The solid lines show the low boundary with single channel current of 0.17 pA and open probability of 0.7, and the dashed lines are the high boundary with single channel current of 0.7 pA and open probability of 0.9. Parameters: [Ca^{2+}]$_\infty$=0.1 μM, D=400 μm^{2}s^{-1}, for EGTA, K$_{on}$ = 2.5×10^6M^{-1}s^{-1}, K$_d$ = 0.22 μM; for BAPTA, K$_{on}$ = 4×10^8M^{-1}s^{-1}, K$_d$ = 0.50 μM, are taken from literatures (Wu, 1996; Smith 1996).

4. Discussion

4.1 Main conclusions

The main conclusion in the present study is that the voltage-gated Ca^{2+} channels in the olfactory receptor neurons of *Xenopus laevis* are neither evenly distributed nor separately or randomly arranged throughout the cell membrane. In contrast, they tend to gather in some relatively tiny areas in which the propagations of Ca^{2+} influxes via these Ca^{2+} channels are diffusion-limited and will likely form high Ca^{2+}-concentration microdomains measuring a few hundred nanometers. And interestingly, the BK channels also tend to locate nearby.

Moreover, the interesting findings in the present study are also due in part to the appearance of a small Ca^{2+} current and a few Ca^{2+} microdomains in the individual olfactory receptor neurons. The recorded Ca^{2+} current in a single neuron (10–80 pA at -10 mV, Fig. 9C) is too small to be simply detected with a patch-clamp method in physiological conditions (Schild, 1989), and the observed Ca^{2+} channel number per neuron (33 ± 18, Fig. 5C) is even less than the average channel number per "hotspot" of a cochlear hair cell (Roberts 1990; Wu 1996; Bortolozzi *et al.*, 2008). Needless to say as well, there are very few Ca^{2+} microdomains discovered in single neurons (6 ± 3, Fig. 7C) when Ca^{2+} channels are likely congregated (5–25 channels per Ca^{2+} microdomains, Fig. 10B). Nevertheless, it is proved that such a few Ca^{2+} microdomains with the co-localized BK channels (Fig. 15) still confer important functions to the olfactory receptor neurons, shaping the action potentials (Fig. 18–21) and facilitating the firing rates in response to the odorant stimuli (Fig. 17 and 22), which may play a key role in olfactory signal transduction.

4.2 Ca^{2+} microdomains and their co-localization with BK channels

4.2.1 Voltage-dependent Ca^{2+} microdomains in olfactory receptor neurons

The present study demonstrates that Ca^{2+} microdomains which were observed by applying a Ca^{2+} indicator, Fluo-5f, and depolarization of the membrane potential, are

widely present in olfactory receptor neurons of *Xenopus laevis*. Except in a few cases where the likely reason could be that the neurons were unhealthy, more than 80% of the olfactory receptor neurons revealed the existence of at least one to about ten such spatially confined and high Ca^{2+}-concentrated microdomains with a voltage-dependent property.

Generally, the appearance of a Ca^{2+} microdomain requires a condition of Ca^{2+} compartmentalization, which is determined by a local Ca^{2+} source (for example, the Ca^{2+} channels), and importantly, by a fast Ca^{2+} removal mechanism: the endogenous mobile and immobile Ca^{2+} buffers, typically, the Ca^{2+} binding proteins (Naraghi and Neher, 1997; Rizzuto and Pozzan, 2006). However, with the whole-cell configuration like what was done in the present experiments, the endogenous mobile Ca^{2+} buffers might be gradually replaced by the main Ca^{2+} chelators applied in the intracellular solutions, and the recorded fluorescence images of Ca^{2+} microdomains were also merely the concentration profiles of Ca^{2+}-bound dyes under artificial buffer conditions. Nonetheless, the present observations still to some extent depict the real spatial and temporal aspects of Ca^{2+} distributions around the Ca^{2+} sources. Particularly, the property like the observed voltage dependency, which might be shifted due to the change of Ca^{2+} reversal potential caused by different Ca^{2+} buffer systems, cannot be fully eliminated in a real intact neuron. Therefore, the observation of voltage-dependent Ca^{2+} microdomains is indeed a widespread phenomenon which exists among the olfactory receptor neurons of *Xenopus laevis*, and will perform key functions in cell signaling.

4.2.2 Voltage-gated Ca^{2+} channels in Ca^{2+} microdomains

As to the Ca^{2+} sources in the observed Ca^{2+} microdomains, a reasonable inference is L-type voltage-gated Ca^{2+} channels. The evidence includes the following observations and facts.

First, there may be only one type of voltage-gated Ca^{2+} channels in the surface

membrane of olfactory receptor neurons. Although the observed number of Ca^{2+} channels in the individual neurons covers a wide range from 10 to about 80 (Fig. 5C), the distribution of single channel current is still relatively narrow, and two thirds of the values is mainly in a small rage (0.4–0.7 pA; Fig. 5D), implying the existence of one dominant channel type.

Second, if the single channel current is not accurate enough, that the straight line perfectly fits the experiment data in Fig. 9C (see section 3.3.2) may provide a more definitive answer. The slope of that line, $k = i(1 - P_o)$, indicates that the product of the single channel current (i) and probability for the channel to be closed (1-P_o) is constant. Although the value i cannot be definitely estimated, the constant k still implies the presence of Ca^{2+} channels with the same single channel current (i) and open probability (P_o), which are likely the same channel type. Otherwise, in order to show still a line in the plot of current variance against mean, the assumption of different channel types with different i or P_o values will result in a more complicated paradox where the channels of different types have to express in a constant proportion regardless of their absolute expression levels in individual neurons (For the calculation detail see Appendix ii). However, such a strong correlation in expression levels of different channel types throughout all the neurons seems rarely possible. So, the simple explanation, namely only one type of Ca^{2+} channels being dominantly expressed, is preferred.

Third, there was little inactivation in the recorded Ca^{2+} current (Fig. 4 and 9A), and the maximal activation of the current was between -10 to 0 mV (Fig. 4B). Both findings are consistent with the characteristics of a Ca_v1 subfamily channel, the classical L-type (Long-lasting) Ca^{2+} channel, which is activated by high voltage around -10 to +10 mV and slow to inactivate (Tsien *et al.*, 1988). Since, neither any big transient nor big inactivation component was observed, another two types of transiently activated Ca^{2+} channels, the classical T-type (Transient current) channel (Ca_v3 subfamily) and R-type channel (Ca_v2 subfamily) (Randall and Tsien, 1997),

were all unlikely to give much contribution and therefore could be excluded. Additionally, a genetic research on the database of *Xenopus tropicalis* shows so far only the L-, T- and R-type genes being found (see appendix iii), suggesting that the Ca^{2+} channels like P/Q- and N-type (all are Ca_v2 subfamily) might also be excluded. Moreover, as shown in Fig. 4E, despite a slight decrease in vehicle-treated control probably due to the rundown of Ca^{2+} channels, a significant inhibition of the Ca^{2+} current by nimodipine, a dihydropyridine L-type Ca^{2+}-channel selective antagonist, was still observed, further indicating that the recorded Ca^{2+} current consisted dominantly of an L-type current. It has also been noticed that there was still a small non-inactivating Ca^{2+} current left (Fig. 4C) after the application of nimodipine (~20 μM). Considering, on the one hand, that different L-type Ca^{2+} channels might have different sensitivities to dihydropyridines, for example, ~90% of $Ca_v1.2$ current is inhibited by 1 μM nimodipine but the same concentration inhibits only about 50% of $Ca_v1.3$ current (Xu and Lipscombe, 2001); considering, on the other hand, that the solubility of nimodipine in water is extremely low which is around 2.3 mg/L (~5.5 μM; Yang and Ren, 2003) and 20 μM is almost the highest concentration that can be achieved with 0.2% or less DMSO in solution; therefore, the left part of the non-inactivating current could still be the L-type current due to the incomplete blocking of the channels.

The last but most important one is that in the present study, both the fluorescent signals of individual Ca^{2+} microdomains in Ca^{2+} imaging (Fig. 8D) and the Ca^{2+} current signals in whole-cell recording (Fig. 9A) reveal similar shapes and inactivation properties during the 200-ms depolarizing test-pulses, indicating that it is the same voltage-gated Ca^{2+} channel type that generates the currents and forms the Ca^{2+} microdomains. Besides, during Ca^{2+} imaging, a Cs^+-based intracellular solution was always used, which would bloke the Ca^{2+} induced Ca^{2+} release (Kennedy and Meech, 2002), suggesting that the Ca^{2+} induced Ca^{2+} release would not necessarily contribute to the observed Ca^{2+} microdomains.

Taking into account all the arguments, a conclusion with very high possibility can be drawn: in olfactory receptor neurons of *Xenopus laevis* the main Ca^{2+} sources for the voltage-dependent Ca^{2+} microdomains are the L-type voltage-gated Ca^{2+} channels.

However, it shouldn't be fully excluded that under a real physiological condition there might be an involvement of Ca^{2+} induced Ca^{2+} release in Ca^{2+} signaling of these neurons. Since the Ca^{2+} induced Ca^{2+} release may use the same Ca^{2+} sources as the Ca^{2+} microdomains, if they would give some contributions, they should also show coincident effects with a certain delay which would correspond to the Ca^{2+} diffusion and the buffering environments. Consequently, they would either intensify the Ca^{2+} transients in the Ca^{2+} microdomains directly like a positive feedback if the Ca^{2+} was released to the same areas, or relay the Ca^{2+} signals to the next effectors if the Ca^{2+} was released to somewhere else inside the cells. For this point of view, a further study is worthwhile and will possibly exhibit another important pathway of Ca^{2+} signaling from the L-type Ca^{2+} channels of Ca^{2+} microdomains to Ca^{2+} induced Ca^{2+} release in olfactory receptor neurons of *Xenopus laevis*.

4.2.3 Single channel versus channel cluster

In the present study, the number of Ca^{2+} microdomains per olfactory receptor neuron, which was counted using a method combined the patch-clamp technique and confocal Ca^{2+} imaging, was around 1–13 with an average of 6 (Fig. 6 and 7); and the number of voltage-gated Ca^{2+} channels per neuron, which was examined using a non-stationary fluctuation analysis of whole-cell Ca^{2+} tail currents, was about 10–80 with an average of 33 (Fig. 5).

The two numbers show a marked difference and especially the smaller number in the Ca^{2+} microdomains seems to imply that the Ca^{2+} microdomains are composed of multiple Ca^{2+} channels like channel clusters. However, owing to the noise in the Ca^{2+} imaging it was sometimes difficult to decide (less than 20%) whether an irregularly shaped microdomain was formed by a single domain or the fusion of multiple

domains (2 or 3 at most), whereby the number of microdomains might have been underestimated with an estimated error of 20 to 30% (maximum). On the other hand, due to the rundown of the Ca^{2+} tail currents that fewer and fewer channels would be activated, the number of Ca^{2+} channels might have also been underestimated with a maximum error of ~30%. Thus, there are still differences between these two numbers; and no matter how the Ca^{2+} channels are distributed, at least some if not all Ca^{2+} microdomains may arise from Ca^{2+} channel clusters.

Another argument is that these two quantitative results were not performed in the same neurons but in two different experiments with two batches of neurons, and in one experiment for the detection of Ca^{2+} microdomains, additional Fluo-5f was even applied in the intracellular solution as a Ca^{2+} indicator. Thus, it cannot be wholly excluded that the Ca^{2+} channels in the appearance of the Ca^{2+} indicators become somehow silent. This possibility might be one argument against the former hypothesis, because, instead of forming channel clusters, the smaller count of Ca^{2+} microdomains can also be due to the less number of activated Ca^{2+} channels.

Nevertheless, it can be further found from the electrophysiological data of those two experiments that although the amplitudes of whole-cell Ca^{2+} currents are different from cell to cell, the average currents of those experiments are still comparable. And in a separated experiment, the adding of Fluo-5f did not significantly change the amplitude of the Ca^{2+} current or shift the current-voltage relationships as was presented in Fig. 4B, implying that there are no considerable differences in the total number of activated Ca^{2+} channels in those different experiments. Therefore, the smaller number of Ca^{2+} microdomains compared to that of the Ca^{2+} channels most likely suggests the existence of Ca^{2+} channel clusters in some Ca^{2+} microdomains. If all the Ca^{2+} channels are equally spread among the Ca^{2+} microdomains, a value of 5-6 channels per microdomain can be expected.

An optical fluctuation analysis was employed in further experiments and the

determined number of Ca^{2+}-channels per Ca^{2+} microdomain was around 12 ± 5 (Fig. 10B). The standard error of 5 which is about 40% seems to indicate that the distribution covers a wide range. It is noticeable that there is a peak around 6 in the distribution chart, implying that about 1/3 of the Ca^{2+} microdomains are in accordance with an equally spread distribution, namely 5–6 Ca^{2+}-channels per Ca^{2+} microdomain. However, it also implies that another 2/3 may contain more channels, which are around 10–25. For the appearance of such a broad distribution, there might be two possibilities. One is that spatially adjacent microdomains cannot be separated in the experiment and has been treated as one microdomain, indicating a close link in space between those Ca^{2+} microdomains. Or, the other more interesting possibility is that there is a basic unit composing the Ca^{2+} microdomains, and each observed microdomain is formed by one up to maximum of like four of such units, suggesting the existence of a unitary Ca^{2+} channel cluster maybe with 5–6 channels, acting as a building block of Ca^{2+} microdomains. For this point of view, further studies will be necessary to explore the detailed distribution of the Ca^{2+} channels throughout the Ca^{2+} microdomains. Nonetheless, the optical fluctuation analysis again confirm that Ca^{2+} microdomains in olfactory receptor neurons of *Xenopus laevis* consist of not completely single Ca^{2+} channels but mainly Ca^{2+} channel clusters.

4.2.4 Voltage dependency and co-localization of BK channels

Functionally, the presence of voltage-dependent Ca^{2+} microdomains enables the local control of cellular processes that need to be restricted in time and space. Such locally controlled processes by Ca^{2+} microdomains in olfactory receptor neurons are likely the activation of BK channels, which are activated very accurately during each falling phase of the action potentials (Fig. 20 and 21). Intuitively, one can imagine that the activation timing of BK channels is adjusted by the diffusion of Ca^{2+} influx through a proper distance between the Ca^{2+}-channel pole and the BK channel Ca^{2+}-gating regions. Therefore, the co-localization of BK channels and Ca^{2+} microdomains will have an obvious physiological significance.

In the present study, the BK channels which were stained by the Alexa-IbTx (a fluorophor-labeled BK channel antagonist), can be clearly identified in both the living (Fig. 14 and 15) and fixed slices (Fig. 13) as puncta throughout the surface membrane of the olfactory receptor neurons. It is noteworthy that an almost perfect overlap between the BK channel puncta and the Ca^{2+} microdomains is demonstrated in the living slices (Fig. 15), suggesting a co-localization of BK channels and Ca^{2+} microdomains. Since the Ca^{2+} microdomains are indicated by the function of voltage-gated Ca^{2+} channels via depolarizations, such co-localization of BK channels and Ca^{2+} microdomains further suggests that BK channels and Ca^{2+} channels are spatially very close to each other and very willing to form functional microdomains.

4.3 Mechanisms of BK channels

4.3.1 Functions of BK channels relating to the action potentials

As discussed before, the existence of BK channels in the Ca^{2+} microdomains makes it feasible to control the cellular processes that need to be restricted in time and space. The present data have revealed that the increase in firing rate of olfactory receptor neurons by applying the amino acid mixture reduced significantly when BK channels are blocked (Fig. 17 and 18). This suggests that in those neurons the functions of BK channels are involved in neuronal responses to odorant stimuli. Moreover, blocking BK channels slows the falling phase and enlarges the inter-spike interval of action potentials (Fig. 18–22), which are all events in millisecond-ranges, implying that the activation of BK channels are under a precisely temporal control, especially corresponding to individual action potentials. As BK channels are K^+ channels with a large single-channel conductance, the activation of BK channels just prior the falling phase of action potentials, which will speed up the membrane hypopolarization because of the increase in a potassium conductance, is a most likely hypothesis to interpret the effects of BK channels in olfactory receptor neurons. The question now is how the BK channels can be activated so precisely?

4.3.2 Activation of BK channels under the control of Ca^{2+} diffusion

As mentioned before, the precise timing of BK channel activation can be controlled by a diffusional distance between BK channels and Ca^{2+} channels, which is a simple and reliable way for Ca^{2+} microdomains to synchronize the triggering of BK channels with a precise delay. Imagine that once the Ca^{2+} channels are activated during the rising phase of an action potential, the Ca^{2+} influx will rely on the diffusion time, until reaching a proper concentration in a certain position where the BK channels are located, thus starting the BK channels there.

Some of the evidence is based on the observation that different influences of action potential falling phases occur under different intracellular solutions containing Ca^{2+} buffers with different Ca^{2+} binding kinetics. It has been found that 10 mM BAPTA could mimic the effect of BK channel antagonist, which not only slowed down the falling phase of action potentials dramatically but also abolished the further effect of the antagonist (Fig. 24C and 25). However, such influence did not occur when 1.2 mM EGTA was used (Fig. 24A and 25), whereas when 10 mM EGTA was applied, the influence was likely in a middle state (Fig. 24B and 25). Regarding other findings such as the single Ca^{2+} channel current, the open probability, and the channel number per microdomain, the proper distance between BK channels and Ca^{2+} channels has been thus estimated, which was around 50–200 nm but no less than 30 nm (Table 4, Section 3.6.6).

Loading cells with exogenous Ca^{2+} binding substances is a well known method to influence the decay kinetics of intracellular spatially distributed free Ca^{2+}. With the whole-cell configuration, not only can exogenous Ca^{2+} buffers be introduced, but also endogenous mobile Ca^{2+} buffers can be gradually removed (Zhou and Neher, 1993). Consequently, the distance between the target and the Ca^{2+} source can be analytically distinguished depending on whether the introduced substances have fast or slow Ca^{2+}-binding kinetics (Neher and Augustine, 1992; Lee *et al.*, 2000). For example, the distance is within several ten nanometers if the processes between the target and Ca^{2+}

source are effectively interfered with by BAPTA, but not by EGTA, or, the targets are mostly far away from the Ca^{2+} source and the distances are beyond a few hundred nanometers if the processes are equally sensitive to BAPTA and EGTA (Fakler and Adelman, 2008).

Following the same idea, the present finding also suggests that the distance between BK and Ca^{2+} channels is neither very far at least within the range that 1.2 mM EGTA cannot show any effect, which is around a few hundred nanometers; nor very close at least beyond the distance that 10 mM BAPTA can exert its function, which is around several ten nanometers. So, the distance between BK and Ca^{2+} channels, which is around 50–200 nm but no less than 30 nm, is a reasonable estimate.

4.3.3 Adaptation for a low-frequency signal

A previous report shows that in cortical neurons (mainly in hippocampus), single Ca^{2+} channels can already contribute to action potential repolarization (Müller, 2007). Their conclusion that the diffusional distance between BK and Ca^{2+} channels is 13 nm, is much shorter than the current finding. However, it has been noticed that the duration of action potentials which is around 1 ms in cortical neurons in that report (Müller, 2007) is also much shorter than that of the current finding which is around 5–7 ms in olfactory receptor neurons of *Xenopus laevis*.

It is well known that the odor is the sensation resulting from stimulation of the olfactory organs by the odorant, a substance capable of passing through the mucous layer to the cilia of the olfactory receptor neurons and eliciting an olfactory response. Such response is tightly related to the slow diffusion of an odorant to its receptors. And it will never be similar to the sound signals which have a dynamic range from several ten hertz up to several ten kilo hertz and can be changed immediately and freely, nor be similar to the transmission signals in hippocampus or many other cortical neurons, which may contain the spike trains with a firing rate as high as several hundred hertz. An odorant event is usually in a range of a few hundred

milliseconds to a few minutes. To adapt such a property, the olfactory receptor neurons, as an odor sensor, should also have different features from the neurons that need to fire in high-frequency discharges. At least it is thinkable that using bursts of several hundred hertz to encode a signal with a usual frequency of only a few hertz will be energy dissipation, which will normally not be adopted by the organism if there are no special circumstances.

This may explain why the observed basal activity of an olfactory receptor neuron is around 0.1 to 10 Hz. By the same token, the rising and falling phases of the action potentials are also not necessarily as short as in neurons that need to fire in high-frequency discharges, because longer (or slower) rising and falling phases will need less number of Na^+ and K^+ channels, which will further reduce the energy consumption.

As an adaptation for the long duration of action potentials, it is now necessary to activate the BK channels with a longer delay in olfactory receptor neurons than in cortical neurons. That is why the distance between BK and Ca^{2+} channels in the current finding, as compared to the previous report (Müller, 2007), is longer. And the number of Ca^{2+} channels which involved in the activation of BK channels, may also not be only one, just because the longer diffusional distance needs more Ca^{2+} to maintain an effective concentration for the activation of BK channels.

4.3.4 Mechanisms: a negative feedback

In order to fit the odorant events that are usually slow in speed but long lasting, low spiking rates with long duration action potentials are employed by the olfactory receptor neurons. Accordingly, to accomplish the BK channel activation being phase-locked to an action potential with a precise delay of millisecond range, BK channels are arranged in a specific distance beside the Ca^{2+} channels, whereby the neurons can have a very good adaptation for the low-frequency signal without additional efforts or means. Besides, the activation of BK channels further speeds up

the membrane potential repolarization and in turn reduces the Ca^{2+} influx. In other words, as soon as BK channels are activated, the Ca^{2+} has completed its task and further influx seems not necessary; thus, the activation of BK channels closes the Ca^{2+} channels and in turn limits the amount of Ca^{2+} influx. Such a signaling mechanism depicts a negative feedback that may keep the low intracellular Ca^{2+} environment.

On the other hand, a time activation of BK channels will effectively control the duration of action potentials, which may provide the olfactory receptor neurons with a broad dynamic range and a potential possibility of higher spiking rates in response to the odorant stimuli. With this property, more pronounced synaptic transmission can be generated, which in turn not only increases the range of sensation, but also improves the quality of signaling.

4.3.5 Functions of BK channels in signaling

Activation of BK channels not only speeds up the membrane potential repolarization, but also maintains the short ISIs (Fig. 23). Besides, the effect of BK channels also has an initial delay. As shown in Fig. 23C, blocking BK channels slightly influenced the first ISI, while the second and the subsequent ISIs increased significantly, which means that the effect of BK channels on ISIs requires a pre-activation of the neurons.

Such function in maintaining the short ISIs and its initial delay indicate that: 1) BK channels are essential for olfactory receptor neurons to have a high-frequency firing rate in response to odorant stimuli, and 2) BK channels, in some extent, synchronize the excitation of a neuron and the initiation of a spike train. Since BK channels will take effect only after an action potential, and since high $[Ca^{2+}]$ will soon recover after the neuronal excitation (proved by the rapid disappearance of Ca^{2+} microdomains after the depolarization), BK channels can be effective also only for a short time; thus, if there is no more action potentials induced within a certain period after the first action potential, the effect of BK channels will not contribute to the subsequent ISIs. If the time of the ISIs encodes the starting of the neuronal excitation, the reliable existence of such a

point is because the activation of BK channels depends on the activation of neurons, and consequently the evoked BK channels feedback modulate the ISIs that may encode the onset of the excitation.

It is well known that the activity of postsynaptic neurons is modulated by the neuronal integration of presynaptic impulses, which is a crucial step of information processing in signaling via the synaptic transmission. The mitral/tufted (M/T) cells which receive information from the axons of olfactory receptor neurons, forming synapses in glomeruli, are the postsynaptic neurons of olfactory receptor neurons. Therefore, the activity of M/T cells is also modulated by the presynaptic spike trains generated in olfactory receptor neurons. As BK channels are essential for the spike trains in olfactory receptor neurons, one immediate implication is, that BK channels also play a key role in the signal transduction in these two types of neurons. One preliminary result has demonstrated that blocking BK channels in olfactory receptor neurons would shift the response firing patterns in M/T cells in response to the odorant stimuli, and in some M/T cells, even the response waveform itself was eliminated. These phenomena further imply that without functional BK channels in presynaptic neurons, the signal transmission will be disturbed, and the integration of the M/T cells will be unable to relay the disturbed response anymore.

So, the feedback control provided by the BK channels in olfactory receptor neurons achieves crucial functions, not only shaping the action potential, limiting the Ca^{2+} influx, but also facilitating the firing rates which may encode the odorant information for higher centers.

4.4 Ca^{2+} microdomains in ORNs, a physiological outcome

Ca^{2+}, as a second messenger, impacts a multitude of cellular processes and does so by partitioning its actions in time and space; Ca^{2+} signaling is thus highly dynamic in that it not only responds to extracellular signals but also is greatly involved in a variety of intracellular feedback controls. In many excitable cells, an important one of such

dynamic feedback controls is mediated by the BK channels, which limit the amount of Ca^{2+} influx evoked by membrane depolarization. Because of this dynamic feedback control, BK channels can contribute to many strictly and subtly timing processes like the fine-tuning of firing, membrane potential oscillation, and muscle contractility (Salkoff *et al.*, 2006).

Several investigators have addressed the question of how BK channels can be selectively regulated by Ca^{2+} influx through voltage-gated Ca^{2+} channels, given that BK channels typically require micromolar concentrations of free Ca^{2+} for robust activation at physiological membrane potentials (Grunnet and Kaufmann, 2004; Berkefeld *et al.*, 2006; Loane *et al.*, 2007), the close distance between those two channels could be the key element, namely the forming of Ca^{2+} microdomains with the co-localized BK channels in proper distances.

In olfactory receptor neurons, the odorant stimuli bind to the receptors and generate the action potentials, which accomplish the first step of the olfactory signal transduction. In this first step, the signaling feedback control in the shape of individual action potentials and in the modulation of firing rates is conferred by the functional Ca^{2+} microdomains where the localizations of BK and Ca^{2+} channels are precisely arranged to ensure the maximum efficiency. In spite of a very few BK channels and voltage-gated Ca^{2+} channels being expressed in the olfactory receptor neurons, they still can be well organized in the surface membrane by a marvelous workmanship of the neurons, forming the functional Ca^{2+} microdomains. With such functional microdomains, local Ca^{2+} influx generated by membrane potential depolarization is able to control the BK channels precisely, and further to govern the downstream effectors accurately, which is no doubt an important even indispensable feature in olfactory signal transduction.

The Ca^{2+} microdomains in olfactory receptor neurons of *Xenopus laevis* is a very good example of how the cells can regulate their function through modulating and

optimizing the extent and location of Ca^{2+} signaling. The targets and the voltage-gated Ca^{2+} channels lie a certain distance apart from each other and form the Ca^{2+} microdomains. With the participation of internal buffering proteins, the Ca^{2+} microdomains ensure that action potential-evoked Ca^{2+} influx reach a high concentration only within a microdomain, and effectively and accurately regulate the targets via the precisely optimized distance, while the bulk Ca^{2+} concentration is still kept at a low level. Depending on the number of Ca^{2+} channels located in the Ca^{2+} microdomains and the duration of action potentials, as well as the kinetics of buffering proteins, the Ca^{2+} signal can either remain confined within several ten nanometers or spread a few hundred nanometers around the channel pole. Such restricted and compartmentalized events of Ca^{2+} influx, which further only activate all the Ca^{2+}-activated ion channels nearby, are concerned with the main excitatory function of the neurons. Long lasting Ca^{2+} signals, however, influence a multitude of cellular processes and can ultimately lead to cell death. The Ca^{2+} microdomains reveal a perfect model that can demonstrate how the concepts of Ca^{2+} signaling combine to produce a specific physiological outcome, which not only overcome the Ca^{2+} overloading, but also subtly control the downstream signaling in only defined space and time.

5. References

Ahmed Z, Connor JA. 1988. Calcium regulation by and buffer capacity of molluscan neurons during calcium transients. *Cell Calcium*. 9(2): 57-69. PMID: 3383224

Alvarez O, Gonzalez C, Latorre R. 2002. Counting channels: a tutorial guide on ion channel fluctuation analysis. *Adv Physiol Educ*. 26(1-4): 327-41. PMID: 12444005.

Armstrong CE, Roberts WM. 2001. Rapidly inactivating and non-inactivating calcium-activated potassium currents in frog saccular hair cells. *J Physiol*. 536(Pt 1): 49-65. PMID: 11579156.

Atkinson NS, Robertson GA, Ganetzky B. 1991. A component of calcium-activated potassium channels encoded by the Drosophila slo locus. *Science*. 253(5019): 551-5. PMID: 1857984.

Bao L, Rapin AM, Holmstrand EC, Cox DH. 2002. Elimination of the BK(Ca) channel's high-affinity Ca(2+) sensitivity. *J Gen Physiol*. 120(2): 173-89. PMID: 12149279.

Behrens R, Nolting A, Reimann F, Schwarz M, Waldschütz R, Pongs O. 2000. hKCNMB3 and hKCNMB4, cloning and characterization of two members of the large-conductance calcium-activated potassium channel β subunit family. *FEBS Lett*. 474(1): 99-106. PMID: 10828459.

Berkefeld H, Sailer CA, Bildl W, Rohde V, Thumfart JO, Eble S, Klugbauer N, Reisinger E, Bischofberger J, Oliver D, Knaus HG, Schulte U, Fakler B. 2006. BK_{Ca}-Cav channel complexes mediate rapid and localized Ca^{2+}-activated K^+ signaling. *Science*. 314(5799): 615-20. PMID: 17068255.

Berridge MJ. 2006. Calcium microdomains: organization and function. *Cell Calcium*. 40(5-6): 405-12. PMID: 17030366.

Birnbaumer L, Campbell KP, Catterall WA, Harpold MM, Hofmann F, Horne WA, Mori Y, Schwartz A, Snutch TP, Tanabe T, et al. 1994. The naming of voltage-gated calcium channels. *Neuron*. 13(3): 505-6. PMID: 7917287.

Blatz AL, Magleby KL. 1984. Ion conductance and selectivity of single calcium-activated potassium channels in cultured rat muscle. *J Gen Physiol*. 84(1): 1-23. PMID: 6086805.

Blatz AL, Magleby KL. 1987. Calcium-activated potassium channels. *Trends Neurosci*. 10(11): 463-467.

Bond CT, Maylie J, Adelman JP. 1999. Small-conductance calcium-activated potassium channels. *Ann N Y Acad Sci*. 868: 370-8. PMID: 10414306.

Bootman M, Niggli E, Berridge M, Lipp P. 1997. Imaging the hierarchical Ca2+ signalling system in HeLa cells. *J Physiol*. 499 (Pt 2): 307-14. PMID: 9080361.

Bortolozzi M, Lelli A, Mammano F. 2008. Calcium microdomains at presynaptic active zones of vertebrate hair cells unmasked by stochastic deconvolution. *Cell Calcium*. 44(2): 158-68. PMID: 18249440.

Brenner R, Chen QH, Vilaythong A, Toney GM, Noebels JL, Aldrich RW. 2005. BK channel β4 subunit reduces dentate gyrus excitability and protects against temporal lobe seizures. *Nat Neurosci*. 8(12): 1752-9. PMID: 16261134.

Brenner R, Jegla TJ, Wickenden A, Liu Y, Aldrich RW. 2000a. Cloning and functional characterization of novel large conductance calcium-activated potassium channel β subunits, hKCNMB3 and hKCNMB4. J Biol Chem.; 275(9): 6453-61. PMID: 10692449.

Brenner R, Peréz GJ, Bonev AD, Eckman DM, Kosek JC, Wiler SW, Patterson AJ, Nelson MT, Aldrich RW. 2000b. Vasoregulation by the β1 subunit of the calcium-activated potassium channel. *Nature*. 407(6806): 870-6. PMID: 11057658.

Brochet DX, Yang D, Di Maio A, Lederer WJ, Franzini-Armstrong C, Cheng H. 2005. Ca^{2+} blinks: rapid nanoscopic store calcium signaling. *Proc Natl Acad Sci* U S A. 102(8): 3099-104. PMID: 15710901.

Butler A, Tsunoda S, McCobb DP, Wei A, Salkoff L. 1993. mSlo, a complex mouse gene encoding "maxi" calcium-activated potassium channels. *Science*. 261(5118): 221-4. PMID: 7687074.

Capogrossi MC, Stern MD, Spurgeon HA, Lakatta EG. 1988. Spontaneous Ca^{2+} release from the sarcoplasmic reticulum limits Ca^{2+}-dependent twitch potentiation in individual cardiac myocytes. A mechanism for maximum inotropy in the myocardium. *J Gen Physiol*. 91(1): 133-55. PMID: 3343586.

Catterall WA, Perez-Reyes E, Snutch TP, Striessnig J. 2005. International Union of Pharmacology. XLVIII. Nomenclature and structure-function relationships of voltage-gated calcium channels. *Pharmacol Rev*. 57(4): 411-25. PMID: 16382099.

Catterall WA, Striessnig J, Snutch TP, Perez-Reyes E. 2003. International Union of Pharmacology. International Union of Pharmacology. XL. Compendium of voltage-gated ion channels: calcium channels. *Pharmacol Rev*. 55(4): 579-81. PMID: 14657414.

Chang CP, Dworetzky SI, Wang J, Goldstein ME. 1997. Differential expression of the α and β subunits of the large-conductance calcium-activated potassium channel: implication for channel diversity. *Brain Res Mol Brain Res*. 45(1): 33-40. PMID: 9105668.

Chavis P, Ango F, Michel JM, Bockaert J, Fagni L. 1998. Modulation of big K^+ channel activity by ryanodine receptors and L-type Ca^{2+} channels in neurons. *Eur J Neurosci*. 10(7): 2322-7. PMID: 9749760.

Chen L, Tian L, MacDonald SH, McClafferty H, Hammond MS, Huibant JM, Ruth P,

Knaus HG, Shipston MJ. 2005. Functionally diverse complement of large conductance calcium- and voltage-activated potassium channel (BK) α-subunits generated from a single site of splicing. *J Biol Chem*. 280(39): 33599-609. PMID: 16081418.

Chen TW, Lin BJ, Schild D. 2009. Odor coding by modules of coherent mitral/tufted cells in the vertebrate olfactory bulb. *Proc Natl Acad Sci* U S A. 106(7): 2401-6. PMID: 19181842.

Cheng H, Lederer MR, Lederer WJ, Cannell MB. 1996. Calcium sparks and $[Ca^{2+}]_i$ waves in cardiac myocytes. *Am J Physiol*. 270(1 Pt 1): C148-59. PMID: 8772440.

Cheng H, Lederer WJ, Cannell MB. 1993. Calcium sparks: elementary events underlying excitation-contraction coupling in heart muscle. *Science*. 262(5134): 740-4. PMID: 8235594

Cheng H, Lederer WJ. 2008. Calcium sparks. *Physiol Rev*. 88(4):1491-545.PMID: 18923188.

Chess A, Simon I, Cedar H, Axel R. 1994. Allelic inactivation regulates olfactory receptor gene expression. *Cell*. 78(5): 823-34. PMID: 8087849.

Cho W, Stahelin RV. 2005. Membrane-protein interactions in cell signaling and membrane trafficking. *Annu Rev Biophys Biomol Struct*. 34: 119-51.PMID: 15869386.

Clapham DE. 2007. Calcium signaling. *Cell*. 131(6): 1047-58. PMID: 18083096.

Conti R, Tan YP, Llano I. 2004. Action potential-evoked and ryanodine-sensitive spontaneous Ca^{2+} transients at the presynaptic terminal of a developing CNS inhibitory synapse. *J Neurosci*. 24(31): 6946-57. PMID: 15295030.

Cox DH, Cui J, Aldrich RW. 1997. Allosteric gating of a large conductance Ca-activated K^+ channel. *J Gen Physiol*. 110(3): 257-81. PMID: 9276753.

De Crescenzo V, ZhuGe R, Velázquez-Marrero C, Lifshitz LM, Custer E, Carmichael J, Lai FA, Tuft RA, Fogarty KE, Lemos JR, Walsh JV Jr. 2004. Ca^{2+} syntillas, miniature Ca^{2+} release events in terminals of hypothalamic neurons, are increased in frequency by depolarization in the absence of Ca^{2+} influx. *J Neurosci*. 24(5): 1226-35. PMID: 14762141.

Denk W, Sugimori M, Llinás R. 1995. Two types of calcium response limited to single spines in cerebellar Purkinje cells. *Proc Natl Acad Sci* U S A. 92(18): 8279-82. PMID: 7667282.

Edgerton JR, Reinhart PH. 2003. Distinct contributions of small and large conductance Ca^{2+}-activated K^+ channels to rat Purkinje neuron function. *J Physiol*. 548(Pt 1): 53-69. PMID: 12576503.

Eisenman G, Latorre R, Miller C. 1986. Multi-ion conduction and selectivity in the

high-conductance Ca++-activated K+ channel from skeletal muscle. *Biophys J*. 50(6): 1025-34. PMID: 2432947.

Endo M. 2009. Calcium-induced calcium release in skeletal muscle. *Physiol Rev*. 89(4):1153-76. PMID: 19789379.

Ertel EA, Campbell KP, Harpold MM, Hofmann F, Mori Y, Perez-Reyes E, Schwartz A, Snutch TP, Tanabe T, Birnbaumer L, Tsien RW, Catterall WA. 2000. Nomenclature of voltage-gated calcium channels. *Neuron*. 25(3): 533-5. PMID: 10774722.

Fagni L, Chavis P, Ango F, Bockaert J. 2000. Complex interactions between mGluRs, intracellular Ca^{2+} stores and ion channels in neurons. *Trends Neurosci*. 23(2): 80-8. PMID: 10652549.

Fakler B, Adelman JP. 2008. Control of K_{Ca} channels by calcium nano/microdomains. *Neuron*. 59(6): 873-81. PMID: 18817728.

Fiorillo CD, Williams JT. 1998. Glutamate mediates an inhibitory postsynaptic potential in dopamine neurons. *Nature*. 394(6688): 78-82. PMID: 9665131.

Fodor AA, Aldrich RW. 2009. Convergent evolution of alternative splices at domain boundaries of the BK channel. *Annu Rev Physiol*. 71: 19-36. PMID: 18694345.

Gennerich A, Schild D. 2002. Anisotropic diffusion in mitral cell dendrites revealed by fluorescence correlation spectroscopy. *Biophys J*. 83(1): 510-22. PMID: 12080138.

Gennerich A, Schild D. 2005. Sizing-up finite fluorescent particles with nanometer-scale precision by convolution and correlation image analysis. *Eur Biophys J*. 34(3): 181-99. PMID: 15609049.

Gerke V, Creutz CE, Moss SE. 2005. Annexins: linking Ca^{2+} signalling to membrane dynamics. *Nat Rev Mol Cell Biol*. 6(6): 449-61. PMID: 15928709.

Goldberg JH, Tamas G, Aronov D, Yuste R. 2003. Calcium microdomains in aspiny dendrites. *Neuron*. 40(4): 807-21. PMID: 14622584.

Goldstein SA, Bockenhauer D, O'Kelly I, Zilberberg N. 2001. Potassium leak channels and the KCNK family of two-P-domain subunits. *Nat Rev Neurosci*. 2(3): 175-84. PMID: 11256078.

Golowasch J, Kirkwood A, Miller C. 1986. Allosteric effects of Mg^{2+} on the gating of Ca^{2+}-activated K^+ channels from mammalian skeletal muscle. *J Exp Biol*. 124: 5-13. PMID: 2428908.

González A, Kirsch WG, Shirokova N, Pizarro G, Stern MD, Ríos E. 2000. The spark and its ember: separately gated local components of Ca^{2+} release in skeletal muscle. *J Gen Physiol*. 115(2): 139-58. PMID: 10653893.

Gordon MP, Ha T, Selvin PR. 2004. Single-molecule high-resolution imaging with

photobleaching. *Proc Natl Acad Sci* U S A. 101(17):6462-5. PMID: 15096603.

Gorman AL, Thomas MV. 1980. Intracellular calcium accumulation during depolarization in a molluscan neurone. *J Physiol*. 308: 259-85. PMID: 7230017.

Grunnet M, Kaufmann WA. 2004. Coassembly of big conductance Ca^{2+}-activated K^+ channels and L-type voltage-gated Ca^{2+} channels in rat brain. *J Biol Chem*. 279(35): 36445-53. PMID: 15210719.

Ha TS, Heo MS, Park CS. 2004. Functional effects of auxiliary β4-subunit on rat large-conductance Ca^{2+}-activated K^+ channel. *Biophys J*. 86(5): 2871-82. PMID: 15111404.

Heppner TJ, Bonev AD, Nelson MT. 1997. Ca^{2+}-activated K^+ channels regulate action potential repolarization in urinary bladder smooth muscle. *Am J Physiol*. 273(1 Pt 1): C110-7. PMID: 9252448.

Hicks GA, Marrion NV. 1998. Ca^{2+}-dependent inactivation of large conductance Ca^{2+}-activated K^+ (BK) channels in rat hippocampal neurones produced by pore block from an associated particle. *J Physiol*. 508(Pt 3): 721-34. PMID: 9518728.

Hirsch N, Zimmerman LB, Grainger RM. 2002. *Xenopus*, the next generation: *X. tropicalis* genetics and genomics. *Dev Dyn*. 225(4): 422-33. PMID: 12454920.

HODGKIN AL, KEYNES RD. 1957. Movements of labelled calcium in squid giant axons. *J Physiol*. 138(2): 253-81. PMID: 13526124.

Holmes KH, Keele NB, Arvanov VL, Shinnick-Gallagher P. 1996. Metabotropic glutamate receptor agonist-induced hyperpolarizations in rat basolateral amygdale neurons: receptor characterization and ion channels. *J Neurophysiol*. 76(5): 3059-69. PMID: 8930255.

Horrigan FT, Cui J, Aldrich RW. 1999. Allosteric voltage gating of potassium channels I. Mslo ionic currents in the absence of Ca^{2+}. *J Gen Physiol*. 114(2): 277-304. PMID: 10436003.

Ichihara A, Tanaami A, Isozaki K, Sugiyama Y, Kosugi Y, Mikuriya K, Abe M, Uemura I. 1996. High speed confocal fluorescence microscopy using a Nipkow scanner with microlenses for 3-D imaging of single fluorescent molecules in real time. *Bioimages*. 4: 57-62.

Isaacson JS, Murphy GJ. 2001. Glutamate-mediated extrasynaptic inhibition: direct coupling of NMDA receptors to Ca^{2+}-activated K^+ channels. *Neuron*. 31(6): 1027-34. PMID: 11580901.

Jackson AC, Yao GL, Bean BP. 2004. Mechanism of spontaneous firing in dorsomedial suprachiasmatic nucleus neurons. *J Neurosci*. 24(37): 7985-98. PMID: 15371499.

Jiang Y, Pico A, Cadene M, Chait BT, MacKinnon R. 2001. Structure of the RCK

domain from the E. coli K^+ channel and demonstration of its presence in the human BK channel. *Neuron*. 29(3): 593-601. PMID: 11301020.

Jiang Z, Wallner M, Meera P, Toro L. 1999. Human and rodent MaxiK channel β-subunit genes: cloning and characterization. *Genomics*. 55(1): 57-67. PMID: 9888999.

Kawai F. 2002. Ca^{2+}-activated K^+ currents regulate odor adaptation by modulating spike encoding of olfactory receptor cells. *Biophys J*. 82(4): 2005-15. PMID: 11916858.

Kehl SJ, Wong K. 1996. Large-conductance calcium-activated potassium channels of cultured rat melanotrophs. *J Membr Biol.*; 150(3): 219-30. PMID: 8661991.

Kennedy HJ, Meech RW. 2002. Fast Ca^{2+} signals at mouse inner hair cell synapse: a role for Ca^{2+}-induced Ca^{2+} release. *J Physiol*. 539(Pt 1): 15-23. PMID: 11850498.

Knaus HG, Garcia-Calvo M, Kaczorowski GJ, Garcia ML. 1994. Subunit composition of the high conductance calcium-activated potassium channel from smooth muscle, a representative of the mSlo and slowpoke family of potassium channels. *J Biol Chem*. 269(6): 3921-4. PMID: 7508434.

Kobel HR, Du Pasquier L. 1986. Genetics of polyploid *Xenopus*. *Trends Genet*. 12: 310-315.

Kretsinger RH. 1980. Structure and evolution of calcium-modulated proteins. *CRC Crit Rev Biochem*. 8(2): 119-74. PMID: 6105043.

Lakatta EG, Vinogradova T, Lyashkov A, Sirenko S, Zhu W, Ruknudin A, Maltsev VA. 2006. The integration of spontaneous intracellular Ca^{2+} cycling and surface membrane ion channel activation entrains normal automaticity in cells of the heart's pacemaker. *Ann N Y Acad Sci*. 1080: 178-206. PMID: 17132784.

Lancaster B, Nicoll RA. 1987. Properties of two calcium-activated hyperpolarizations in rat hippocampal neurones. *J Physiol*. 389: 187-203. PMID: 2445972.

Langer P, Gründer S, Rüsch A. 2003. Expression of Ca^{2+}-activated BK channel mRNA and its splice variants in the rat cochlea. *J Comp Neurol*. 455(2): 198-209. PMID: 12454985.

Latorre R, Brauchi S. 2006. Large conductance Ca^{2+}-activated K^+ (BK) channel: activation by Ca^{2+} and voltage. *Biol Res*. 39(3): 385-401. PMID: 17106573.

Latorre R, Miller C. 1983. Conduction and selectivity in potassium channels. *J Membr Biol*. 71(1-2): 11-30. PMID: 6300405.

Laude AJ, Simpson AW. 2009. Compartmentalized signalling: Ca^{2+} compartments, microdomains and the many facets of Ca^{2+} signalling. *FEBS J*. 276(7): 1800-16. PMID: 19243429.

Launikonis BS, Zhou J, Royer L, Shannon TR, Brum G, Ríos E. 2006. Depletion "skraps" and dynamic buffering inside the cellular calcium store. *Proc Natl Acad Sci U S A*. 103(8): 2982-7. PMID: 16473932.

Laurent G. 1999. A systems perspective on early olfactory coding. *Science*. 286(5440): 723-8. PMID: 10531051.

Lee SH, Rosenmund C, Schwaller B, Neher E. 2000. Differences in Ca^{2+} buffering properties between excitatory and inhibitory hippocampal neurons from the rat. *J Physiol*. 525 Pt 2: 405-18. PMID: 10835043.

Lipp P, Niggli E. 1998. Fundamental calcium release events revealed by two-photon excitation photolysis of caged calcium in Guinea-pig cardiac myocytes. *J Physiol*. 508 (Pt 3): 801-9. PMID: 9518734.

Loane DJ, Lima PA, Marrion NV. 2007. Co-assembly of N-type Ca^{2+} and BK channels underlies functional coupling in rat brain. *J Cell Sci*. 120(Pt 6): 985-95. PMID: 17311846.

Long SB, Campbell EB, Mackinnon R. 2005. Voltage sensor of Kv1.2: structural basis of electromechanical coupling. *Science*. 309(5736): 903-8. PMID: 16002579.

Lovell PV, McCobb DP. 2001. Pituitary control of BK potassium channel function and intrinsic firing properties of adrenal chromaffin cells. *J Neurosci*. 21(10): 3429-42. PMID: 11331373.

Lumpkin EA, Hudspeth AJ. 1998. Regulation of free Ca^{2+} concentration in hair-cell stereocilia. *J Neurosci*. 18(16): 6300-18. PMID: 9698322.

Magleby KL. 2003. Gating mechanism of BK (Slo1) channels: so near, yet so far. *J Gen Physiol*. 121(2): 81-96. PMID: 12566537.

Manzini I, Peters F, Schild D. 2002. Odorant responses of Xenopus laevis tadpole olfactory neurons: a comparison between preparations. *J Neurosci Methods*. 121(2): 159-67. PMID: 12468006.

Marrion NV, Tavalin SJ. 1998. Selective activation of Ca^{2+}-activated K^+ channels by co-localized Ca^{2+} channels in hippocampal neurons. *Nature*. 395(6705): 900-5. PMID: 9804423.

McBurney RN, Neering IR. 1985. The measurement of changes in intracellular free calcium during action potentials in mammalian neurones. *J Neurosci Methods*. 13(1): 65-76. PMID: 2581101.

McManus OB, Helms LM, Pallanck L, Ganetzky B, Swanson R, Leonard RJ. 1995. Functional role of the β subunit of high conductance calcium-activated potassium channels. *Neuron*. 14(3): 645-50. PMID: 7695911.

Meera P, Wallner M, Song M, Toro L. 1997. Large conductance voltage- and calcium-dependent K^+ channel, a distinct member of voltage-dependent ion channels

with seven N-terminal transmembrane segments (S0-S6), an extracellular N terminus, and an intracellular (S9-S10) C terminus. *Proc Natl Acad Sci* U S A. 94(25): 14066-71. PMID: 9391153.

Meredith AL, Thorneloe KS, Werner ME, Nelson MT, Aldrich RW. 2004. Overactive bladder and incontinence in the absence of the BK large conductance Ca^{2+}-activated K^+ channel. *J Biol Chem*. 279(35): 36746-52. PMID: 15184377

Moulton G, Attwood TK, Parry-Smith DJ, Packer JC. 2003. Phylogenomic analysis and evolution of the potassium channel gene family. *Receptors Channels*. 9(6): 363-77. PMID: 14698964.

Müller A, Kukley M, Uebachs M, Beck H, Dietrich D. 2007. Nanodomains of single Ca^{2+} channels contribute to action potential repolarization in cortical neurons. *J Neurosci*. 27(3): 483-95. PMID: 17234581.

Nakano A. 2002. Spinning-disk confocal microscopy -- a cutting-edge tool for imaging of membrane traffic. *Cell Struct Funct*. 27(5): 349-55. PMID: 12502889.

Nakayama S, Kretsinger RH. 1994. Evolution of the EF-hand family of proteins. *Annu Rev Biophys Biomol Struct*. 23: 473-507.PMID: 7919790.

Naraghi M, Neher E. 1997. Linearized buffered Ca^{2+} diffusion in microdomains and its implications for calculation of $[Ca^{2+}]$ at the mouth of a calcium channel. *J Neurosci*. 17(18): 6961-73. PMID: 9278532.

Neher E, Augustine GJ. 1992. Calcium gradients and buffers in bovine chromaffin cells. *J Physiol*. 450: 273-301. PMID: 1331424.

Neher E, Stevens CF. 1977. Conductance fluctuations and ionic pores in membranes. *Annu Rev Biophys Bioeng*. 6: 345-81. PMID: 68708.

Neher, E. 1986. Concentration profiles of intracellular calcium in the presence of a diffusible chelator. *Exp. Brain Res*. Ser. 14: 980-92.

Nicholls DG, Crompton M. 1980. Mitochondrial calcium transport. *FEBS Lett*. 111(2): 261-8. PMID: 6987089.

Oberhauser A, Alvarez O, Latorre R. 1988. Activation by divalent cations of a Ca^{2+}-activated K^+ channel from skeletal muscle membrane. *J Gen Physiol*. 92(1): 67-86. PMID: 3171535.

Park HY, Kim SA, Korlach J, Rhoades E, Kwok LW, Zipfel WR, Waxham MN, Webb WW, Pollack L. 2008. Conformational changes of calmodulin upon Ca^{2+} binding studied with a microfluidic mixer. *Proc Natl Acad Sci* U S A. 105(2): 542-7. PMID: 18178620.

Pattillo JM, Yazejian B, DiGregorio DA, Vergara JL, Grinnell AD, Meriney SD. 2001. Contribution of presynaptic calcium-activated potassium currents to transmitter release regulation in cultured Xenopus nerve-muscle synapses. *Neuroscience*. 102(1):

229-40. PMID: 11226687.

Pérez GJ, Bonev AD, Patlak JB, Nelson MT. 1999. Functional coupling of ryanodine receptors to K_{Ca} channels in smooth muscle cells from rat cerebral arteries. *J Gen Physiol*. 113(2): 229-38. PMID: 9925821.

Petran M, Hadravsky M, Egger MD, Galambos R. 1968. Tandem scanning reflected light microscope. *J Opt Soc Am*. 58:661–4.

Poulsen AN, Wulf H, Hay-Schmidt A, Jansen-Olesen I, Olesen J, Klaerke DA. 2009. Differential expression of BK channel isoforms and β-subunits in rat neuro-vascular tissues. *Biochim Biophys Acta*. 1788(2): 380-9. PMID: 18992709.

Prakriya M, Lingle CJ. 1999. BK channel activation by brief depolarizations requires Ca^{2+} influx through L- and Q-type Ca^{2+} channels in rat chromaffin cells. *J Neurophysiol*. 81(5):2267-78. Erratum in: J Neurophysiol 1999 Nov; 82(5): 12. PMID: 10322065.

Pyott SJ, Meredith AL, Fodor AA, Vázquez AE, Yamoah EN, Aldrich RW. 2007. Cochlear function in mice lacking the BK channel alpha, beta1, or beta4 subunits. *J Biol Chem*. 282(5): 3312-24. PMID: 17135251.

Ramanathan K, Michael TH, Jiang GJ, Hiel H, Fuchs PA. 1999. A molecular mechanism for electrical tuning of cochlear hair cells. *Science*. 283(5399): 215-7. PMID: 9880252.

Randall AD, Tsien RW. 1997. Contrasting biophysical and pharmacological properties of T-type and R-type calcium channels. *Neuropharmacology*. 36(7): 879-93. PMID: 9257934.

Ricci AJ, Gray-Keller M, Fettiplace R. 2000. Tonotopic variations of calcium signalling in turtle auditory hair cells. *J Physiol*. 524 Pt 2: 423-36. PMID: 10766923.

Rizzuto R, Pozzan T. 2006. Microdomains of intracellular Ca^{2+}: molecular determinants and functional consequences. *Physiol Rev*. 86(1): 369-408. PMID: 16371601.

Roberts WM, Jacobs RA, Hudspeth AJ. 1990. Colocalization of ion channels involved in frequency selectivity and synaptic transmission at presynaptic active zones of hair cells. *J Neurosci*. 10(11): 3664-84. PMID: 1700083.

Roberts WM. 1993. Spatial calcium buffering in saccular hair cells. *Nature*. 363(6424): 74-6. PMID: 8479539.

Sabatini BL, Svoboda K. 2000. Analysis of calcium channels in single spines using optical fluctuation analysis. *Nature*. 408(6812): 589-93. PMID: 11117746.

Salkoff L, Butler A, Ferreira G, Santi C, Wei A. 2006. High-conductance potassium channels of the SLO family. *Nat Rev Neurosci*. 7(12): 921-31. PMID: 17115074.

Schild D. 1989. Whole-cell currents in olfactory receptor cells of Xenopus laevis. *Exp Brain Res*. 78(2): 223-32. PMID: 2599033.

Schreiber M, Salkoff L. 1997. A novel calcium-sensing domain in the BK channel. *Biophys J*. 73(3): 1355-63. PMID: 9284303.

Schreiber M, Yuan A, Salkoff L. 1999. Transplantable sites confer calcium sensitivity to BK channels. *Nat Neurosci*. 2(5): 416-21. PMID: 10321244.

Shannon TR, Guo T, Bers DM. 2003. Ca^{2+} scraps: local depletions of free $[Ca^{2+}]$ in cardiac sarcoplasmic reticulum during contractions leave substantial Ca^{2+} reserve. *Circ Res*. 93(1): 40-5. PMID: 12791706.

Shao LR, Halvorsrud R, Borg-Graham L, Storm JF. 1999. The role of BK-type Ca^{2+}-dependent K^+ channels in spike broadening during repetitive firing in rat hippocampal pyramidal cells. *J Physiol*. 521 Pt 1: 135-46. PMID: 10562340.

Shi J, Krishnamoorthy G, Yang Y, Hu L, Chaturvedi N, Harilal D, Qin J, Cui J. 2002. Mechanism of magnesium activation of calcium-activated potassium channels. *Nature*. 418(6900): 876-80. PMID: 12192410.

Shipston MJ. 2001. Alternative splicing of potassium channels: a dynamic switch of cellular excitability. *Trends Cell Biol*. 11(9): 353-8. PMID: 11514177.

Sigworth FJ, Affolter H, Neher E. 1995. Design of the EPC-9, a computer-controlled patch-clamp amplifier. 2. Software. *J Neurosci Methods*. 56(2): 203-15. PMID: 7538621.

Smith GD. 1996. Analytical steady-state solution to the rapid buffering approximation near an open Ca^{2+} channel. *Biophys J*. 71(6): 3064-72. PMID: 8968577.

Smith JS, Imagawa T, Ma J, Fill M, Campbell KP, Coronado R. 1988. Purified ryanodine receptor from rabbit skeletal muscle is the calcium-release channel of sarcoplasmic reticulum. *J Gen Physiol*. 92(1): 1-26. PMID: 2459298.

Snutch TP, Leonard JP, Gilbert MM, Lester HA, Davidson N. 1990. Rat brain expresses a heterogeneous family of calcium channels. *Proc Natl Acad Sci* U S A. 87(9): 3391-5. PMID: 1692134.

Stefani E, Ottolia M, Noceti F, Olcese R, Wallner M, Latorre R, Toro L. 1997. Voltage-controlled gating in a large conductance Ca2+-sensitive K+channel (hslo). *Proc Natl Acad Sci* U S A. 94(10): 5427-31. PMID: 9144254.

Storm JF. 1987a. Action potential repolarization and a fast after-hyperpolarization in rat hippocampal pyramidal cells. *J Physiol*. 385: 733-59. PMID: 2443676.

Storm JF. 1987b. Intracellular injection of a Ca^{2+} chelator inhibits spike repolarization in hippocampal neurons. *Brain Res*. 435(1-2): 387-92. PMID: 3123013.

Stuyvers BD, Dun W, Matkovich S, Sorrentino V, Boyden PA, ter Keurs HE. 2005.

Ca^{2+} sparks and waves in canine purkinje cells: a triple layered system of Ca^{2+} activation. *Circ Res*. 97(1): 35-43. PMID: 15947247.

Sun XP, Callamaras N, Marchant JS, Parker I. 1998. A continuum of InsP_3-mediated elementary Ca^{2+} signalling events in *Xenopus* oocytes. *J Physiol*. 509 (Pt 1):67-80. PMID: 9547382.

Swartz KJ. 2008. Sensing voltage across lipid membranes. *Nature*. 456(7224): 891-7. PMID: 19092925.

Tanaami T, Otsuki S, Tomosada N, Kosugi Y, Shimizu M, Ishida H. 2002. High-speed 1-frame/ms scanning confocal microscope with a microlens and Nipkow disks. *Appl Opt*. 41(22): 4704-8. PMID: 12153106.

Thomas D, Lipp P, Berridge MJ, Bootman MD. 1998. Hormone-evoked elementary Ca^{2+} signals are not stereotypic, but reflect activation of different size channel clusters and variable recruitment of channels within a cluster. *J Biol Chem*. 273(42): 27130-6. PMID: 9765231.

Tian L, Duncan RR, Hammond MS, Coghill LS, Wen H, Rusinova R, Clark AG, Levitan IB, Shipston MJ. 2001. Alternative splicing switches potassium channel sensitivity to protein phosphorylation. *J Biol Chem*. 276(11): 7717-20. PMID: 11244090.

Tseng-Crank J, Godinot N, Johansen TE, Ahring PK, Str∅baek D, Mertz R, Foster CD, Olesen SP, Reinhart PH. 1996. Cloning, expression, and distribution of a Ca^{2+}-activated K^+ channel beta-subunit from human brain. *Proc Natl Acad Sci* U S A. 93(17): 9200-5. PMID: 8799178.

Tsien RW, Lipscombe D, Madison DV, Bley KR, Fox AP. 1988. Multiple types of neuronal calcium channels and their selective modulation. *Trends Neurosci*. 11(10): 431-8. PMID: 2469160.

Uebele VN, Lagrutta A, Wade T, Figueroa DJ, Liu Y, McKenna E, Austin CP, Bennett PB, Swanson R. 2000. Cloning and functional expression of two families of β-subunits of the large conductance calcium-activated K^+ channel. *J Biol Chem*. 275(30): 23211-8. PMID: 10766764.

Ukhanov K, Leinders-Zufall T, Zufall F. 2007. Patch-clamp analysis of gene-targeted vomeronasal neurons expressing a defined V1r or V2r receptor: ionic mechanisms underlying persistent firing. *J Neurophysiol*. 98(4): 2357-69. PMID: 17715188.

Vergara C, Latorre R, Marrion NV, Adelman JP. 1998. Calcium-activated potassium channels. *Curr Opin Neurobiol*. 8(3): 321-9. PMID: 9687354.

Wagner J, Keizer J. 1994. Effects of rapid buffers on Ca^{2+} diffusion and Ca^{2+} oscillations. *Biophys J*. 67(1): 447-56. PMID: 7919018.

Wallner M, Meera P, Toro L. 1999. Molecular basis of fast inactivation in voltage and

Ca^{2+}-activated K^+ channels: a transmembrane β-subunit homolog. *Proc Natl Acad Sci U S A*. 96(7): 4137-42. PMID: 10097176.

Wang B, Rothberg BS, Brenner R. 2006. Mechanism of $\beta 4$ subunit modulation of BK channels. *J Gen Physiol*. 127(4): 449-65. PMID: 16567466.

Wang SQ, Song LS, Lakatta EG, Cheng H. 2001. Ca^{2+} signalling between single L-type Ca^{2+} channels and ryanodine receptors in heart cells. *Nature*. 410(6828): 592-6. PMID: 11279498.

Wang SQ, Song LS, Xu L, Meissner G, Lakatta EG, R ós E, Stern MD, Cheng H. 2002. Thermodynamically irreversible gating of ryanodine receptors in situ revealed by stereotyped duration of release in Ca^{2+} sparks. *Biophys J*. 83(1): 242-51. PMID: 12080116.

Weigel A, Schild D, Zeug A. 2009. Resolution in the ApoTome and the confocal laser scanning microscope: comparison. *J Biomed Opt*. 14(1): 014022. PMID: 19256710.

Weiger TM, Holmqvist MH, Levitan IB, Clark FT, Sprague S, Huang WJ, Ge P, Wang C, Lawson D, Jurman ME, Glucksmann MA, Silos-Santiago I, DiStefano PS, Curtis R. 2000. A novel nervous system β subunit that downregulates human large conductance calcium-dependent potassium channels. *J Neurosci*. 20(10): 3563-70. PMID: 10804197.

Westheimer FH. 1987. Why nature chose phosphates. *Science* 235(4793): 1173-8. PMID: 2434996.

Womack MD, Chevez C, Khodakhah K. 2004. Calcium-activated potassium channels are selectively coupled to P/Q-type calcium channels in cerebellar Purkinje neurons. *J Neurosci*. 24(40): 8818-22. PMID: 15470147.

Womack MD, Khodakhah K. 2004. Dendritic control of spontaneous bursting in cerebellar Purkinje cells. *J Neurosci*. 24(14): 3511-21. PMID: 15071098.

Wu YC, Tucker T, Fettiplace R. 1996. A theoretical study of calcium microdomains in turtle hair cells. *Biophys J*. 71(5): 2256-75. PMID: 8913569.

Wulff H, Miller MJ, Hansel W, Grissmer S, Cahalan MD, Chandy KG. 2000. Design of a potent and selective inhibitor of the intermediate-conductance Ca^{2+}-activated K^+ channel, *IKCa1*: a potential immunosuppressant. *Proc Natl Acad Sci* U S A. 97(14): 8151-6. PMID: 10884437.

Xia XM, Ding JP, Lingle CJ. 1999. Molecular basis for the inactivation of Ca^{2+}- and voltage-dependent BK channels in adrenal chromaffin cells and rat insulinoma tumor cells. *J Neurosci*. 19(13): 5255-64. PMID: 10377337.

Xia XM, Zeng X, Lingle CJ. 2002. Multiple regulatory sites in large-conductance calcium-activated potassium channels. *Nature*. 418(6900): 880-4. PMID: 12192411.

Xu W, Lipscombe D. 2001. Neuronal $Ca_V 1.3$ α_1 L-type channels activate at relatively

hyperpolarized membrane potentials and are incompletely inhibited by dihydropyridines. *J Neurosci*. 21(16): 5944-51. PMID: 11487617.

Yang XH, Ren Y. 2003. The characteristics of nimodipine/SBE7-β-CD inclusion complex. *Chin J MAP*. 20(5): 380-3.

Yao LJ, Wang G, Ou-Yang KF, Wei CL, Wang XH, Wang SR, Yao W, Huang HP, Luo JH, Wu CH, Liu J, Zhou Z, Cheng HP. 2006. Ca^{2+} sparks and Ca^{2+} glows in superior cervical ganglion neurons. *Acta Pharmacol Sin*. 27(7): 848-52. PMID: 16787568

Yazejian B, Sun XP, Grinnell AD. 2000. Tracking presynaptic Ca^{2+} dynamics during neurotransmitter release with Ca^{2+}-activated K^+ channels. *Nat Neurosci*. 3(6): 566-71. PMID: 10816312.

Yusifov T, Savalli N, Gandhi CS, Ottolia M, Olcese R. 2008. The RCK2 domain of the human BK_{Ca} channel is a calcium sensor. *Proc Natl Acad Sci* U S A. 105(1): 376-81. PMID: 18162557.

Zeng XH, Xia XM, Lingle CJ. 2003. Redox-sensitive extracellular gates formed by auxiliary β subunits of calcium-activated potassium channels. *Nat Struct Biol*. 10(6): 448-54. PMID: 12740608.

Zeng XH, Xia XM, Lingle CJ. 2005. Divalent cation sensitivity of BK channel activation supports the existence of three distinct binding sites. *J Gen Physiol*. 125(3): 273-86. PMID: 15738049.

Zhou Z, Neher E. 1993. Mobile and immobile calcium buffers in bovine adrenal chromaffin cells. *J Physiol*. 469:245-73. PMID: 8271200.

ZhuGe R, Fogarty KE, Tuft RA, Walsh JV Jr. 2002. Spontaneous transient outward currents arise from microdomains where BK channels are exposed to a mean Ca^{2+} concentration on the order of 10 μM during a Ca^{2+} spark. *J Gen Physiol*. 120(1): 15-27. PMID: 12084772.

Zou H, Lifshitz LM, Tuft RA, Fogarty KE, Singer JJ. 2002. Visualization of Ca^{2+} entry through single stretch-activated cation channels. *Proc Natl Acad Sci* U S A. 99(9): 6404-9. PMID: 11983921.

Zou S, Jha S, Kim EY, Dryer SE. 2008. The β1 subunit of L-type voltage-gated Ca^{2+} channels independently binds to and inhibits the gating of large-conductance Ca^{2+}-activated K^+ channels. *Mol Pharmacol*. 73(2): 369-78. PMID: 17989350.

Appendix i

Equations for a steady-state Ca²⁺ profile near a Ca²⁺ channel

Suppose that the reaction scheme for each mobile Ca^{2+} buffer species, B_j, is

$$Ca^{2+} + B_j \underset{k_j^-}{\overset{k_j^+}{\rightleftarrows}} CaB_j$$
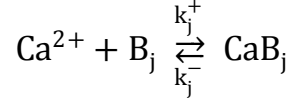
a set of reaction-diffusion equations can be created to calculate the local $[Ca^{2+}]$ near a Ca^{2+} pole (Neher, 1986; Wager, 1994; Smith, 1996):

$$\left[\frac{\partial[Ca^{2+}]}{\partial t}\right]_{diffusion} = D_{Ca}\nabla^2[Ca^{2+}] + \sum_j R_j + \frac{I_{Ca}(t)}{2F}\delta(r) \qquad (16)$$

$$\frac{\partial[B_j]}{\partial t} = D_j\nabla^2[B_j] + R_j \qquad (17)$$

Assuming independent association reactions between all buffers, R_j will be given by

$$R_j = -k_j^+[B_j][Ca^{2+}] + k_j^-(B_{j,Total} - [B_j]) \qquad (18)$$

In Eq. 16–18, D_{Ca} is the diffusion constant of free Ca^{2+}; j is an index over each buffer; $B_{j,Total}$ and D_j are the total concentration and diffusion constant of buffer j; k_j^+ and k_j^- are its association and dissociation constants; I_{Ca} is the Ca^{2+} influx through the Ca^{2+} pole which is a function of time; F is Faraday's constant; and $\delta(r)$ is the Dirac delta function. Note that if any buffer, say m, is a stationary buffer not a mobile buffer, let $D_m=0$, and the equations are still correct.

Assume that there is only one mobile buffer with unsaturable state ($[B]\approx B_{Total}$), and its concentration, $[B]$, is constant in space and time: $\nabla^2[B] = 0$, $\frac{\partial[B]}{\partial t} = 0$. Further two assumptions are that: 1) Ca^{2+} influx and diffusion reaches a stead-stare: $\frac{\partial[Ca^{2+}]}{\partial t} = 0$; and 2) the average total current of Ca^{2+} influx (I_{Ca}) is i_{Total}, which is constant, and the bulk Ca^{2+} concentration of cytosolic free Ca^{2+} is C_∞, which is constant too. So, Eq. 16–18 can be rewritten to approximated ones:

Eq. 17: $k^+[B]C_\infty = k^-(B_{Total} - [B]) \overset{K_d=\frac{k^-}{k^+}}{\Longleftrightarrow} [B] = \frac{B_{Total}\,K_d}{C_\infty + K_d}$ or $\frac{K_d(B_{Total} - [B])}{[B]} = C_\infty$

$$\text{Eq. 16:} \quad 0 = D_{Ca}\left(\frac{\partial^2}{\partial r^2} + \frac{2}{r}\frac{\partial}{\partial r}\right)[Ca^{2+}] - k^+[B]([Ca^{2+}] - C_\infty) + \frac{i_{Total}}{2F}\,\delta(r)$$

$$\xrightarrow[\left(\lambda = \sqrt{\frac{D_{Ca}}{k^+[B]}}\right)\ \text{and}\ (r>0)]{} \quad \frac{d^2[Ca^{2+}]}{dr^2} = -\frac{2}{r}\frac{d[Ca^{2+}]}{dr} + \frac{[Ca^{2+}] - C_\infty}{\lambda^2}$$

$$\xrightarrow[\lambda>0,\ [Ca^{2+}]\ \text{monotone decreasing}]{} \quad [Ca^{2+}] = \frac{A}{r}e^{-\frac{r}{\lambda}} + C_\infty \quad (A > 0, \text{constant}) \quad (19)$$

where r is the calculated distance from the Ca^{2+} pole, λ is the characteristic length of the Ca^{2+} buffer, and K_d is the equilibrium binding constant. Now, using boundary conditions for r→∞:

$$\lim_{r\to\infty}[Ca^{2+}] = C_\infty = [Ca^{2+}]_\infty$$

and Gauss's theorem for a point source and a hemisphere diffusion in r→0:

$$-[\text{Outflux}]_{r\to 0} = -\lim_{r\to 0}\left[2\pi r^2 D_{Ca}\frac{d[Ca^{2+}]}{dr}\right] = \lim_{r\to 0}\left[\frac{2\pi D_{Ca} A e^{-\frac{r}{\lambda}}(\lambda + r)}{\lambda}\right] = 2\pi D_{Ca} A$$

$$-[\text{Outflux}]_{r\to 0} = [\text{Influx}]_{r=0} = \frac{i_{Total}}{2F} \quad \Rightarrow \quad A = \frac{i_{Total}}{4\pi F D_{Ca}}$$

the result can be found as:

$$\text{Eq. 19}\xrightarrow{A = \frac{i_{Total}}{4\pi F D_{Ca}}} \quad [Ca^{2+}]_r = \frac{i_{Total}}{4\pi F D_{Ca} r}e^{-\frac{r}{\lambda}} + [Ca^{2+}]_\infty \quad (20)$$

$$\text{where} \quad \lambda = \sqrt{\frac{D_{Ca}}{K_{on}[B]}}, \quad [B] = \frac{B_{Total} K_d}{[Ca^{2+}]_\infty + K_d}, \quad K_d = \frac{K_{off}}{K_{on}}$$

Here, $[Ca^{2+}]_\infty$ is the defined bulk Ca^{2+} concentration, which is usually ~100 nM (Wager, 1994; Smith, 1996); and K_{on}/K_{off} (same as k^+/k^-) are association and dissociation constants of the Ca^{2+} buffer.

This result describes an analytical approximation to the steady-state Ca^{2+} profile near a Ca^{2+} channel (Neher, 1986). And it is a time independent function.

Appendix ii

Derivation of relationship between current mean, variance, and expression levels

The relationship between the current mean and the expected variance is derived here when more than one channel types are expressed. Points are the current means and variances of different cells came from the experiments showing a linear relationship. Such phenomena may hint new information on the signal channel current, the open probability and even the expression level of each channel type. The derivation will help to get the new information.

Suppose each cell has several independent channel types with different single channel currents and open probabilities, and each cell also has different channel number for each channel type. For example, for cell *m*, the current, I_m, and its variance, σ_m^2, are

$$I_m = \sum_j N_{j,m}\, i_j\, P_j \qquad \text{and} \qquad \sigma_m^2 = \sum_j N_{j,m}\, i_j^2\, P_j\left(1 - P_j\right)$$

where N is the channel number, i is the single channel current, P is the open probability, *j* is an index over each channel type, and *m* is an index over each cell. A further assumption is a relative proportion of individual channel types for each cell:

$$q_{j,m} = \frac{N_{j,m}}{N_{Total\,,m}}\,, \qquad \text{and} \quad \sum_j q_{j,m} = 1$$

where $N_{Total\,,m}$ is the total number of all channels in cell *m*, and $q_{j,m}$ defines the proportion of channel type *j* in cell *m*.

If I_m and σ_m^2 show a linear relationship, a general line equation can be written:

$$\sigma_m^2 = I_m k + b$$

$$\Leftrightarrow k = \sum_j q_{j,m}\, i_j^2\, P_j\left(1 - P_j\right)\Big/\sum_j q_{j,m}\, i_j\, P_j - b\Big/\sum_j q_{j,m}\, N_{Total\,,m}\, i_j\, P_j \qquad (21)$$

where both k and b, the slope and the offset of the line, are constants.

Now, two cases will be discussed: either b = 0 or b ≠ 0. First, suppose b = 0, such that

Eq. 21 can be rewritten as:

$$k = \sum_j q_{j,m}\, i_j^2\, P_j(1 - P_j)\bigg/\sum_j q_{j,m}\, i_j\, P_j \quad = C, \qquad (C = \text{contant}) \qquad (22).$$

Two answers can be found to keep k constant: either, (1) i and P are two constants for all channel types:

$$i_j = i;\; P_j = P \quad \Leftrightarrow \quad k = \frac{i^2\, P(1 - P)\sum_j q_{j,m}}{iP\sum_j q_{j,m}} = i(1 - P),$$

which indicates one channel type; or (2) $q_{j,m}$ for each cell are same:

$$q_{j,m} = q_j \quad \Leftrightarrow \quad k = \sum_j q_j\, i_j^2\, P_j(1 - P_j)\bigg/\sum_j q_j\, i_j\, P_j\,.$$

Now, k is independent on the cell index m, which means k is same for different cells and could be a constant. In Eq. 22, k relates to q, i and P of individual channel types. Since i and P are the properties of a channel, for each channel type they can be constants, whereas for q, it is a relative expression level in different cells, and now it should also be a constant to have a constant k at the end, meaning for each cell, regardless of the total expression level, a given channel type should be expressed in a constant proportion. That is to say in case (2) it has to be assumed that all i, P and q are independent on the cell, provided that a constant k or a linear relationship between current mean and variance is expected.

How about if $b \neq 0$? Since $b \neq 0$, and both b and k are constants, so from Eq. 21, the following equation can be got:

$$k = f(q_{j,m}, i_j, P_j) - g(q_{j,m}, i_j, P_j, N_{Total,m})b \qquad (23)$$

$$\text{where} \quad f(q_{j,m}, i_j, P_j) = \sum_j q_{j,m}\, i_j^2\, P_j(1 - P_j)\bigg/\sum_j q_{j,m}\, i_j\, P_j$$

$$\text{and,} \quad g(q_{j,m}, i_j, P_j, N_{Total,m}) = 1\bigg/\sum_j q_{j,m} N_{Total,m}\, i_j\, P_j$$

It is noticeable that the constant k is made of two parts, related to functions f and g; and f has only 3 parameters without $N_{Total,m}$ which only appears in the second part,

meaning that no matter how $N_{Total,m}$ changes, the value of $f(q_{j,m}, i_j, P_j)$, will not change. Eq. 23 can also be rewritten as:

$$f(q_{j,m}, i_j, P_j) - k = g(q_{j,m}, i_j, P_j, N_{Total,m})b$$

indicating however $N_{Total,m}$ changes, $g(q_{j,m}, i_j, P_j, N_{Total,m})$ should not change. Now, a conflict occurs under the assumption of $b \neq 0$, suggesting that if $N_{Total,m}$ is not a constant, b must be 0, or, if $b \neq 0$, $N_{Total,m}$ must be a constant, meaning that for all cells their total channel numbers are equal, which is usually not true in real cells.

So, for cells with multiple channel types and different channel numbers, if their channel current means and variances show a linear relationship, there will be two possibilities, either 1) all channel types have the same single channel current and open probability, or 2) each channel type is expressed in a constant proportion.

Appendix iii

Classification schemes for voltage-gated Ca^{2+} channel proteins in *Xenopus tropicalis*.

The following table shows the nomenclature (introduced by Tsien) and the relations to those describing the different gene types (Snutch/Birnbaumer and IUP classes). The locations of the genes are also listed.

HVA (high voltage activated, large conductance, persistent)				
Tsien class:	L-type			
Snutch/Birnbaumer class:	α_{1S}	α_{1C}	α_{1D}	α_{1F}
IUP classification:	Cav 1.1	Ca$_v$ 1.2	Ca$_v$ 1.3	Ca$_v$ 1.4
Gene (HGNC Symbol):	CACNA1S	CACNA1C	CACNA1D	CACNA1F
Ensembl ID[1]:	0015130	NF	0015664	0007195
Scaffold[2]:	scaffold_771	-	scaffold_1408	Scaffold_690
Location[3]:	391785-432827	-	10665-66402	495431-522741

HVA (high voltage activated, rapid inactivating)			
Tsien class:	P/Q-type	N-type	R-type
Snutch/Birnbaumer class:	α_{1A}	α_{1B}	α_{1E}
IUP classification:	Cav 2.1	Ca$_v$ 2.2	Ca$_v$ 2.3
Gene (HGNC Symbol):	CACNA1A	CACNA1B	CACNA1E
Ensembl ID:	NF	NF	0012458
Scaffold:	-	-	scaffold_287
Location:	-	-	72992-248422

LVA (low voltage activated)			
Tsien class:	T-type		
Snutch/Birnbaumer class:	α_{1G}	α_{1H}	α_{1I}
IUP classification:	Ca$_v$ 3.1	Ca$_v$ 3.2	Ca$_v$ 3.3
Gene (HGNC Symbol):	CACNA1G	CACNA1H	CACNA1I
Ensembl ID:	0006824	0022646	0016133
Scaffold:	scaffold_504	scaffold_27	scaffold_69
Location:	370264-493782	3957111-4249820	134152-293965

Tsien class (Tsien *et al.*, 1988); Snutch/Birnbaumer class (Snutch *et al.*, 1990; Birnbaumer *et al.*, 1994); IUP class (Ertel *et al.*, 2000; Catterall *et al.*, 2003, 2005).

IUP = International Union of Pharmacology; HGNC = HUGO Gene Nomenclature Committee; HUGO = Human Genome Organisation; NF = Not Found

[1]Ensembl ID for *Xenopus tropicalis* gene has a format like "NSXETG0000xxxxxxx", "xxxxxxx" here is a 7-digital number (e.g. 0015130) that is listed in the table.

[2]According to genome assembly version 4.1, the genome contains 19,501 scaffolds.

[3]Starting and ending position of DNA in the corresponding scaffold.

Acknowledgements

Curriculum Vitae

Personal data

Name:	Guobin Bao
Date of Birth:	26/09/1972
Place of Birth:	Shanghai, P. R. China
Nationality:	Chinese
E-Mail:	gbao@gwdg.de

Education

12/2006–Present:	Ph.D Candidate, Department of Neurophysiology and Cellular Biophysics, DFG Research Center Molecular Physiology of the Brain (CMPB).
09/2004–06/2006:	Ph.D Candidate, Institute of Biochemistry and Cell Biology, Shanghai Institutes for Biological Sciences (SIBS), Chinese Academy of Sciences (CAS).
08/2002–02/2003:	Visiting scientist, Group of Prof. Wolfgang Schwarz, Dept. of Biophysical Chemistry, Max Planck Institute of Biophysics, Frankfurt/Main
07/2001–09/2004:	M.Sc., in Cell Biology, Institute of Biochemistry and Cell Biology, SIBS, CAS.
09/1996–06/2006:	Staff, in Laboratory of Molecular Cell Biology, SIBS, CAS.
09/1991–07/1996:	B.Sc., in Biological Science, University of Science and Technology of China (USTC).